INFORMATION TO USERS

This manuscript has been reproduced from the microfilm master. UMI films the text directly from the original or copy submitted. Thus, some thesis and dissertation copies are in typewriter face, while others may be from any type of computer printer.

The quality of this reproduction is dependent upon the quality of the copy submitted. Broken or indistinct print, colored or poor quality illustrations and photographs, print bleedthrough, substandard margins, and improper alignment can adversely affect reproduction.

In the unlikely event that the author did not send UMI a complete manuscript and there are missing pages, these will be noted. Also, if unauthorized copyright material had to be removed, a note will indicate the deletion.

Oversize materials (e.g., maps, drawings, charts) are reproduced by sectioning the original, beginning at the upper left-hand corner and continuing from left to right in equal sections with small overlaps.

Photographs included in the original manuscript have been reproduced xerographically in this copy. Higher quality 6" x 9" black and white photographic prints are available for any photographs or illustrations appearing in this copy for an additional charge. Contact UMI directly to order.

Bell & Howell Information and Learning
300 North Zeeb Road, Ann Arbor, MI 48106-1346 USA

UMI®
800-521-0600

Specific ionization in a drift chamber filled with helium-isobutane

Marko Milek
Department of Physics, McGill University
Montréal, Québec, Canada

A Thesis submitted to the
Faculty of Graduate Studies and Research
in partial fulfillment of the requirements for the degree of
Master of Science

National Library
of Canada

Acquisitions and
Bibliographic Services

395 Wellington Street
Ottawa ON K1A 0N4
Canada

Bibliothèque nationale
du Canada

Acquisitions et
services bibliographiques

395, rue Wellington
Ottawa ON K1A 0N4
Canada

Your file Votre référence

Our file Notre référence

0-612-44223-3

Canada

Abstract

This thesis discusses the measurement of the dE/dx resolution of the BaBar drift chamber. The study was performed on the data obtained with a small scale prototype drift chamber (built at LAPP, Annecy, France) during test beam runs at CERN (PS) and Zurich (PSI). Drift chamber simulations were performed in order to study the expected performance. Good tracking, necessary in the analysis of the PS runs but unnecessary in the PSI runs, was obtained by performing a χ^2 minimization of the space residuals, yielding a time to distance function. An average tracking resolution of $\approx 350\mu$m was achieved. The resolution result for seven energy loss samplings per event was scaled up to 40 samples per event which will be available in the BaBar chamber. The expected dE/dx resolution of the BaBar chamber, as obtained from the PS runs, is: (7.3 ± 0.1 ± 0.5) %. The result from the PSI runs is: (6.9 ± 0.4 ± 0.5) %.

Résumé

Cette thèse discute les mesures de la résolution en dE/dx de la chambre à dérive du détecteur BaBar. Cette étude a été effectuée avec les données obtenues avec un prototype a petite gamme de la chambre à dérive (construite à LAPP, à Annecy en France) dans le faisceau de test au CERN (PS) et a Zurich (PSI). Des simulations des chambres à dérives on été effectuée pour étudier la performance. Une bonne reconsturction, nécéssaire pour l'analyse des test PS mais démodée pour les tests PSI, a été obtenue en faisant une minimsation en χ^2 des "space residuals" donnant une fonction qui relit le temps et la distance. Une résolution de reconstuction de $\approx 350\mu$m a été achevée. Le résultat de la résolution pour sept mesures de l'énergie perdue par événement a été extrapolé jusqu'à 40 mesures (ce qui sera disponible dans la chambre à derive du détecteur BaBar). La résolution en dE/dx attendue de la chambre BaBar, obtenue des tests PS est: (7.3 ± 0.1 ± 0.5) %. Le résultat des tests PSI est: (6.9 ± 0.4 ± 0.5) %.

Contents

List of Figures

List of Tables

Aknowledgements

I would like to express my deepest gratitude to the members of the BaBar group at LAPP: Yannis Karyotakis, Dominique Boutigny, Andrea Jeremie, Isabelle De Bonis and Abdel Boucham for giving me the opportunity to work with them on what has proven to be an interesting and challenging project. I also thank my supervisor, Prof. Popat Patel, for his help in finding a suitable project and in writing of this thesis. This research was partially financially sponsored by the Alexander McFee Foundation.

My time at McGill was made enjoyable and interesting, both intellectually and socially, primarily by my office buddies: Shem, Claude, Kostas, Wai and Rainer, who were both helpful and supportive.

I must also thank Marko for getting us here, or, at least, helping us along the way and my parents for unconditionally believing in me.

Finally, I thank Jelena for being there, bearing with me and providing the necessary strength and stability.

Chapter 1

Introduction

The physics of Elementary Particles is a vast and ancient field, with a very ambitious goal: a fundamental description of the nature of both matter and energy. At this point, it is a very mature and well developed field, with a body of theory and a language that constitutes what are probably the most accurate theories known to modern science. This language is called Quantum Field Theory (QFT) and it is a (some sceptics would say forced) mixture of several theories:

- Quantum Mechanics - the laws that describe the processes at atomic distance scales, where the classical laws of Newton and his successors break down and where the traditional notions of reality are challenged.

- Special Relativity - Einstein's discovery of the relationships between space and time on one hand, and matter and energy on the other.

- Field Theory - originally developed by Faraday and Maxwell to describe electricity and magnetism and now extended to describing strong interactions, weak interactions and gravitation.

- Symmetry Principles - the application of the mathematical Theory of Groups to describe a set of transformations that can be applied to physical systems and leave them unchanged are now being used to classify and enumerate those systems.

The importance of CP violation, especially in the early universe formation, can not be overestimated. If indeed all the matter and energy of the Universe were created out of the gravitational potential energy of the Big Bang, the symmetry with respect to charge conjugation would have ensured that equal amounts of matter and antimatter were produced. But, this is clearly no longer the case, as the Universe we observe is constructed almost entirely of matter with very little antimatter. Back in 1967 Andrei Sakharov established that three requirements must be met in order to produce this matter-antimatter asymmetry [Sak67]:

- a stage in the evolution of the Universe which was far from equilibrium - this was certainly true in the first moments of Universe creation when the expansion was rapid.
- proton decay - modern Grand Unified Theories all predict that protons indeed do decay [GG74] (even though proton decay has yet not been observed, its lifetime is believed to be many orders of magnitude larger than the age of the Universe [WN96]).
- *CP* violation - observed in the kaon system in 1964. [CCFT64]

Bearing in mind the fact that *CP* violation in *B* mesons is a lot stronger than in *K* mesons, one would not be wrong in saying that the comprehensive study of the *CP violation in B decays, performed at a B factory*, is one of the priorities for High Energy Physics in the following decade. This study is the primary physics goal of the BaBar experiment. [Col95]

Chapter 2

Theoretical Background

2.1 The Standard Model

Over the last few decades a theory has emerged that describes all of the known elementary particle interactions except gravity (and as far as we can tell, gravity is far too weak to play an important role in elementary particle processes). This theory (or rather a collection of related theories) which, in addition to theories mentioned in the previous chapter, also incorporates quantum electrodynamics, the theory of electroweak processes and quantum chromodynamics has become known as *the Standard Model*. Even though no one pretends that the Standard Model is the definitive description of nature it has an attractive aesthetic feature: all of the fundamental interactions are derived from very few general principles. Those requirements on any candidate physical theory are the following: *unitarity* - ensures the conservation of probability, *microcausality* - physical observables must be separately measurable at different positions and equal times, and *locality* - the amplitudes for spatially separated physical processes must factorize and be preserved under time evolution (provided that no signals propagate from one point to the other), *invariance under Lorentz transformations and translations* - by the Noether's Theorem implies the existence of the corresponding conserved quantities (like four-momentum and angular momentum), *stability* - ensures existence of the lowest energy state and *renormalizability* - the physics at small energy scale is largely insensitive to the physics at high energy scale (if $Q \ll \Lambda$ then contributions of order Q/Λ, where Λ is the large scale energy factor and Q measures the small energy scale, can be neglected). [Bur97]

The strong, weak and electromagnetic interactions are understood as arising due to the exchange of various spin-1 bosons amongst spin-1/2 particles that make up matter. Their properties can be summarized as being particles that are associated with the generators of the algebra:

$$SU_c(3) \times SU_L(2) \times U_Y(1) \tag{2.1}$$

The eight spin-1 particles associated with the factor $SU_c(3)$ ('c' is meant to denote color, which is a quantum number carried by strongly interacting particles) are called gluons and are thought to be massless. The four spin-1 bosons associated with the factor $SU_L(2) \times U_Y(1)$ ('L' is meant to indicate that only left-handed fermions carry this quantum number, 'Y' distinguishes the group associated with the weak hypercharge from the $U_{em}(1)$, the electromagnetic group) are related to the physical bosons $W^{\pm}$, Z^0 and the photon.

Table 2.1 shows the four fundamental forces governing the interactions between both matter and energy. Masses of the gauge bosons are from [WN96]. Gravity, mediated by a hypothetical spin-2 graviton, being difficult to quantize, is excluded from the Standard Model.

Apart from spin-1 particles there are a number of fundamental spin-1/2 particles, called fermions, and the character of their interactions can be summarized by giving their transformation properties with respect to the $SU_c(3) \times SU_L(2) \times U_Y(1)$

Force	Range [m]	Mediator	Mass [MeV/c^2]	Electric Charge [e]
Gravity	infinite	Graviton	0	0
Electromagnetism	infinite	Photon	$\leq 6 \times 10^{-22}$	$\leq 5 \times 10^{-30}$
Weak	$\leq 10^{-18}$	W^+	80330	1
		W^-	80330	-1
		Z^0	91187	0
Strong	$\leq 10^{-15}$	Gluons	0	0

Table 2.1: Four fundamental forces and their mediators.

gauge group. Fermions transform in a fairly complicated way as there appear to be three families of particles, with each family coupling identically to all gauge bosons. *Leptons* are, by definition, those spin-1/2 particles which do not take part in strong interactions. Six leptons are known up to date. *Hadrons*, on the other hand, are defined as particles which do take part in strong interactions. The spectrum of known hadrons is rich but they can be accounted for as the bound states of five quarks (u, d, c, s and b). Table 2.2 is a summary of the Standard Model particle content. The masses were taken from [WN96]. Both quarks and leptons are grouped into three families. Corresponding antiparticles are not shown. The ν masses are upper limits with a 90% confidence level. The u, d and s quark masses are estimates of 'current-quark masses' in a mass independent subtraction scheme, the c and b quark masses are estimated from charmonium, bottomonium, D and B masses, the t quark mass is from a CDF observation of top candidate events.

Once the most general renormalizable Lagrangian built out of the fields corresponding to the expected particle content is diagonalized, all the boson and fermion masses can be read off and are identically zero ! The vanishing of the

Lepton	Mass [MeV]	Electric Charge	Quark	Mass [MeV/c^2]	Electric Charge [e]
ν_e	$\leq$15 10^{-6}	0	u	2-8	2/3
e	0.511	-1	d	5-15	-1/3
ν_μ	$\leq$0.17	0	c	1000-1600	2/3
μ	105.7	-1	s	100-300	-1/3
ν_τ	$\leq$24	0	t	180000	2/3
τ	1777	-1	b	4100-4500	-1/3

Table 2.2: Elementary particle content of the Standard Model.

masses is the consequence of the $SU_c(3) \times SU_L(2) \times U_Y(1)$ invariance of the theory and can be avoided only if this symmetry is spontaneously broken by the ground state. The simplest way to do so is to add to the theory a weakly-coupled spin-0 particle with a potential which is minimized for a non-zero field. This particle which is 'artificially' added to the Standard Model is the Higgs boson, which is yet to be experimentally observed, and its foundations are much weaker than the rest of the theory. In a way, the Higgs-doublet parametrizes most of our ignorance of the Standard Model. [Bur97]

2.2 Discrete Symmetries

As we have seen, symmetries play a crucial role in the Standard Model as they gave us the conserved quantities. Symmetries with the respect to the gauge group ($SU_c(3) \times SU_L(2) \times U_Y(1)$) and to electromagnetism ($U_{em}(1)$) are continuous, they represent invariance of the physical quantities under transformations governed by one or more continuous parameters (such as position in space or angular orientation). There are, in addition, symmetries associated with discrete parameters and three of them are particularly useful: *parity inversion (P)* - the inversion of the three spatial coordinates through an arbitrary origin converting a left-handed system into a right-handed, *time reversal (T)* - effectively the reversal of the temporal coordinate and *charge conjugation (C)* - a change in the sign of all internal degrees of freedom (electric charge, baryon number, lepton number, strangeness, charm, beauty, truth but not mass, four momentum and spin) of all particles in the system converting particles into antiparticles.

Until 1956 it was believed that the physical laws were ambidextrous, inverting parity on any physical process must result in another possible process. The evidence of parity violation in weak decays (original experiment was made on Co^{60} beta decay) was first detected by C. S. Wu *et al.* who found that most of the electrons were emitted in the direction of the nuclear spin. [W$^+$57] Another evidence of P violation is the fact that all neutrinos are left-handed and all antineutrinos are right-handed, as measured in $\pi^{\pm} \rightarrow \mu^{\pm} + \nu_{\mu}(\bar{\nu_{\mu}})$. Charge conjugation is also not a symmetry of the weak interactions as applying it to a left-handed neutrino produces a left-handed antineutrino, which doesn't exist ! Time reversal is a lot harder to test as no particles are eigenstates of T so we can not just look at whether a given reaction preserves the eigenvalues of the time reversal operator, or whether the rates of T *even* and T *odd* reactions are the same. The most direct way to test the conservation of T is to measure the rates of a candidate reaction (such as $n + p \rightleftharpoons d + \gamma$) as we run it both ways under the same conditions. As stated by the 'principle of detailed balance' those rates should be the same. No evidence of T violation was found in strong and electromagnetic interactions, which is hardly surprising considering that both C and P were violated exclusively in weak decays. Unfortunately, inverse-reaction experiments are hard to do in the weak interactions. Consider a typical weak decay $\Lambda \rightarrow p^+ + \pi^-$. The inverse reaction is $p^+ + \pi^- \rightarrow \Lambda$ (allowed only if the energies of p^+ and π^- are large enough to produce Λ), but we will never see such a reaction because a strong interaction of a proton and a pion will always dominate over the weak one. [Gri87] In practice the critical test of T invariance involves measurements of quantities which should be exactly equal to zero if T is a perfect symmetry. The best known experiment to date is Ramsey's upper limit on the electric dipole moment of a neutron. [Ram82]

Nevertheless, there is a compelling answer as to why time reversal cannot be a perfect symmetry of nature. Based on the most general assumptions - Lorentz invariance, quantum mechanics and the idea that interactions are carried by fields - the *TCP Theorem* states that the combined operation of time reversal, charge conjugation and parity inversion, in any order, is an exact symmetry of any interaction. [Lue57] It is not possible to construct a quantum field theory in which TCP is violated. If, as will be presented soon, CP is violated then there must be a compensating violation of T.

2.3 *CP* Violation

Some temporary relief to the 'problem' of C and P violation was provided by the discovery that the Universe is made of only left-handed particles and right-handed antiparticles. This means that the combined CP symmetry transforms the real physical states into each other. With the discovery of the CP violation in the kaon system the sanctity of discrete symmetries was pushed back again. The most obvious CP violating scenario is when two CP conjugate processes have different amplitudes. The general approach to the explanation of the CP violation, when CP conjugate amplitudes *are* the same, is via the interference of two amplitudes that have a nonzero physical phase difference in a multiamplitude process. CP violation can be either: *direct* - the two amplitudes that interfere with each other contribute directly to the decay of the B meson (there being contributions from both tree and penguin diagrams) and *indirect* - due to mixing, the interference between $X \to f$ and $X \to \bar{X} \to f$ (assuming that both X and $\bar{X}$ decay into a CP eigenstate f) gives rise to CP violation. If for a process we have $M = M_1 + e^{i\phi} M_2$ then for a rate and a CP conjugate rate

$$\begin{aligned} P &\equiv MM^* = M_1M_1^* + M_2M_2^* + M_1M_2^*e^{-i\phi} + M_2M_1^*e^{i\phi} \\ P_{CP} &\equiv \widehat{CP}MM^* = M_1M_1^* + M_2M_2^* + M_1M_2^*e^{i\phi} + M_2M_1^*e^{-i\phi} \end{aligned} \tag{2.2}$$

we get $P - P_{CP} \neq 0$. The three family Standard Model does provide the necessary CP violating phase through the *CKM matrix*.

Evidently, the long lived neutral kaon is not a perfect eigenstate of CP. Violation in $K_S^0 - K_L^0$ mixing is described by a single parameter $\epsilon = 2.3 \times 10^{-3}$:

$$\begin{aligned} |K_L^0> &= \frac{(1+\epsilon)|K^0> -(1-\epsilon)|\bar{K}^0>}{\sqrt{2(1+|\epsilon|^2)}} \\ |K_S^0> &= \frac{(1+\epsilon)|K^0> +(1-\epsilon)|\bar{K}^0>}{\sqrt{2(1+|\epsilon|^2)}} \end{aligned} \tag{2.3}$$

CP violation in the semi-leptonic kaon decays has also been observed. It is parametrized by the following quantity (charge asymmetry in leptonic decays):

$$\delta = \frac{\Gamma(K_L^0 \to \pi^- l^+ \nu) - \Gamma(K_L^0 \to \pi^+ l^- \nu)}{\Gamma(K_L^0 \to \pi^- l^+ \nu) + \Gamma(K_L^0 \to \pi^+ l^- \nu)} \tag{2.4}$$

The experimentally measured value of δ (averaged from electron and muon channels) is: $\delta = (0.327 \pm 0.012)\%$. [WN96] This asymmetry provides an absolute distinction between matter and antimatter and an unambiguous, convention free definition of positive charge as the charge of a lepton preferentially produced in the decay of a long-lived neutral kaon.

2.3.1 *CP* Violation in the Standard Model

The following sections are a summary of the several published works on the subject of CP violation in and beyond the Standard Model. The full discussion is given in: [NQ92], [Gro96], [Lon96] and [Kay96].

A Lagrangian is *CP* conserving if all the coupling and mass terms can be made real by an appropriate set of field redefinitions. In the Standard Model, the most general theory with only two quark generations and a single Higgs multiplet is of that type. However, when a third quark generation is added then the most general quark mass matrix does allow *CP* violation. The three generation Standard Model with a single Higgs multiplet has only a single non-zero phase and it appears in the matrix which relates weak eigenstates to mass eigenstates. This is commonly known as the CKM (Cabibbo-Kobayashi-Maskawa) matrix, [KM73] which is a generalization of the four quark mixing matrix parametrized by a single (Cabibbo) angle. [Cab63]

2.3.2 The Cabibbo-Kobayashi-Maskawa Matrix

By convention, the three charge 2/3 quarks (u,c and t) are unmixed, and all the mixing is expressed in terms of a 3 × 3 unitary matrix V operating on the charge -1/3 quarks (d, s and b):

$$\begin{pmatrix} d' \\ s' \\ b' \end{pmatrix} = \begin{pmatrix} V_{ud} & V_{us} & V_{ub} \\ V_{cd} & V_{cs} & V_{cb} \\ V_{td} & V_{ts} & V_{tb} \end{pmatrix} \begin{pmatrix} d \\ s \\ b \end{pmatrix}$$

The values of individual matrix elements can in principle all be determined from weak decays of relevant quarks or from deep inelastic neutrino scattering. Using the unitarity constraint and assuming only three quark generations, the 90% confidance limits on the magnitudes of the elements of the *CKM* matrix are: [GKR97]

$$V = \begin{pmatrix} 0.9745 - 0.9760 & 0.217 - 0.224 & 0.0018 - 0.0045 \\ 0.217 - 0.224 & 0.9737 - 0.9753 & 0.036 - 0.042 \\ 0.004 - 0.013 & 0.035 - 0.042 & 0.9991 - 0.9994 \end{pmatrix}$$

There are several parametrizations of the *CKM* matrix. One proposed by Chau and Keung [CK84] ($c_{ij} = \cos\theta_{ij}$ and $s_{ij} = \sin\theta_{ij}$, with i and j being the generation labels, and a single phase $0 \leq \delta_{13} \leq 2\pi$):

$$V = \begin{pmatrix} c_{12}c_{13} & s_{12}c_{13} & s_{13}e^{-i\delta_{13}} \\ -s_{12}c_{23} - c_{12}s_{23}s_{13}e^{i\delta_{13}} & c_{12}c_{23} - s_{12}s_{23}s_{13}e^{i\delta_{13}} & s_{23}c_{13} \\ s_{12}s_{23} - c_{12}c_{23}s_{13}e^{i\delta_{13}} & -c_{12}s_{23} - s_{12}c_{23}s_{13}e^{i\delta_{13}} & c_{23}c_{13} \end{pmatrix}$$

Another useful parametrization, up to the fourth power of the Cabibbo angle λ ($\lambda \approx 0.22$, A and $\eta^2 + \rho^2$ are of $O(1)$) is due to Wolfenstein: [Wol83]

$$V = \begin{pmatrix} 1 - \frac{1}{2}\lambda^2 & \lambda & A\lambda^3(\rho - i\eta) \\ -\lambda & 1 - \frac{1}{2}\lambda^2 & A\lambda^2 \\ A\lambda^3(1 - \rho - i\eta) & -A\lambda^2 & 1 \end{pmatrix}$$

The unitarity of the *CKM* matrix leads to relations such as:

$$V_{tb}V_{td}^* + V_{cb}V_{cd}^* + V_{ub}V_{ud}^* = 0 \tag{2.5}$$

The *unitarity triangle* is a geometrical representation of this relation in the complex plane: the three complex quantities, $V_{tb}V_{td}^*$, $V_{cb}V_{cd}^*$ and $V_{ub}V_{ud}^*$ should form a triangle, as shown in Fig. 2.1. The unitarity triangle gives a relationship between the two most poorly determined entries of the *CKM* matrix, V_{ub} and V_{td}.

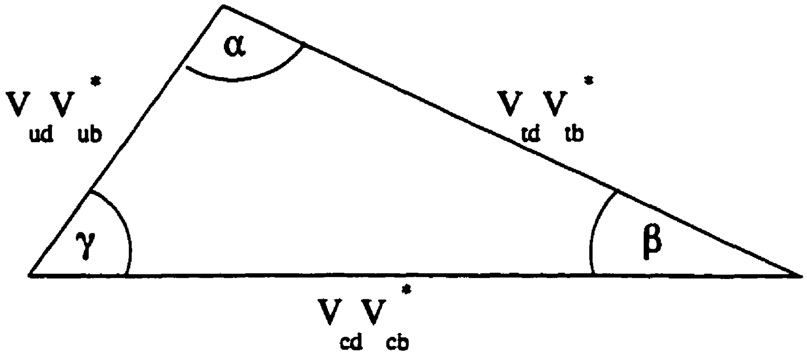

Figure 2.1: The unitarity triangle.

It is thus convenient to present constraints on the *CKM* parameters as bounds on the coordinates of the vertex A of the unitarity triangle, as in Fig. 2.2. [GKR97] The top quark mass evaluated at the relevant scale for the $B_d^0 - \bar{B}_d^0$ mixing is $m_t = 166 \pm 5 \mathrm{GeVc}^{-2}$. Note a different scale with respect to the unitarity triangle in Fig. 2.1.

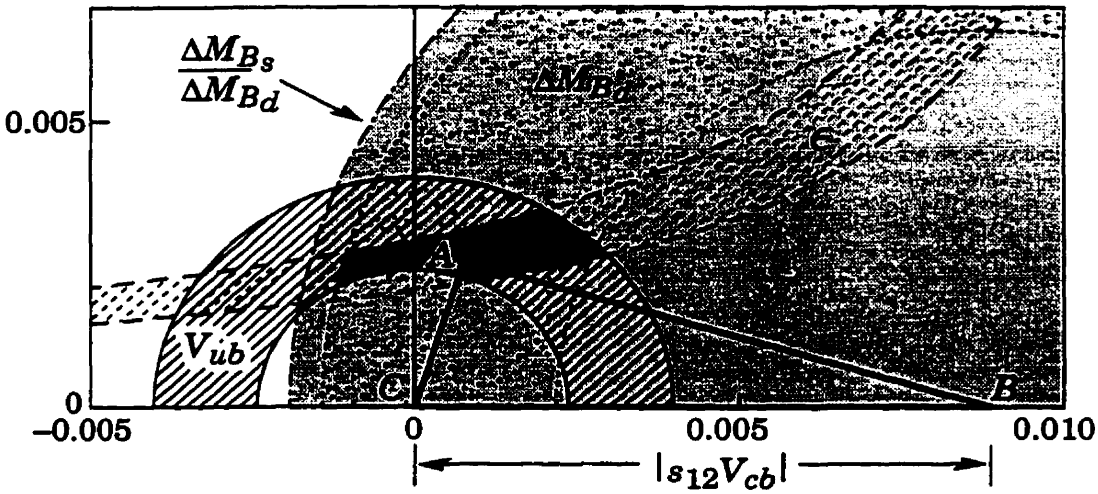

Figure 2.2: Constraints on the position of the vertex, A, of the unitarity triangle following from $|V_{ub}|$, B-mixing and ϵ. A possible unitarity triangle is shown with A in the preferred region.

The Standard Model predictions for the *CP* asymmetries in neutral B decays into certain *CP* eigenstates are fully determined by the values of the three angles, α, β and γ, of the unitarity triangle.

2.3.3 *CP* Violation in Neutral B Decays

When we consider a neutral meson B^0 and its antiparticle $\bar{B}^0$ the two mass eigenstates are B_L and B_H (meaning light and heavy, respectively):

$$|B_L> = p|B^0> + q|\bar{B}^0>$$

$$|B_H>= p|B^0> -q|\bar{B}^0> . \tag{2.6}$$

The eigenvalue equation is:

$$\left(M-\frac{i}{2}\Gamma\right)\begin{pmatrix} p \\ \pm q \end{pmatrix} = \left(M_{L,H}-\frac{i}{2}\Gamma_{L,H}\right)\begin{pmatrix} p \\ \pm q \end{pmatrix} . \tag{2.7}$$

Here M (the mass matrix) and Γ (which describes the exponential decay of the system) are 2×2 Hermitian matrices. The difference between Γ_H and Γ_L is produced by channels with branching ration $O(10^{-3})$ which contribute with alternating signs and it is safe to set $\Gamma \equiv \Gamma_L = \Gamma_H$. Also, we define $M \equiv (M_L + M_H)/2$ and $\Delta M \equiv M_H - M_L$. As $\Gamma_{12} \ll M_{12}$ gives $|p/q| = 1$ the proper time evolution of states which at time t=0 were either pure B^0 or pure $\bar{B}^0$ is given by:

$$\begin{aligned} |B^0_{phys}> &= e^{(-\frac{\Gamma}{2}-iM)t}\cos\frac{\Delta Mt}{2}|B^0> + \frac{p}{q}ie^{(-\frac{\Gamma}{2}-iM)t}\sin\frac{\Delta Mt}{2}|\bar{B}^0> \\ |\bar{B}^0_{phys}> &= \frac{p}{q}ie^{(-\frac{\Gamma}{2}-iM)t}\sin\frac{\Delta Mt}{2}|B^0> + e^{(-\frac{\Gamma}{2}-iM)t}\cos\frac{\Delta Mt}{2}|\bar{B}^0> . \end{aligned} \tag{2.8}$$

Since we are interested in the decay of neutral B mesons into a *CP* eigenstate, which we denote by f_{CP}, we define the following amplitudes:

$$A \equiv < f_{CP}|H|B^0>, \bar{A} \equiv < f_{CP}|H|\bar{B}^0> . \tag{2.9}$$

The time-dependent rates for initially pure B^0 or $\bar{B}^0$ states to decay into *CP* eigenstates are:

$$\begin{aligned} \Gamma(B^0_{phys}(\bar{B}^0_{phys}) \rightarrow f_{CP}) = |A|^2 e^{-\Gamma t}\Bigg[\frac{1+|\lambda|^2}{2} \pm \frac{1-|\lambda|^2}{2}\cos(\Delta Mt) \\ \mp \mathrm{Im}\lambda\ sin(\Delta Mt)\Bigg] \end{aligned} \tag{2.10}$$

where

$$\lambda \equiv \frac{q}{p}\frac{\bar{A}}{A}. \tag{2.11}$$

The time-dependent *CP* asymmetry, which is defined as:

$$a_{f_{cp}}(t) \equiv \frac{\Gamma(B^0_{phys}(t) \rightarrow f_{CP}) - \Gamma(\bar{B}^0_{phys}(t) \rightarrow f_{CP})}{\Gamma(B^0_{phys}(t) \rightarrow f_{CP}) + \Gamma(\bar{B}^0_{phys}(t) \rightarrow f_{CP})} \tag{2.12}$$

is given by:

$$a_{f_{cp}}(t) = \frac{(1-|\lambda|^2)\cos(\Delta M t) - 2\mathrm{Im}\lambda \sin(\Delta M t)}{1+|\lambda|^2}. \tag{2.13}$$

The quantity $\mathrm{Im}\lambda$ which can be extracted from $a_{f_{cp}}(t)$ can be directly related to the *CKM* matrix elements in the Standard Model. In the general case:

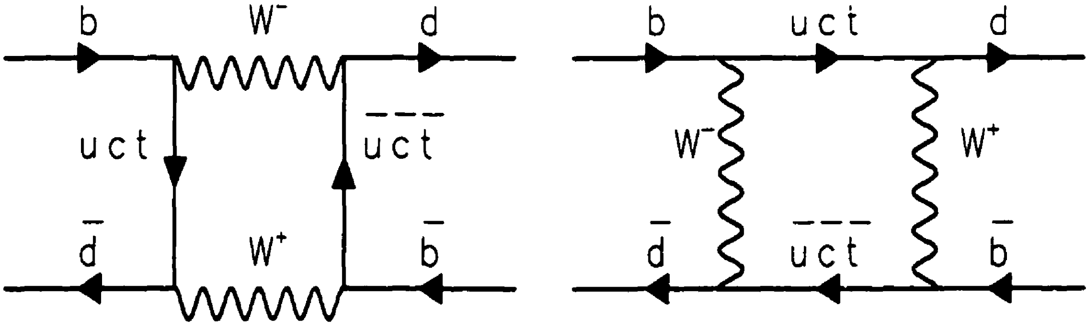

Figure 2.3: Feynman diagrams responsible for $B^0 - \bar{B}^0$ mixing.

$$A = \sum_i A_i e^{i\delta_i} e^{i\phi_i}, \quad \bar{A} = \sum_i A_i e^{i\delta_i} e^{-i\phi_i}, \tag{2.14}$$

where A_i are real, ϕ_i are *CKM* phases and δ_i are strong phases. If all amplitudes that contribute to the direct decay have the same *CKM* phase, such that $\bar{A}/A = e^{-2i\phi_D}$ and if $q/p = e^{-2i\phi_M}$, where ϕ_M is the *CKM* phase in the $B - \bar{B}$ mixing (the relevant Feynman diagrams are shown in Fig. 2.3), then Eq. 2.13 simplifies considerably:

$$a_{f_{cp}}(t) = -\mathrm{Im}\lambda \sin(\Delta M t)$$

$$\lambda = e^{-2i(\phi_D+\phi_M)} \Rightarrow \mathrm{Im}\lambda = -\sin 2(\phi_D + \phi_M) \tag{2.15}$$

CP asymmetries in $B^0 \to f_{cp}$ provide a way to measure the angles of the unitarity triangle, which are defined by:

$$\alpha \equiv \arg\left(-\frac{V_{td}V_{tb}^*}{V_{ud}V_{ub}^*}\right), \quad \beta \equiv \arg\left(-\frac{V_{cd}V_{cb}^*}{V_{td}V_{tb}^*}\right), \quad \gamma \equiv \arg\left(-\frac{V_{ud}V_{ub}^*}{V_{cd}V_{cb}^*}\right). \tag{2.16}$$

The aim is to 'overdetermine' the unitarity triangle, to make enough independent measurements of the sides and the angles and thus check the validity of the Standard Model. Table 2.3 [NQ92] lists *CP* asymmetries for various channels in B_d (left) and B_s (right) decays. One possible hadronic final state is listed for each specific quark decay. Standard Model predictions for the parameter Imλ (in terms of the unitarity triangle angles) are given in the last columns.

Quark process	Final state	Imλ	Quark process	Final state	Imλ
$\bar{b} \to \bar{c}c\bar{s}$	ψK_S	$-\sin 2\beta$	$\bar{b} \to \bar{c}c\bar{s}$	$\psi\phi$	0
$\bar{b} \to \bar{c}c\bar{d}$	D^+D^-	$-\sin 2\beta$	$\bar{b} \to \bar{c}c\bar{d}$	ψK_S	0
$\bar{b} \to \bar{u}u\bar{d}$	$\pi^+\pi^-$	$\sin 2\alpha$	$\bar{b} \to \bar{u}u\bar{d}$	ρK_S	$-\sin 2\gamma$
$\bar{b} \to \bar{s}s\bar{s}$	ϕK_S	$-\sin 2\beta$	$\bar{b} \to \bar{s}s\bar{s}$	$\eta'\eta'$	0
$\bar{b} \to \bar{s}s\bar{d}$	$K_S K_S$	0	$\bar{b} \to \bar{s}s\bar{d}$	ϕK_S	$\sin 2\beta$
$\bar{b} \to \bar{c}u\bar{s}, \bar{u}c\bar{s}$	$D^0_{CP}K^{*0}$	$\sin\gamma$			

Table 2.3: *CP* asymmetries in B_d and B_s decays.

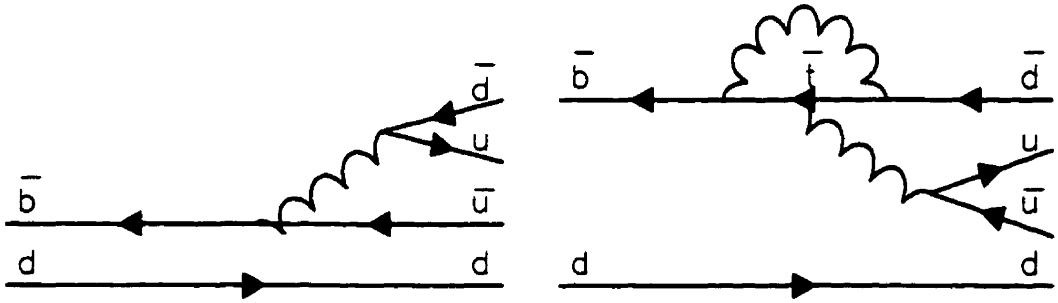

Figure 2.4: Feynman diagrams, tree (left) and penguin (right) for the $B^0_d \to \pi^+\pi^-$ decay.

It is important that only one weak amplitude contributes to a decay if one is to cleanly extract the *CP* phases using indirect *CP* violation. A problem arises since many B decays have more than one such contribution. In addition to tree diagrams, penguin diagrams are often present. This is the case in the decay $B_d^0 \to \pi^+\pi^-$ (both Feynman diagrams for this decay are shown in Fig 2.4), which is one of the interesting CP eigenstates. Here, the tree diagram has the weak phase $V_{ub}^* V_{ud}$, while that of the penguin diagram is $V_{tb}^* V_{td}$. Therefore, for this decay, in addition to indirect CP violation, direct CP violation is present due to the interference between two types of diagrams. This spoils the cleanliness of the measurement of the CP asymmetries, hence the term 'penguin pollution'. Thus, the measurement of CP asymmetry in this mode does not give $\sin 2\alpha$, as advertised before, but $\sin(2\alpha + \theta_{+-})$, where θ_{+-} depends on weak and strong phases of the tree and penguin diagrams as well as on their relative sizes. It should be noted that this problem does not arise in all modes. For example, in $B_d \to \Psi K_S^0$ both tree and penguin diagrams have the same weak phases so there is no interference, and in $B_s \to D_s^\pm K^\mp$ there are no penguin contributions.

2.3.4 *CP* Violation in Charged *B* Decays

In charged B decays one may look for the CP violating asymmetries of the form:

$$a_f \equiv \frac{\Gamma(B^+ \to f) - \Gamma(B^- \to \bar{f})}{\Gamma(B^+ \to f) + \Gamma(B^- \to \bar{f})} \tag{2.17}$$

where f is any final state and $\bar{f}$ is its CP conjugate. Although CPT theorem requires that the total B^+ and B^- decay widths are the same, specific channels or sums over channels can contribute to the above asymmetry. For this to happen there must be interference between two separate amplitudes that contribute to the decay with different weak phases, $\phi_1 \neq \phi_2$, and with different strong phase shifts, $\delta_1 \neq \delta_2$. In that case:

$$a_f \propto \sin(\delta_1 - \delta_2)\sin(\phi_1 - \phi_2) \tag{2.18}$$

It was recognized [BSS79] that, within the Standard Model, these conditions can be readily met in three types of B decays: *(i)* *CKM* suppressed decays where tree amplitudes can interfere with penguin type amplitudes, *(ii)* *CKM* forbidden decays, which have no tree contributions but there can be interference of penguin contributions with different charge 2/3 quarks in the loop, and *(iii)* Radiative decays, similar to *(ii)* but the leading contribution is an electromagnetic penguin (the gluons are replaced by a single photon line).

2.3.5 Beyond the Standard Model

The above discussion assumes that the only source of *CP* violation is the phase of the *CKM* matrix. Models beyond the Standard Model involve other phases and, consequently, the measurements of the *CP* asymmetries may violate the constraints of the unitarity triangle. Even in the absence of new *CP* violating phases the sides of the triangle may be affected by new contributions. In certain models, such as four-generation model and models involving Z-mediated flavor-changing neutral currents, the unitarity triangle turns into a quadrangle.

Through a measurement of the *CP* asymmetries, the presence of new physics can be detected in several ways: *(i)* the relation $\alpha + \beta + \gamma = \pi$ is violated, *(ii)* even if $\alpha + \beta + \gamma = \pi$ value for the *CP* phase can be outside of the Standard Model predictions, *(iii)* the CP angles are consistent with the Standard Model predictions but are inconsistent with the measured sides of the unitarity triangle.

Any additional information on the *CP* violation in and beyond the Standard Model can be found in a myriad of books and review publications on theoretical particle physics. The ones used in the preparation of this introductory chapter are: [NQ92], [Gro96], [Lon96], [Kay96], [WN96] and [Bur97].

2.4 Specific Ionization - dE/dx

2.4.1 Theory

This section is a summary of the theoretical description of the particle energy loss in matter. It was taken from *Introduction to Experimental Particle Physics*, by R.C.Fernow [Fer86], *Particle Detectors*, by C.Grupen [Gru96], and *Review of Particle Physics*, published by The American Physical Society [WN96].

Charged particles passing through matter lose kinetic energy by excitation of bound electrons and by ionization. The later process is of greater importance as the atomic electrons are liberated from the atom and can be subsequently detected.

Given the momentum of the incident particle $p = \gamma m_0 \beta c$ (where γ is the Lorentz factor, $\beta c = v$ and m_0 is the rest mass of the particle) the maximum energy that might be transferred to an atomic electron (mass m_e) in a medium is given by [Ros52]:

$$E_{kin}^{max} = \frac{2m_e c^2 \beta^2 \gamma^2}{1 + 2\gamma \frac{m_e}{m_0} + (\frac{m_e}{m_0})^2} = \frac{2m_e p^2}{m_0^2 + m_e^2 + \frac{2m_e E}{c^2}}, \tag{2.19}$$

where the kinetic energy E_{kin} is related to the total according to $E_{kin} = E - m_0 c^2$. If one neglects the quadratic term in Eq. 2.19, which is a good approximation for all incident particles other than electrons, it follows that:

$$E_{kin}^{max} = \frac{p^2}{\gamma m_0 + \frac{m_0^2}{2m_e}}. \tag{2.20}$$

For relativistic particles $E_{kin} \approx E \approx pc$ and the maximum transferable energy becomes:

$$E^{max} = \frac{E^2}{E + \frac{m_0^2 c^2}{2m_e}}. \tag{2.21}$$

If the incident particle is an electron, these approximations are no longer valid. In this case Eq. 2.19 reduces to:

$$E_{kin}^{max} = \frac{p^2}{m_e + \frac{E}{c^2}} = \frac{E^2 - m_e^2 c^4}{E + m_e c^2} = E - m_e c^2, \tag{2.22}$$

which is expected for a central collision of two classical particles of equal mass.

The average energy loss dE per 'length' dx for 'heavy' particles in semi-classical approximation is given by Bethe-Bloch formula [Bet30, Bet32, Blo33]:

$$-\frac{dE}{dx} = 2\pi N_A r_e^2 m_e c^2 z^2 \frac{Z}{A}\frac{1}{\beta^2}\left[ln\frac{2m_e c^2\gamma^2\beta^2 E^{max}}{I^2} - 2\beta^2 - \delta\right], \tag{2.23}$$

where

z - charge of the incident particle in units of elementary charge

Z, A - atomic number and atomic weight of the absorber

m_e - electron mass

r_e - classical electron radius ($r_e = \frac{1}{4\pi\epsilon_0}\frac{e^2}{m_e c^2}$)

N_A - Avogadro number ($6.022 \times 10^{23}\mathrm{mol}^{-1}$)

I - ionization energy of the absorber material which can be approximated by $I = 16Z^{0.9}\mathrm{eV}$ for $Z > 1$

δ - a parameter which describes how much the extended transverse electric field of incident relativistic particles is screened by the effective charge density of the atomic electrons. For energetic particles $\delta \approx 2\ln\gamma + \zeta$, where ζ is a material dependent constant.

The energy loss is usually given in units of $\frac{\mathrm{MeV}}{\mathrm{g\ cm^{-2}}}$. The length unit g cm^{-2} is commonly used because the energy loss per surface mass density (which is dx as defined above) is largely independent of the properties of the material. Eq. 2.23 is an approximation which is precise to the level of a few percent up to energies of several hundred GeV, but it cannot be used for slow particles which move with velocities comparable to, or less than, those of atomic electrons.

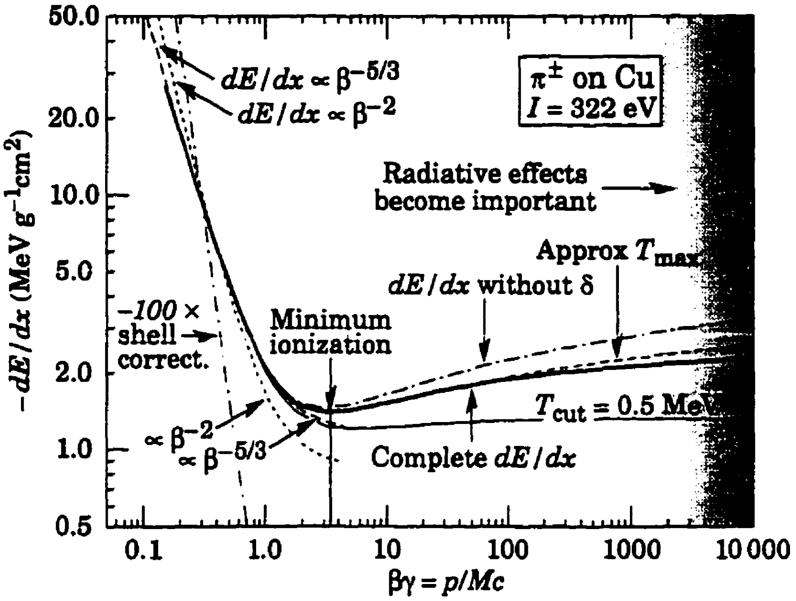

Figure 2.5: Energy loss rate in copper as a function of $\beta\gamma$ of incident pions [WN96].

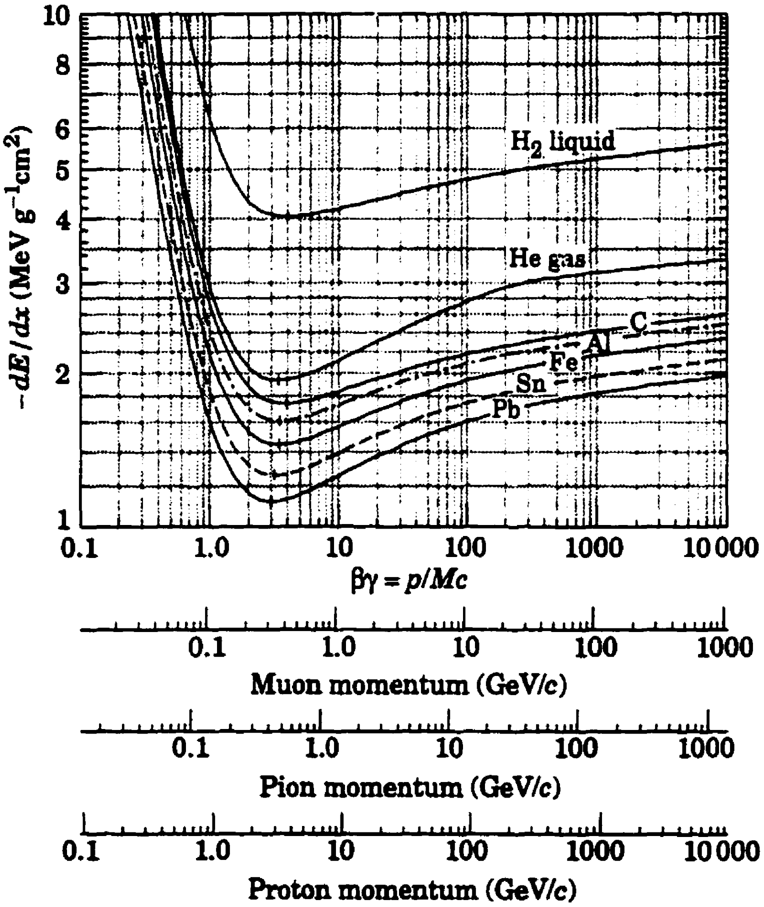

Figure 2.6: Energy loss rate for various materials and several particle species as a function of incident particle momentum [WN96].

Figure 2.5 [WN96] shows the energy loss rate as calculated for an incident pion passing through copper. (Note the difference in energy notation between the figure and the text: $T_{max} \equiv E^{max}$ and $T_{cut} \equiv E_{cut}$). In the low energy domain the energy loss decreases like β^{-q} where q ranges between 2/3 and 3. It reaches a broad minimum of ionization at $\beta\gamma \approx 3.5$. Relativistic particles which have an energy loss in this region are called 'minimum-ionizing particles'. The energy loss increases again because of the logarithmic term in the brackets of Eq. 2.23. This equation only describes energy losses due to ionization and excitation of the atomic electrons in the medium.

Figure 2.6 [WN96] shows the energy loss rate for several spicies of incident particles, as a function of the incident particle momentum, passing through liquid hydrogen, gaseous helium, carbon, aluminum, tin and lead.

At high energies radiation losses, which are not included in the Bethe-Bloch formula, become more and more important, as the rate of energy loss due to bremsstrahlung [Ros52]:

$$-\frac{dE}{dx} = 4\alpha N_A \frac{Z^2}{A} z^2 E \left[\frac{1}{4\pi\epsilon_0}\frac{e^2}{m_e c^2}\right]^2 \ln\frac{183}{Z^{\frac{1}{3}}}, \tag{2.24}$$

begins to dominate the total rate of energy loss at very high energies (E¿1TeV for particle more massive than the electron).

Equation 2.23 gives only the average energy loss of charged particles. For thin absorbers, i.e., mainly in gases, strong fluctuations around the average energy loss exist. The energy loss distribution for thin absorbers is strongly asymmetric and can be parametrized by a Landau distribution, see Fig. 2.7. A reasonable approximation of the Landau distribution is given by [B⁺84]:

$$L(\lambda) = \frac{1}{\sqrt{2\pi}} \times \exp\left[-\frac{1}{2}(\lambda + e^{-\lambda})\right], \tag{2.25}$$

where λ is the deviation from the most probable energy loss:

$$\lambda = \frac{\Delta E - \Delta E^W}{\xi}, \tag{2.26}$$

$$\xi = 2\pi N_A r_e^2 m_e c^2 z^2 \frac{Z}{A} \frac{1}{\beta^2} \rho x. \tag{2.27}$$

ΔE - actual energy loss in a layer of a given thickness,

ΔE^W - most probable energy loss in the same layer,

ρ - density of the traversed material in g cm-3

x - thickness of the material in cm.

r_e - the classical electron radius in cm.

The Landau fluctuations of the energy loss are related to a large extent to very high energy transfers to atomic electrons, which allow escape and are called δ or knock-on electrons. The strong fluctuations of the energy loss are quite frequently not observed by a detector, as detectors only measure the energy which is deposited in their sensitive volume, and this energy may not be the same as the energy lost by the particle. Some of the δ electrons may leave the sensitive volume before depositing all of their energy. Therefore, it is quite often of practical interest to consider only the energy loss with energy transfers E smaller than some cut-off value E_{cut}. The 'mean' for this truncated energy loss distribution is given by [WN96]:

$$-\frac{dE}{dx} = 2\pi N_A r_e^2 m_e c^2 z^2 \frac{Z}{A} \frac{1}{\beta^2} \left[ln \frac{2m_e c^2 \beta^2 \gamma^2 E_{cut}}{I^2} - \beta^2 - \delta \right]. \tag{2.28}$$

The truncated energy loss distribution does not show as pronounced Landau tail as distribution of Eq. 2.23. Because of the density effect, expressed by δ, the mean energy loss of the truncated distribution approaches a constant at high energies, which is called the Fermi plateau.

So far, only the energy loss of the 'heavy' particles was discussed. Electrons, as the incident particles require special treatment as: *(i)* even at low energies, the energy loss is influenced by bremsstrahlung, and *(ii)* the mass of the incident particle and the target electron are the same. The equivalent of Eq. 2.23 for electrons, which also takes into consideration the kinematics of the electron-electron collisions and the screening effects, is [MRRS88]:

$$-\frac{dE}{dx} = 4\pi N_A r_e^2 m_e c^2 \frac{Z}{A}\frac{1}{\beta^2}\left[\ln\frac{\gamma m_e c^2 \beta\sqrt{\gamma-1}}{\sqrt{2}I} + \frac{1}{2}(1-\beta)^2 - \frac{2\gamma-1}{2\gamma^2}\ln 2 + \frac{1}{16}\left(\frac{\gamma-1}{\gamma}\right)^2\right]. \tag{2.29}$$

The ionization energy loss of a 250MeV electron in a 1cm gaseous argon layer is shown in Fig. 2.7, where we have used: $\Delta E^W = 2.4$keV and $\xi = 0.125$keV [Gru96].

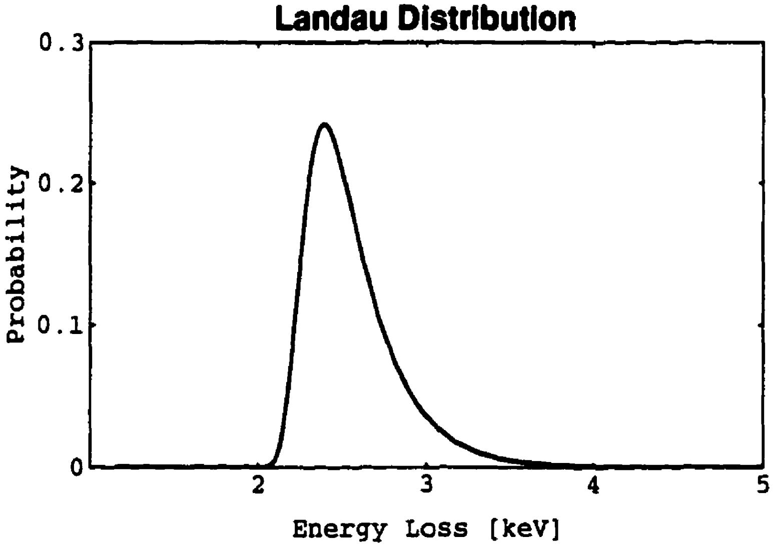

Figure 2.7: Landau distribution for the ionization energy loss of 250MeV electrons in 1cm of gaseous argon.

Finally, the energy loss in a compound of various elements i is given by:

$$\frac{dE}{dx} \approx \sum_i f_i \left.\frac{dE}{dx}\right|_i , \tag{2.30}$$

where f_i is the mass fraction of the i-th element and $\left.\frac{dE}{dx}\right|_i$ the average energy loss rate in that element. Corrections to this relation due to the dependence of the ionization constant on the molecular structure can be safely neglected, provided that one does not have $\beta \leq 10^{-2} - 10^{-3}$.

2.4.2 Applications of dE/dx to Particle Identification in Drift Chambers

It should be realized that the specific energy loss rate, Eq. 2.23, depends on the incident particle's electric charge and velocity, but *not* on its mass. Therefore, if one is able to simultaneously measure curvature of the track and the deposited ionization energy associated with the track, the incident particle can be identified in the following way. The curvature of the track, as obtained from the fit of the drift chamber hits, yields the momentum of the particle, as well as the sign of its electric charge. If the path a particle has traversed in the drift chamber is known (and it is, after the track fit is done) the measurements of the 'total' energy loss of the particle give the rate of energy loss (dE/dx) and, finally, the particle's velocity. The momentum and the velocity of a given particle are sufficient to unambiguously determine its mass, therefore, the incident particle is identified. Figure 2.8 shows the specific ionization energy loss rate for incident kaons and pions in copper. Note the expanded vertical scale compared to Fig. 2.5. The horizontal axis is the momentum rather than $\beta\gamma$ factor of Fig. 2.5. The incident particle momentum ranges between 0 and 3GeVc^{-1}. dE/dx was calculated using Eq. 2.23 with the ionization energy of copper I_{Cu} = 322eV [WN96]. All the 'density effects' (the δ term) were neglected. Note that the two curves cross at the momentum of $\approx$ 0.9GeVc^{-1}.

A fundamental problem of this procedure arises from the fact that, beyond certain momenta, energy loss rates of different particle species, pions and kaons for example (Fig. 2.8), overlap due to instrumantal resolution. Particle identification

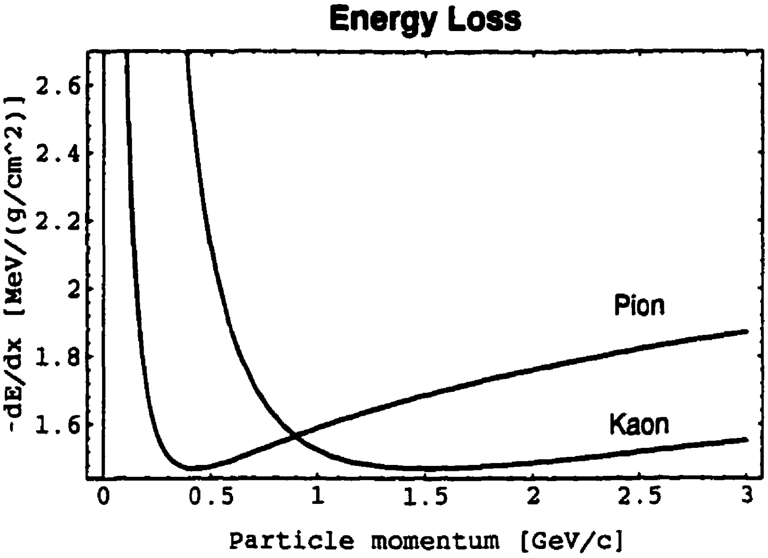

Figure 2.8: Specific ionization of kaons and pions in copper, as a function of their momentum.

using the dE/dx method becomes impossible in that momentum range.

Chapter 3

BaBar Experiment

This chapter is a brief review of the BaBar Technical Design Report [Col95]. Other references are quoted where necessary.

3.1 Motivation

While it has been understood for several years that the measurement of CP violating asymmetries in B^0 decays could lead to important tests of the CKM matrix, the experiments seemed beyond reach. The discovery of a surprisingly long b quark lifetime together with a large $B^0 - \bar{B}^0$ mixing made it possible to contemplate such experiments. It soon became clear that the most straightforward approach involved experiments at a variety of e^+e^- machines, either in the $\Upsilon(4S)$ region (10.58GeV), in the PEP/PETRA continuum region, or at the Z^0 pole (91.19GeV).

The most favorable e^+e^- experimental situation, which is the one producing the smallest statistical error with the least integrated luminosity, is the asymmetric storage ring first proposed by Oddone. [Odd87] This machine would boost the decaying B^0 mesons in the laboratory frame, allowing existing vertex measuring technology to measure the time order of $B^0 - \bar{B}^0$ decay pairs (remember that in order to extract the CP violating parameter Imλ from the measured asymmetry, see Eq. 2.15, one needs to know the time t between the two B^0 decays) even with the short B meson flight distance.

PEP-II collider, at Stanford Linear Accelerator Center (SLAC), in Stanford, California, promises to provide the required luminosity, initially $3 \times 10^{33}\mathrm{cm}^{-2}\mathrm{s}^{-1}$, ultimately 10^{34}, with asymmetric $\Upsilon(4S)$ production at a $\beta\gamma = 0.56$) (9GeV electrons on 3.1GeV positrons). The $B\bar{B}$ production rate will be 3Hz at the initial luminosity, rising to 10Hz. The experimental challenge is then to provide high efficiency, high resolution exclusive state reconstruction in a situation new to the e^+e^- collider world: a center of mass in motion in the laboratory.

The primary goal of the BaBar experiment is the systematic study of CP violation in neutral B decays, as discussed in the previous chapter. The secondary goals are to explore the wide range of other B physics, charm physics, τ physics, two-photon physics and Υ physics that becomes available with the high luminosity of PEP-II.

The critical experimental objectives to achieve the required sensitivity for CP measurements are: [Col95]

- To reconstruct the decays of B^0 mesons into a wide variety of exclusive final states with high efficiency and low background.

- To tag the flavor of the other B meson in the event with high efficiency and purity.

- To measure the relative decay time of the two B mesons.

3.2 The Experimental Setup

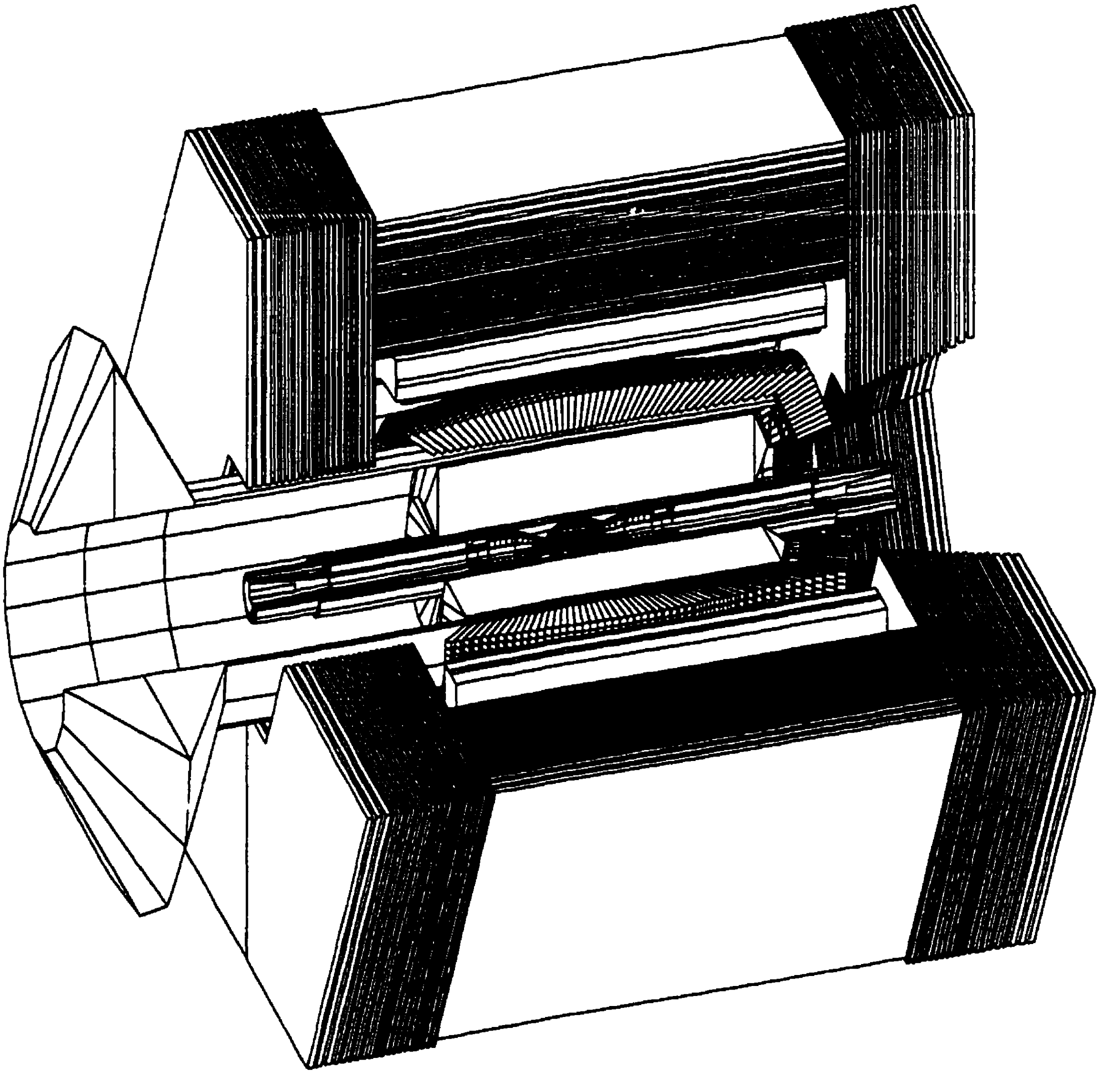

Figure 3.1: 3D view of the BaBar detector.

The BaBar experimental design is shown in Fig. 3.1 and a summary of the individual detector components is given in Table 3.1. It consists of a silicon vertex detector, a drift chamber, a particle identification system, a CsI electromagnetic calorimeter, and a magnet with an instrumented flux return. The superconducting solenoid is designed for a magnetic field of 1.5T, and the flux return is instrumented for muon identification and coarse hadron calorimetry. All of those detectors

Detector	Technology	Dimensions	Performance
SVT	Double-sided Silicon Strip	5 Layers $r = 3.2 - 14.4\text{cm}$ $-0.87 < \cos\theta < 0.96$	$\sigma_z = \sigma_{xy} =$ $= 50\mu\text{m}/p_t \oplus 15\mu\text{m}$ $\sigma_\phi = \sigma_\theta = 1.6\text{mr}/p_t$
DC	Small Cell Drift Chamber	40 Layers $r = 22.5 - 80.0\text{cm}$ $-111\text{cm} < z < 166\text{cm}$	$\sigma(p_t)/p_t =$ $= 0.21\% + 0.14\% \times p_t$
PID	DIRC	$1.75 \times 3.5\text{cm}^2$ quartz $-0.84 < \cos\theta < 0.90$	$N_{pe} = 20 - 50$ $\geq 4\sigma$ K/π separation
CAL	CsI(Ti)	$16 - 17.5$ X_0 $\sim 4.8 \times 4.8\text{cm}$ crystals	$\sigma_E/E = 1\%/E^{\frac{1}{4}} \oplus 1.2\%$ $\sigma_\theta = 3\text{mr}/\sqrt{E} \oplus 2\text{mr}$
MAG	Superconducting Segmented Iron	$IR = 1.40\text{m}$ $L = 3.85\text{m}$	$B = 1.5\text{T}$
IFR	RPC	16-17 Layers	$\epsilon_\mu > 90\%$ for $p_\mu > 0.8\text{GeVc}^{-1}$

Table 3.1: The BaBar detector - parameter summary.

operate with good performance for laboratory polar angles between 17^0 and 150^0, corresponding to the range $-0.95 < \cos\theta_{cm} < 0.87$ (due to the Lorentz boost, the center of mass frame does not coincide with the laboratory frame).

The detector coordinate system is defined with $+z$ in the boost (high energy beam) direction. The origin is the nominal collision point, which is offset in the $-z$ direction from the geometrical center of the detector magnet.

The tracking system in BaBar consists of the vertex detector and a drift chamber. The vertex detector is used to precisely measure both impact parameters for charged tracks (z and $r - \phi$). These measurements are used to determine the difference in decay times of two B^0 mesons. Charged particles with transverse momentum (p_t) between $\sim$ 40MeV/c and $\sim$ 100MeV/c are tracked only with the vertex detector, which must therefore provide good pattern recognition.

The drift chamber (extending from 22.5cm in radius to 80cm) is used primarily to achieve excellent momentum resolution and pattern recognition for charged particles with $p_t > 100$MeV/c. It also supplies information for the charged track trigger and a measurement of dE/dx for particle identification. The optimum resolution is achieved by having a continuous tracking volume with a minimum amount of material to cause multiple scattering. By using helium-based gas mixture with low mass wires and a magnetic field of 1.5T very good momentum resolution can be obtained. The chamber is designed to minimize the amount of material in front of the particle identification and calorimeter systems in the heavily populated forward direction. The readout electronics are mounted only on the backward end of the chamber.

Two primary goals for the particle identification system are to identify kaons for tagging beyond the momentum range in which dE/dx separation works well, and to identify pions from few body decays such as $B^0 \to \pi^+\pi^-$ and $B^0 \to \rho\pi$. A new detector technology is needed to meet these goals and in the barrel region a DIRC (Detector of Internally Reflected Čerenkov radiation) is used. Čerenkov light produced in quartz bars is transferred by total internal reflection to a large water tank outside of the backward end of the magnet. The light is observed by an array of photomultiplier tubes, where images governed by the Čerenkov angle are formed. This arrangement provides at least 4 standard deviation π/K separation up to almost the kinematic limit for particles from B decays.

The electromagnetic calorimeter must have superb energy resolution down to very low photon energies. This is provided by a fully projective CsI(Ti) crystal calorimeter. The barrel calorimeter contains 5880 trapezoidal crystals; the endcap calorimeter contains 900 crystals. The crystal length varies from $17.5X_0$ (X_0 is the radiation length) in the forward endcap to $16X_0$ in the backward part of the barrel. Electronic noise and beam related backgrounds dominate the resolution at low photon energies, while shower leakage from the rear of the crystals dominates at higher energies.

To achieve very good momentum resolution at 'high' momenta without increasing the tracking volume, and therefore the calorimeter cost, it is necessary to have a field of 1.5T. The magnet is therefore of superconducting design. The magnet is similar to many operating detector magnets, so the engineering and fabrication should be straightforward. The segmentation of the iron for an Instrumented Flux Return (IFR), and the need for the DIRC readout in the backward region cause some design complications.

The IFR is designed to identify muons with momentum around 0.5Gev/c and to detect neutral hadrons (such as K^0_Ls). The magnet flux return is divided into layers between which are gaps with Resistive Plate Chambers (RPC), which serve as active detectors. The RPCs represent a proven technology which adapts well to the BaBar geometry.

The high data rate at PEP-II requires a data acquisition system which is more advanced than those used at present e^+e^- experiments. The rate of processes to be recorded at the design luminosity of $3 \times 10^{33}\mathrm{cm}^{-2}\mathrm{s}^{-1}$ is about 100Hz (the bunch crossing period is 4.2ns), except for Bhabha events which have to be 'scaled'. Simulations of machine backgrounds show hit rates of about 100kHz per layer in the inner region of the drift chamber and about 140MHz in the first silicon layer. The goal is to operate with negligible dead time even if the backgrounds are 10 times higher than present estimates, which might happen early in the life of the experiment.

3.3 Gas Choice and Properties

The choice of gas for the drift chamber is driven primarily by the needs to reduce the total amount of the material, minimize multiple scattering for low momentum tracks, and to operate efficiently in a 1.5T magnetic field.

Gas Mixture	X_0 (m)	Primary Ions (cm^{-1})	v_d (μm/ns)	θ_L (deg)	dE/dx Resol. (%)
$Ar : CO_2 : CH_4$(89:10:1)	124	23.6	49	52	7.3
$He : DME$(70:30)	723	22.4	6	8	6.7
$He : C_4H_{10}$(80:20)	807	21.2	22	32	6.9
$He : CO_2 : C_4H_{10}$(83:10:7)	963	13.8	19	26	8.5

Table 3.2: Properties of various gas mixtures at atmospheric pressure and 20°C.

Gas Mixture	p for 3σ (MeV/c)	# of σ at 2.6GeV/c
$Ar : CO_2 : CH_4$(89:10:1)	665	2.4
$He : DME$(70:30)	720	2.1
$He : C_4H_{10}$(80:20)	710	2.1
$He : CO_2 : C_4H_{10}$(83:10:7)	660	1.7

Table 3.3: K/π separation for various gas mixtures.

These requirements are well satisfied by mixtures of helium and hydrocarbons. Mixtures with 10-30% of various hydrocarbons afford a small Lorentz angle (the angle between electron drift velocity and the electric field), good resolution and

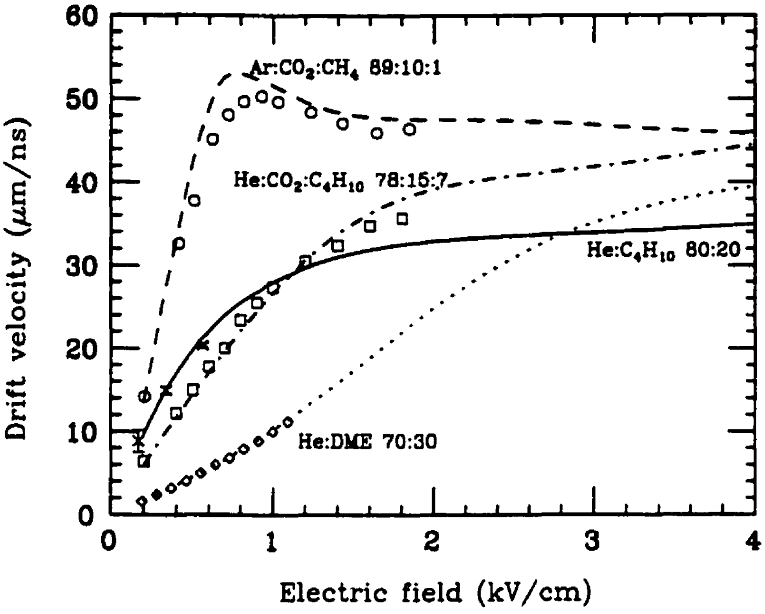

Figure 3.2: Calculated and measured drift velocities as a function of electric field for a zero magnetic field.

low multiple scattering. Tables 3.2 and 3.3 show the properties of gases which have been considered for the BaBar drift chamber.

The drift velocities and Lorentz angles are determined with the Boltzmann integration code [Bia89] and the dE/dx calculations were performed with a modified version of a program by Va'vra [VRFC82]. Note that the helium mixtures have a radiation length more than five times larger than that of $Ar : CO_2 : CH_4$(89:10:1), a commonly used argon-based mixture.

Fig. 3.2 shows the calculated drift velocity vs. electric field for four gases in the table. The results are from [PBES92] ($He : C_4H_{10}$), [BBB92] ($He : CO_2 : C_4H_{10}$ and $Ar : CO_2 : CH_4$), [C+91] ($He : DME$). The helium based mixtures lead to better performance than typical argon mixtures since the smaller Lorentz angle results in a more uniform distance-time relation.

The results for the spatial resolution are summarized in Fig. 3.3. Points represent the data from prototype chamber while curves are results of other studies. [PBES92, C^{+}91, U^{+}93] The $He : C_4H_{10}$(80:20) mixture was chosen for the BaBar drift chamber based on the measured spatial resolution and simulated dE/dx resolution. The aging studies were performed with a small proportional counter and an Fe^{55} source, and the isobutane mixture showed negligible aging. Long term aging studies are under way.

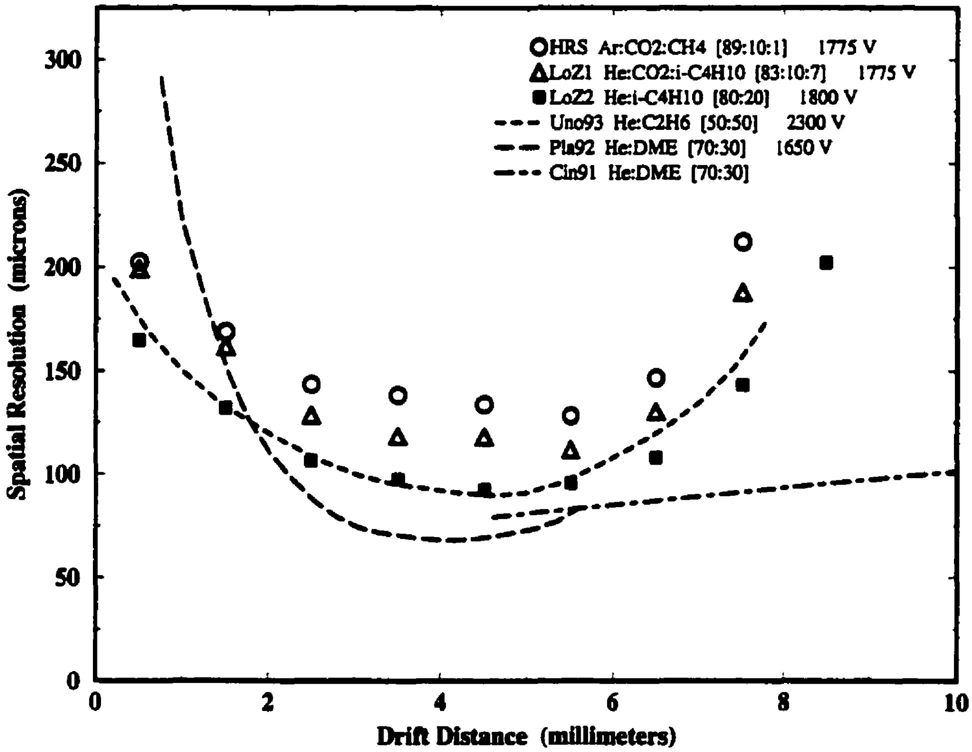

Figure 3.3: Spatial resolution for various gasses from the prototype drift chamber (points) and from other studies (curves).

Chapter 4

Small Scale Drift Chamber

A small scale drift chamber prototype was built by members of the BaBar group at Laboratoire d'Annecy-le-Vieux de Physique des Particules (LAPP), Annecy-le-Vieux, France. This chamber was used for subsequent test-beam experiments at the Proton Synchrotron (PS), CERN (August 1997) and at PSI, Zurich (October 1997). The goal was to study the specific ionization (dE/dx) of the Helium-Isobutane gas mixture (80%He 20%C_4H_{10}) which is to be used in the actual BaBar drift chamber.

4.1 Prototype Drift Chamber Description

The prototype drift chamber is a cylinder of radius ≈5.5cm and of length ≈17.5cm. It consists of 34 hexagonal cells (each cell is a right hexagonal prism of length 17.5 cm). This geometry closely resembles the mid layers of the BaBar drift chamber. Sense wires (gold plated tungsten, 20 micron diameter) are centered at the middles of each cell and are kept at a potential of positive 1650 Volts. Field wires (berylium, 100 micron diameter) positioned at the vertices of hexagons are

kept at a constant potential of 0 Volts thus creating an electric field attracting the deposited electric charge toward the sense wires. Fig. 4.1 shows a two dimensional (z-x plane, with +z being along the incident beam direction, note that this does not correspond to the BaBar coordinate system) view of the small scale drift chamber prototype.

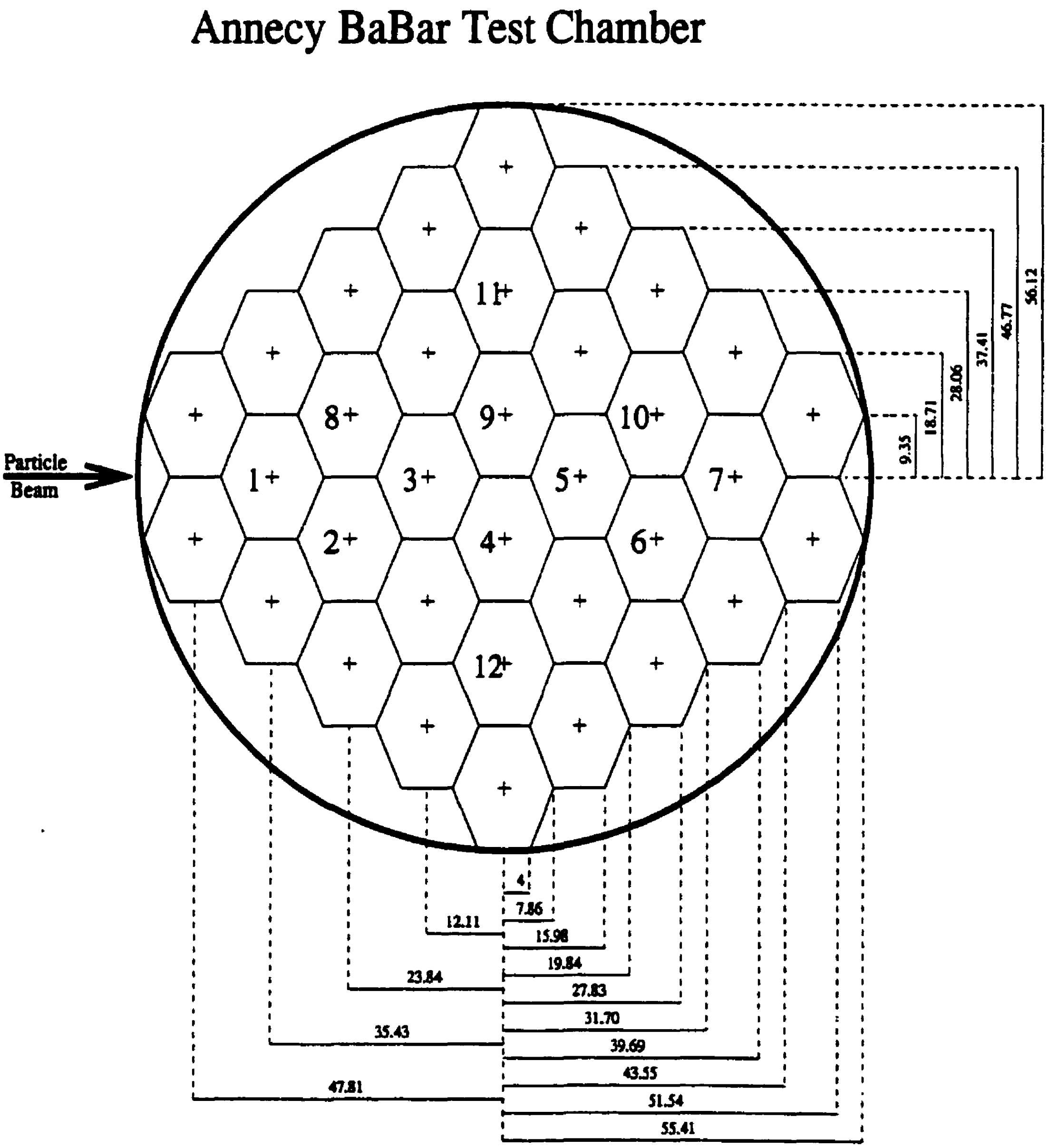

Figure 4.1: 2D geometry of the small scale drift chamber prototype.

For the events passing the common threshold, needed information was obtained in the following way. The times at which the signal arrived at sense wires in cells 1-10 were recorded by TDCs[1] while the charge collected on each sense wire was recorded by ADCs.[2] Signal duration was limited to a $2\mu s$ gate. In addition, cells 1-7 were also recorded by FADCs.[3] Only 200 samples were made at the rate of 100Mhz. Other 24 cells were not read. An Fe^{55} radioactive source is mounted on the inner wall of the chamber. Fe^{55} transforms via the capture of an electron from one of its atomic orbitals: $e^- + p \rightarrow n + \nu$. A hole in the atomic shell is filled by another atomic electron giving rise to the emission of a characteristic x-ray (231keV, with a half-life of 2.73 years [WPF88]). Electrons from this decay cause ionization the same way the beam particles do. Every 5 minutes 500 of these 'source' events are recorded. These were used for calibration purposes. The lifetime of this iron isotope is large enough so that the probability of one beam and one source events overlapping is negligible.

Four scintillators[4] and two ATCs[5] were mounted in front of the chamber and used with beam events. The coincidence of four scintillators was used as a trigger. ATC readouts were used to distinguish whether the ionizing particle was a proton

---

[1] Time-to-Digital Converter: TDC gives a time interval measurement in digital form. Trigger starts a scaler which counts pulses from a constant frequency oscillator. At the arrival of the signal this scaler is gated off to yield a number proportional to the time between trigger and the signal. [Leo87]

[2] Analog-to-Digital Converter: ADC is a device which converts an analog signal to an equivalent digital form. The signal charges a capacitor which is then discharged at a constant current. Digitised signal amplitude is proportional to discharge time. [Leo87]

[3] Flash Analog-to-Digital Converter: FADC is an ADC which samples the signal at a fixed rate thus digitising both the shape and the magnitude of the signal. [Leo87]

[4] Scintillator is a particle detector utilising a property of some materials which emit a flash of light when struck by a particle (charged or neutral).

[5] Aerogel Čerenkov Threshold Counter: ATC produces a signal when its medium istraversed by a particle which emits Čerenkov radiation. This happens if the the particle moves faster than light propagates through the detector medium ($\beta_{particle} > 1/n$).

or a pion. Minimum (threshold) momentum at which a given particle will emit Čerenkov light is:

$$p_{threshold} = \frac{m_0 c}{\sqrt{n^2 - 1}}, \tag{4.1}$$

where m_0 is the particle's rest mass and n is the index of refraction of the ATC medium. For our two ATCs (n=1.03 and n=1.05) threshold momenta for pions and protons are: $p_{thr}(proton, 1.03) = 3.8\mathrm{GeV/c}$, $p_{thr}(proton, 1.05) = 2.9\mathrm{GeV/c}$, $p_{thr}(pion, 1.03) = 0.57\mathrm{GeV/c}$, $p_{thr}(pion, 1.05) = 0.44\mathrm{GeV/c}$. Therefore, a combination of these two ATCs allows us to distinguish pions from protons up to the momentum of $\approx 3.8\mathrm{GeV/c}$. Fig. 4.2 shows the schematics of the experimental setup used for the beam testing at CERN.

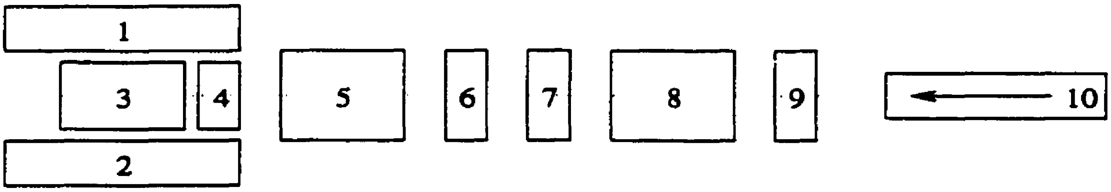

Figure 4.2: Experimental setup in the T10 test area at CERN.

Recording of a beam event starts when a trigger signal is sent to FADC, ADC and TDC. This happens when scintillators S1-S4 are hit, the beam is on and the computer is ready to take new data. Trigger for the source events is provided by the drift chamber signal passing a set threshold and a ready signal from the computer.

The outputs of the chamber (pulses from sense wires) are split, attenuated to 1.5V for the FADC and 400mV for the TDC/ADC and time delayed not to precede the trigger. A Fan out[6] unit is used to split the signals going to TDCs/ADCs.

---

[6] Fan out: FO is an active device which allows distribution of one signal to several parts of the system by 'dividing' the input into several identical signals of the same height and shape. It should be distinguished from the passive splitter which divides signal's amplitude

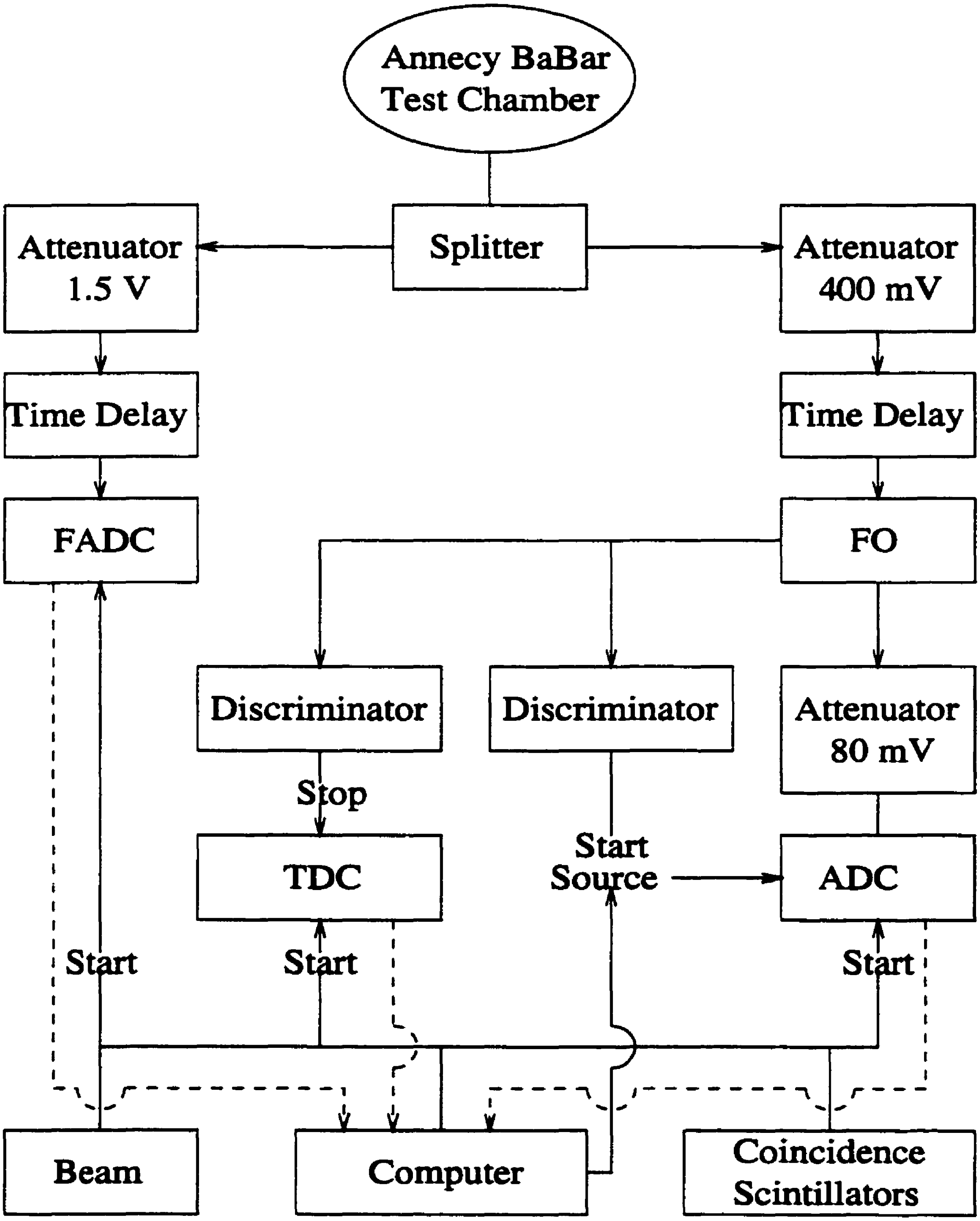

Figure 4.3: Schematics of the Data Acquisition System.

#	Component	Description
1,2	Magnet	B_{max}=1.2T, gap = 22cm
3	Drift Chamber	radius = 5.55cm, length = 17.5cm
4,6,7	Scintillators S4,S3,S2	cross section = 27mm×27mm
5	Aerogel Threshold Counter ATC3	n=1.03, read by an ADC
8	Aerogel Threshold Counter ATC5	n=1.05, read by an ADC
9	Scintillator S1	cross section = 100mm×100mm, read by an ADC
10	Beam Pipe	$\pi^{\pm}, p^{\pm}$ p=1Gev/c → 5Gev/c

Table 4.1: Experimental setup at T10, summary of the component characteristics.

ADC signal is then attenuated to 80mV, and the signal passing the threshold stops the TDC. See Fig. 4.3.

4.2 The Truncated Mean Method

The dE/dx resolution is calculated using a truncation technique. Only a fraction of the hits (dE/dx measurements from each of the cells) are used in the energy loss calculation. The hits are ordered according to the pulse heights, from small to large, and a certain percentage of hits are removed from the high end. The means of the remaining dE/dx measurements are histogramed. This technique should convert a Landau spectrum of dE/dx into a Gaussian-like spectrum of the truncated means [GDKK96]. The resolution is then defined as the ratio of the width of the Gaussian to the pedestal subtracted peak [GDKK96]. Truncation method yields symmetrical errors on dE/dx (this would not be true for errors derived from the original, asymmetric, Landau distribution) which can then be easily propagated.

It will be shown that this method works well for low statistics, but fails for a large number of events, as the truncated distribution systematically differs from a Gaussian. This is easily understood knowing that the relative uncertainty of the counts in each bin equals: $\frac{\sigma_N}{N} = \frac{1}{\sqrt{N}}$. Therefore, a histogram with lower statistics will give a better fit, even if the fit function does not fully correspond to the fitted distribution.

Two sets of random numbers (N=42,000 and N=420,000, which are statistics corresponding to 1000 and 10,000 events with 42 hits per event) were generated according to the Landau distribution peaking at 100 with the width of 10 (arbitrary units). 42 consecutive numbers were linked into an 'event' and truncation mean method was applied. A number of highest hits were cut from each 'event' and the truncated distributions are plotted in Figs. 4.4 (1000 'events') and 4.5 (10,000 'events').

Each of the truncated distributions was fitted to a Gaussian and a confidence level [7] was calculated for the obtained χ^2 and a given number of degrees of freedom.

$$C.L.(\chi^2) = \int_{\chi^2}^{\infty} f(z,n)dz \tag{4.2}$$

When the number of degrees of freedom (n) is large the confidence level is approximated by [BC84]:

$$C.L.(\chi^2) \approx \frac{1}{\sqrt{2\pi}} \int_{y}^{\infty} e^{\frac{-x^2}{2}} dx, \tag{4.3}$$

where $y = \sqrt{2\chi^2} - \sqrt{2n-1}$.

The confidence levels of the Gaussian fits to the small Landau 'data' set are dependent on the number of truncated hits (see Table 4.2). The best fit is obtained

---

[7] C.L. is the probability that a random repeat of a given experiment would lead to a greater χ^2, assuming the model is correct. It is used as a measure of the fit quality.

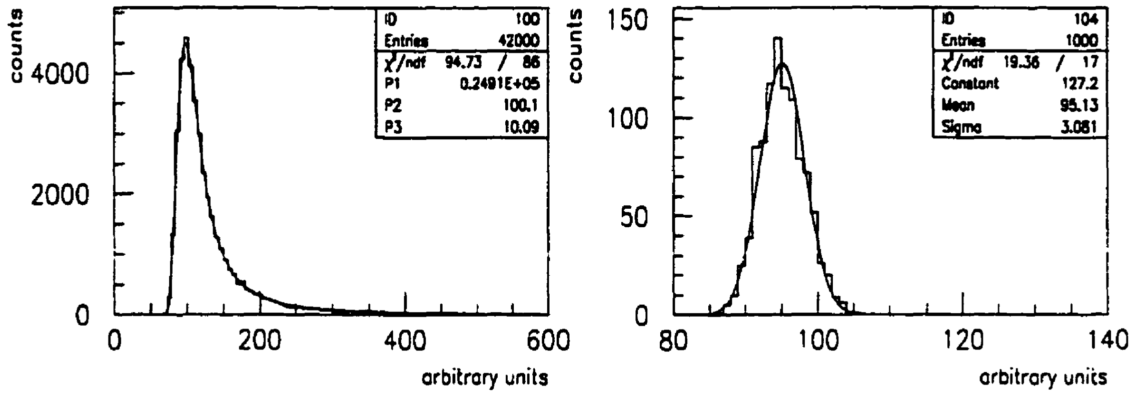

Landau Distribution

Truncated mean, 40%

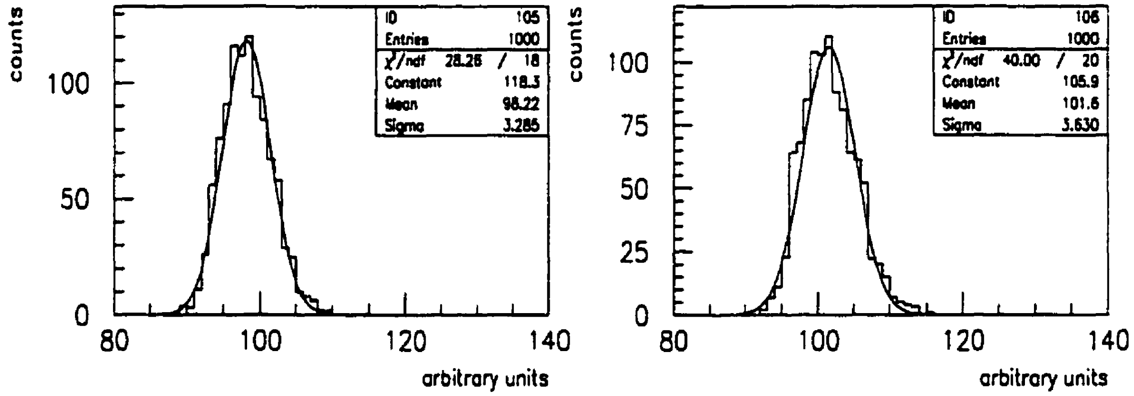

Truncated mean, 50%

Truncated mean, 60%

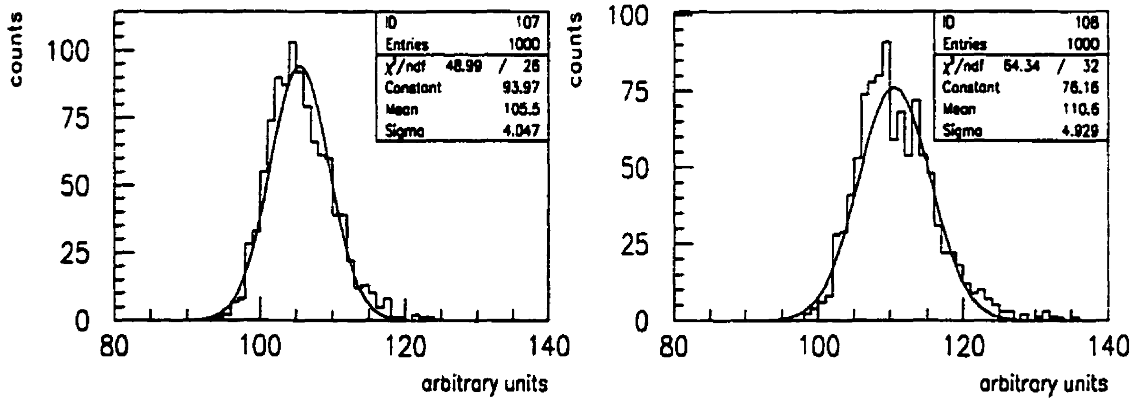

Truncated mean, 70%

Truncated mean, 80%

Figure 4.4: Landau Distribution and the corresponding truncated means for 1000 simulated 'events'. The percentage of hits used in calculation is indicated.

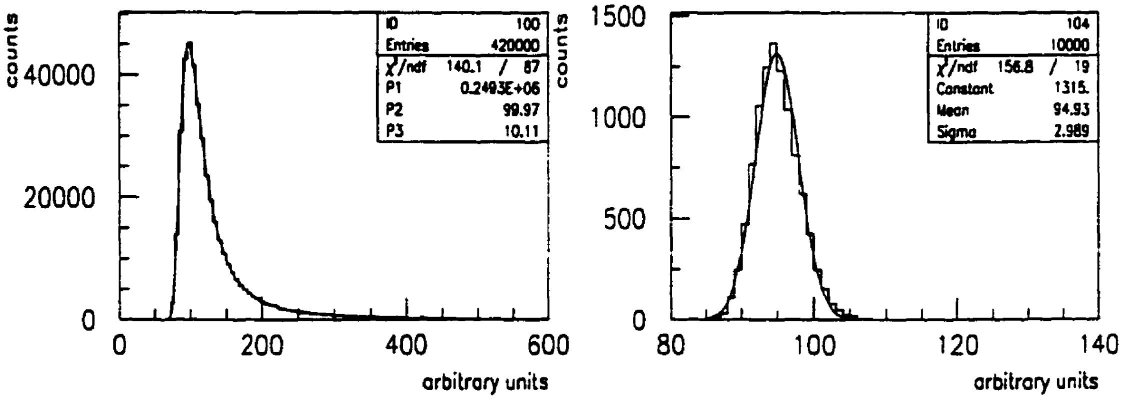

Landau Distribution

Truncated mean, 40%

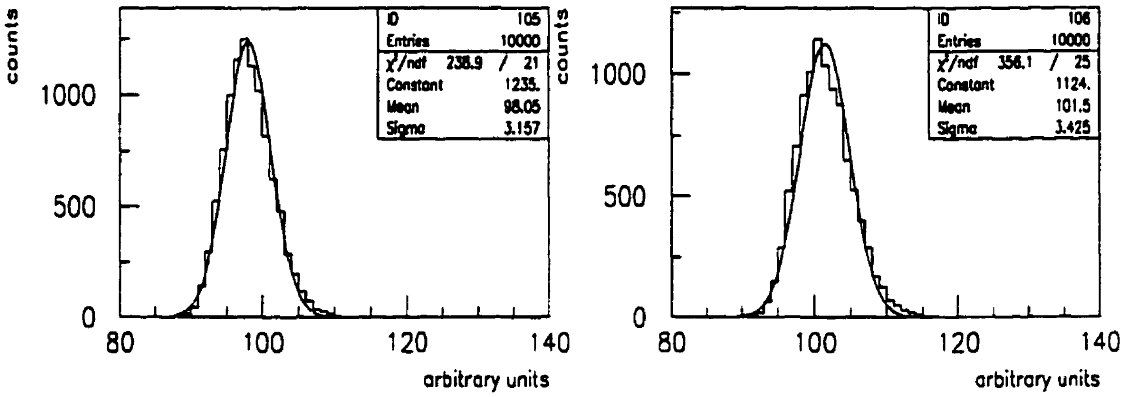

Truncated mean, 50%

Truncated mean, 60%

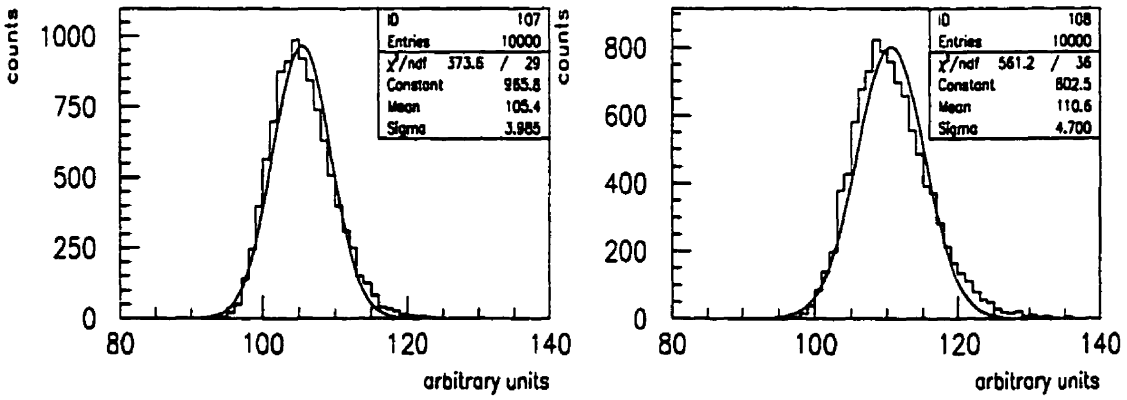

Truncated mean, 70%

Truncated mean, 80%

Figure 4.5: Landau Distribution and the corresponding truncated means for 10,000 simulated 'events'. The percentage of hits used in calculation is indicated.

Fraction of the hits used	40%	50%	60%	70%	80%
Confidence level	31.6%	5.45%	0.35%	0.29%	0.03%

Table 4.2: Confidence level of the Gaussian fit as a function of the percentage of hits used.

when only 40% of the sampled hits are averaged. There is a tradeoff of the quality of the Gaussian fit and the resolution obtained, dependent on the truncation fraction, that will have to be examined when the data is analyzed. It should be noted that the mean of the Gaussian corresponds to the peak position of the underlying Landau distribution. A small shift in the peak is observed and will be corrected for.

When the same truncation method is applied to the big 'data' set (10,000 'events') distribution that is obtained is no longer a Gaussian. Regardless of the truncation fraction confidence levels of the Gaussian fits are identically 0. Truncated distributions systematically differ from a Gaussian. A small asymmetry in the peaks (elongated high end is the consequence of the original Landau distribution) can be neglected and, therefore, we are able to define the resolution of the ionization energy loss as the ratio of the width to the mean of the Gaussian (truncated) distribution.

4.3 GEANT Detector Description and Simulation Tool

GEANT [Sof94] is a system of detector description and simulation tools which help in design, optimization, development and testing of reconstruction programs, and interpretation of experimental data from High Energy Physics experiments.

4.3.1 GEANT Simulation of the Prototype Drift Chamber

GEANT was used to simulate the drift chamber response and see what dE/dx resolution is to be expected. Both the geometry of the chamber and the properties of the Helium-Isobutane gas [8] were taken into account. GEANT uses Monte Carlo techniques to simulate passage of particles through different detector components taking into consideration properties of the simulated particle (its type and momentum), traversed materials and any external factors (such as electric and magnetic fields [9]). For each simulated event we know the exact length the particle traveled in each cell of the drift chamber, as well as the amount of ionization energy deposited in each cell. GEANT assumes that the charge collection at the sense wire is 100% efficient. In simulating ionization energy loss GEANT uses two corrections to Landau model. Vavilov [Vav57] theory removes the restriction that the typical energy loss is small compared to the maximum energy loss in a single collision. If typical energy losses are comparable to the binding energies, as is true for gaseous detectors, more sophisticated approach is necessary [Tal79] to simulate data distributions.

Therefore, dE/dx resolution obtained from GEANT does not include any experimental uncertainties and it is a measure of the intrinsic width of the ionization distribution.

10,000 pions (π^-) and 10,000 protons, at momentum of 3.0GeV, were created and their behavior in the prototype drift chamber was observed. To avoid

---

[8] For the drift chamber gas mixture (80%He, 20%C_4H_{10}) A=5.222g/mol, Z=2.626, $\rho = 8.4 \times 10^{-4}$g/cm^3.

[9] Some runs with an external magnetic field present were taken at CERN. A study discussed in this thesis, however, is based exclusively on $B = 0$ runs.

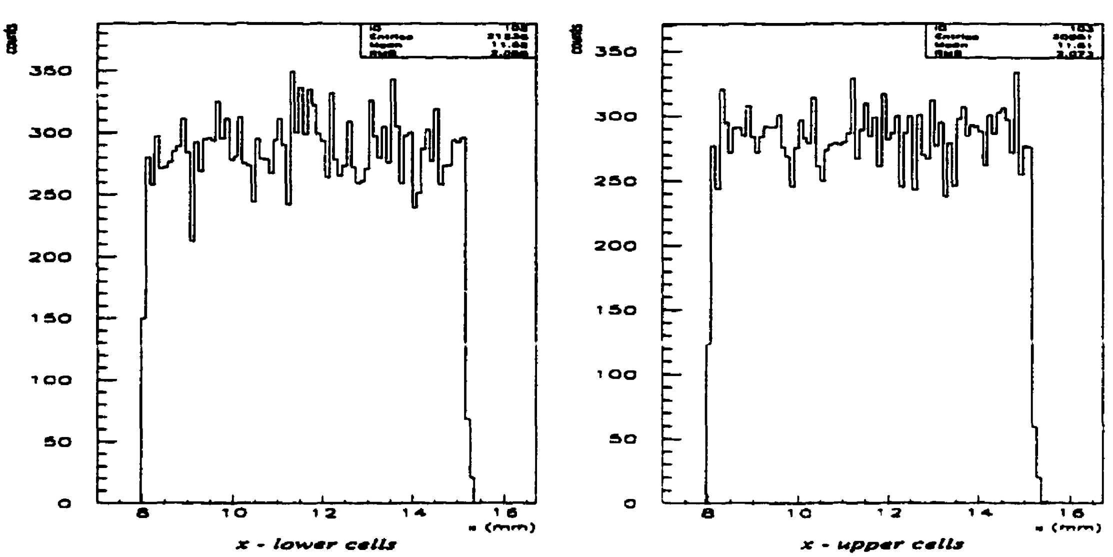

Figure 4.6: Lengths traversed in each cell (mm). Two possible paths are shown. Flat distribution verifies that the cell illumination is uniform.

fluctuations in dE/dx resulting from a short distance traversed in a given cell only the events for which this distance lies in a 8mm-15.72mm range [10] were selected. This cut removed approximately 40% of events, with roughly a half of the remaining events passing through lower 7 cells (marked 1,2,3,4,5,6,7 in Fig. 4.1) and a half passing through upper 7 cells (marked 1,8,3,9,5,10,7 in Fig. 4.1) See Fig. 4.6. These are the only two possible paths because each test-beam particle will be required to have at least 7 hits, and only cells 1-10 are read by the electronics.

Figs. 4.8 and 4.9 show simulated dE/dx (ionization energy deposited in each cell, divided by the length traversed through that cell) for the drift chamber prototype, along with the corresponding truncated distributions. Incident particles are pions and protons at 3GeV/c momentum. Fits to the Landau distribution (in terms of the universal Landau [KS84] function) are also shown. The fit for three independent parameters (P1 - integrated area of the distribution, P2 - the

---

[10] Determined by the chamber geometry, corresponding to particles which do not pass close to field and sense wires.

peak of the distribution, and P3 - the width of the distribution) was done using PAW [Sof95]. The fit function is:

$$\begin{aligned} F(X) &= P1 \times \Phi(\lambda) \\ \Phi(\lambda) &= \int_{-\infty}^{\lambda} \phi(\lambda) d\lambda \\ \phi(\lambda) &= \frac{1}{2\pi i} \int_{c-i\infty}^{c+i\infty} \exp(u \ln u + \lambda u) du, \quad c \geq 0 \\ \lambda &= \frac{X - P2}{P3}, \end{aligned} \tag{4.4}$$

with X being the measured dE/dx. The peak of the distribution, corresponds to the average ionization per unit length of pions (protons) in the He-Isobutane gas (as given by Bethe-Bloch formula, Eq. 2.23), while the width of the dE/dx distribution is given by: $\sigma = \xi/x$, with ξ being the width of the ionization distribution (dE, not dE/dx), as defined in Eq. 2.27. Using the fundamental constants, properties of the incident particles (type and momentum) and the parameters (A, Z and ρ) of the drift chamber gas we can calculate the theoretical prediction of the width of the Landau distribution. Results are shown in Table 4.3. Note that the theoretical positions of the peaks are too high. This is due to the $\delta = 0$ approximation which overestimates the specific ionization. See Fig. 2.5.

4.3.2 Truncation of the GEANT dE/dx Distribution

	μ[keVmm^{-1}]	σ[keVmm^{-1}]	C.L.[%]
Land(p)	9.72×10^{-2}	6.96×10^{-3}	49.6
Theo(p)	14.16×10^{-2}	7.075×10^{-3}	
Land(π)	9.88×10^{-2}	7.68×10^{-3}	2×10^{-21}
Theo(π)	12.23×10^{-2}	6.473×10^{-3}	

Table 4.3: Fit parameters and theoretical values for dE/dx distributions (Landau).

dE/dx distributions of both protons and pions were obtained from GEANT. We see great agreement between theoretical values and the fit parameters in case of protons. Pion distributions, on the other hand, seem to be too wide, fit values are an overestimate of the expected ones. More importantly, it can be seen that the pion distribution is not Landau. This is because another regime defined by the contribution of the collisions with low energy transfer needs to be considered when $\xi/I < 50$ (this is the limit to Landau theory in GEANT). Below this limit, as it is true in our case where $\xi_{proton} = 70.73\text{eV}$, $\xi_{pion} = 64.71\text{eV}$ and $I = 38.51\text{eV}$ special models taking into account the atomic structure of the material are used. The Urbán Model [Sof94] computes restricted energy losses with δ-ray production and can be used for thin layers and gasses. Approaching the limit of of the validity of Landau theory, the energy loss predicted by the Urbán Model approaches smoothly

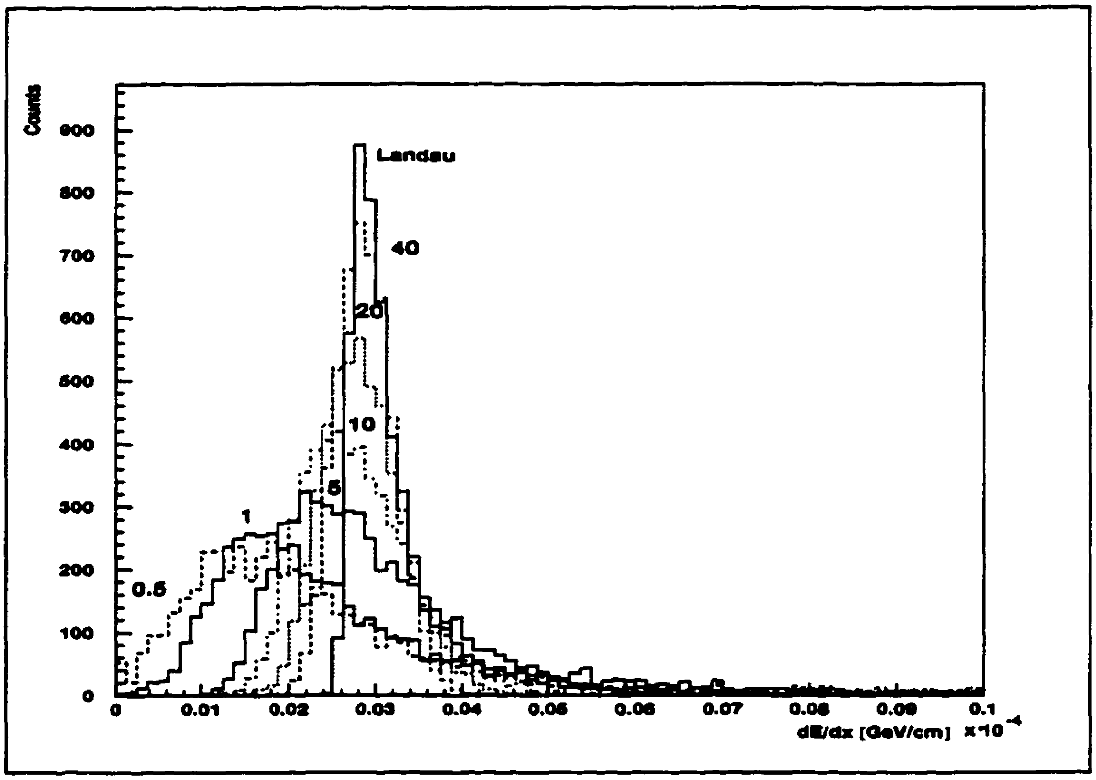

Figure 4.7: Energy loss distribution for a 3 GeV electron in Argon as given by standard GEANT. The width of the layers is given in centimeters. Taken from [Sof94].

the Landau distribution, as seen in Fig. 4.7. It is assumed that the atoms have two energy levels and that particle-atom interaction will be either excitation energy loss or an ionization energy loss. As the excitation cross sections depend on the mass of the incoming particles this correction is visible in the pion spectrum but not in the proton spectrum.

	N[%]	μ[keVmm^{-1}]	σ[keVmm^{-1}]	σ/μ[%]
protons	40	9.37×10^{-2}	2.01×10^{-3}	2.1
	50	9.59×10^{-2}	2.20×10^{-3}	2.3
	60	9.82×10^{-2}	2.42×10^{-3}	2.5
	70	10.1×10^{-2}	2.73×10^{-3}	2.7
	80	10.4×10^{-2}	3.38×10^{-3}	3.2
pions	40	9.50×10^{-2}	2.74×10^{-3}	2.9
	50	9.75×10^{-2}	3.12×10^{-3}	3.2
	60	10.0×10^{-2}	3.39×10^{-3}	3.4
	70	10.3×10^{-2}	3.86×10^{-3}	3.7
	80	10.7×10^{-2}	4.33×10^{-3}	4.1

Table 4.4: Fit parameters of the truncated mean distributions for several truncation fractions (percentages of hits used in the calculation of the means).

Truncation method was applied to dE/dx distributions of both protons and pions. Fits are shown in Figs. 4.8 and 4.9 and the obtained parameters are summerized in Table 4.4. It was shown before that the truncation method does not yield a true Gaussian for high statistics, so high χ^2s per degree of freedom of the fits to the truncated distributions were expected. The widths of these distributions are a measure of the intrinsic width of the original Landau distribution. The actual dE/dx resolution (defined as σ/μ of the truncated means distribution) which will be measured from the data has two contributions: the intrinsic width

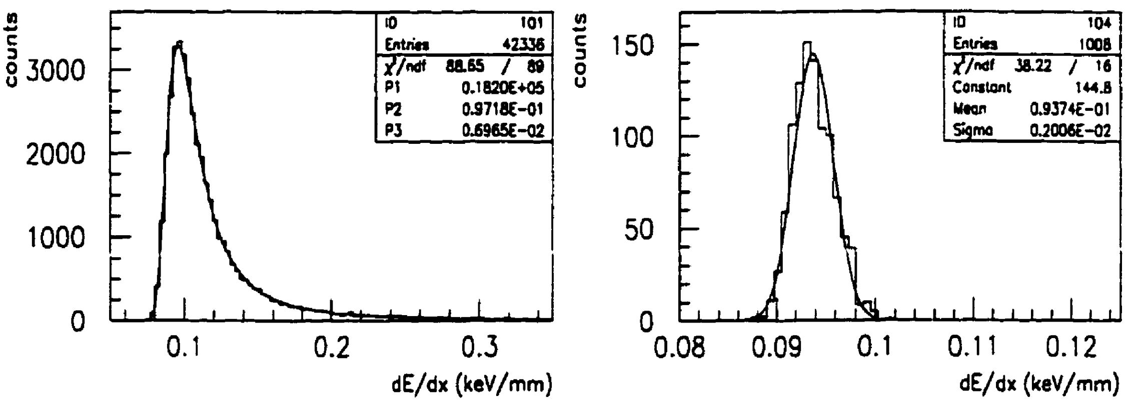

dE/dx (proton) - all cells

Truncated mean, 40%

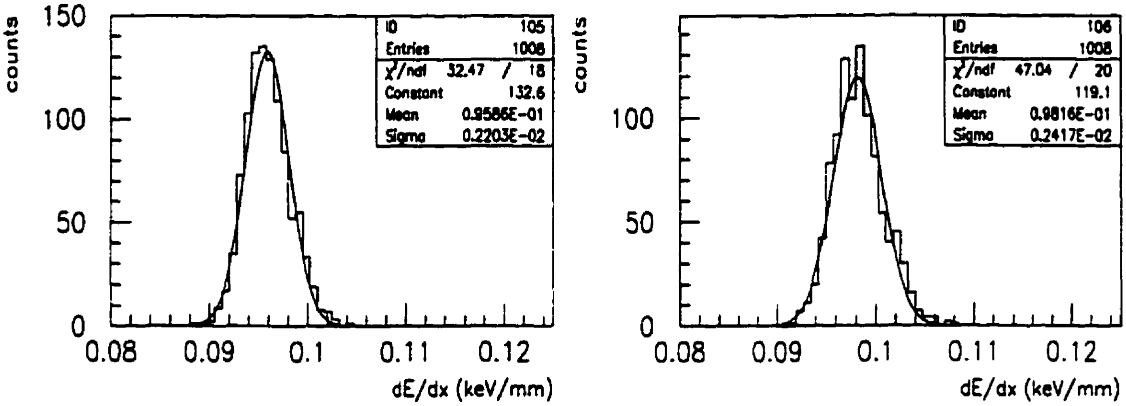

Truncated mean, 50%

Truncated mean, 60%

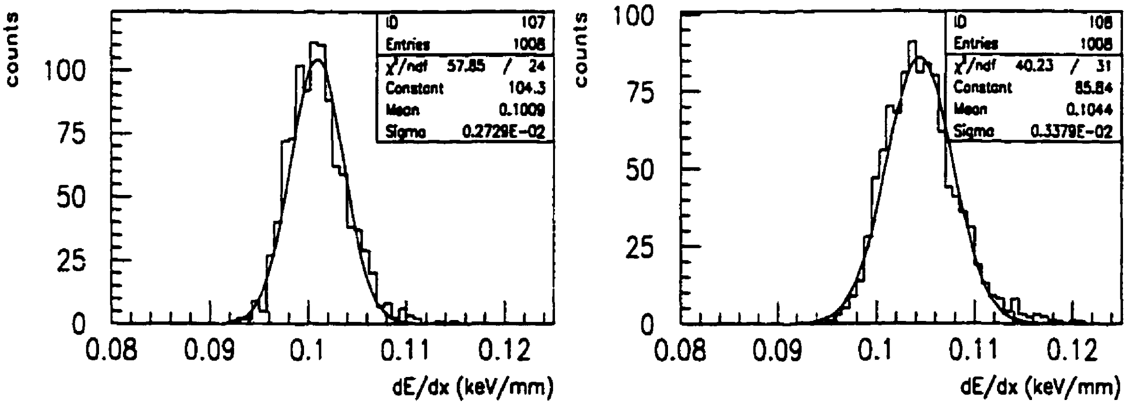

Truncated mean, 70%

Truncated mean, 80%

Figure 4.8: dE/dx **distribution for 3GeV/c incident protons. Truncated means for various truncation fractions are also shown.**

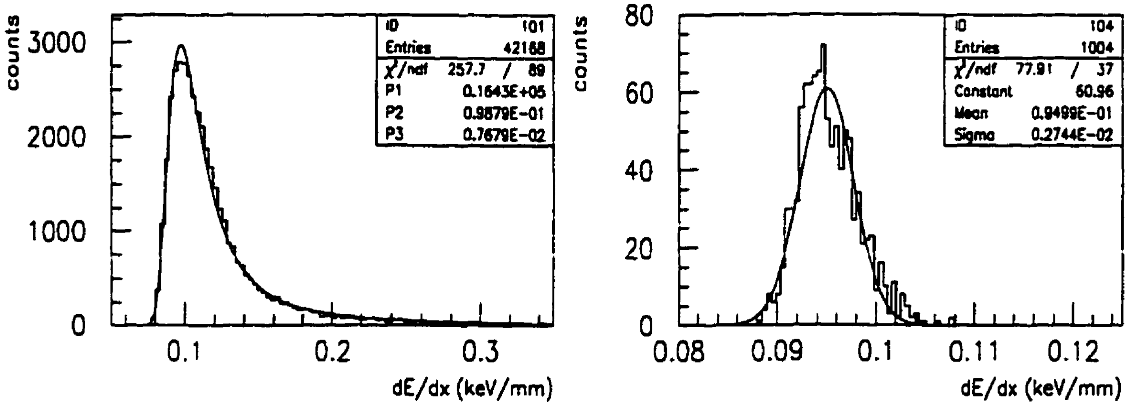

dE/dx (pion) - all cells

Truncated mean, 40%

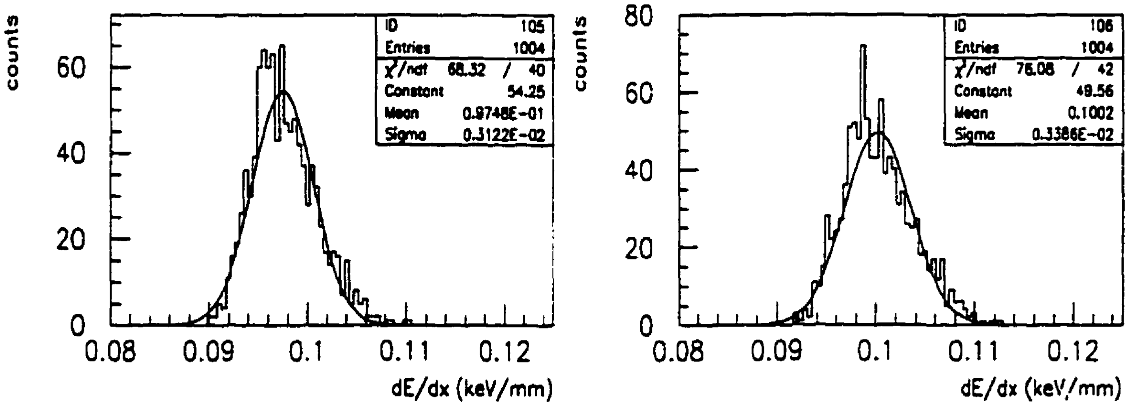

Truncated mean, 50%

Truncated mean, 60%

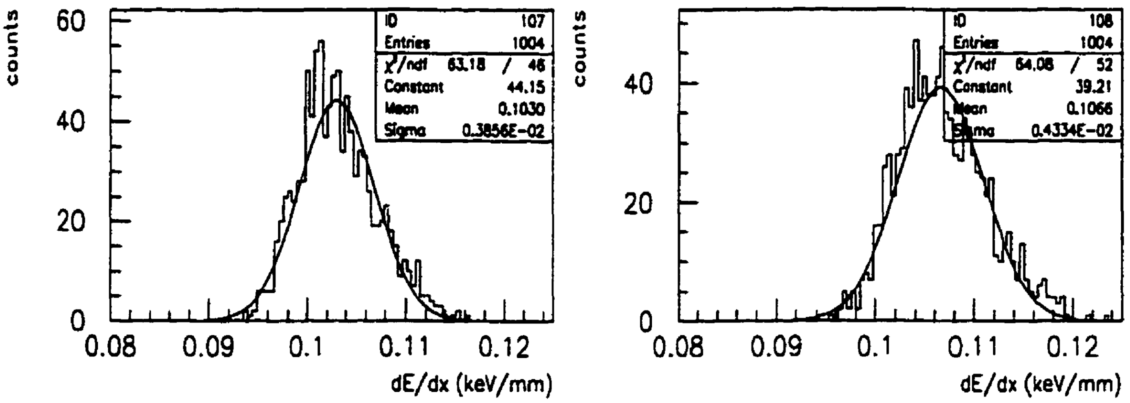

Truncated mean, 70%

Truncated mean, 80%

Figure 4.9: dE/dx **distribution for 3GeV/c incident pions. Truncated means for various truncation fractions are also shown.**

of the dE/dx distribution and the width due to experimental uncertainties.

4.4 The Track Fit

To measure specific ionization (dE/dx) in the drift chamber prototype one needs to know the amount of ionization energy deposited in each cell, as well as the length the particle traveled in a given cell. To obtain the later, the exact trajectory of the particle (the track) needs to be reconstructed. The only information available is the TDC readouts (or the timing as deduced from the FADCs) which correspond to the transport time of the ionization electrons from the track to the sense wire. To convert this time information into distance the time-to-distance relationship (TD is generally a function of the distance to the sense wire) needs to be known. Even the knowledge of the right TD does not uniquely determine the track, as the direction from which the charge has drifted to the sense wire is unknown. This leaves us with a set of circles centered at sense wires with radii representing the drift distance in each cell. See Fig. 4.10. The track is finally determined by minimizing the following χ^2 fit:

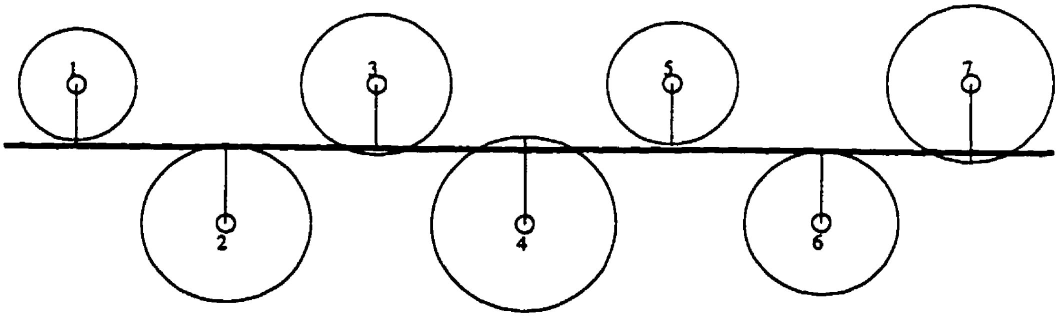

Figure 4.10: A single track passing through cells 1-7. Circles are distances the ionization electrons traveled to the sense wire.

$$\chi^2 = \sum(X_{TD} - X_{FIT}), \tag{4.5}$$

where $X_{TD} - X_{FIT}$ are the space residuals (difference in the distance from the sense wire obtained from the TD and the distance of the track). Due to the experimental error in the drift-time measurement and the uncertainty in the TD function these residuals will be nonzero. The track, which is our best estimate of the actual particle trajectory, is a curve (a helix which in the absence of the magnetic field flattens into a line) passing through points X_{FIT} which minimize the normalized sum of the squared residuals.

4.4.1 GARFIELD Simulation of the Drift Chamber

GARFIELD [Vee96] is a computer program originally written for the detailed simulation of two-dimensional drift chambers. The input parameters include the chamber geometry, voltages on the field wires and the properties of the drift chamber gas. The two-dimensionality is, in our case, not a serious constraint as the beam particles traverse the drift chamber perpendicular to the wires which allows us to treat the chamber as a 2D object. The program can, for instance, calculate the following: field maps and contour plots, plots of electron and ion drift lines, x(t) (time-to-distance) relations, drift time tables and arrival time distributions. Our main goals were to check the uniformity of the cells by looking at equipotential contours and the drift lines, and to obtain a first order TD function. In Fig. 4.11 we see the layout of the cell with the field wires represented by crosses and sense wires by circles. Note the 90^0 rotation with respect to Figs. 4.1 and 4.10 which makes the beam direction vertical. Drift line plot (describing the trajectories of the ionization electrons drifting toward the sense wires) is shown for the incident particle passing through cells 1-7. The asymmetry in the drift lines is caused by slightly different electric potentials in different cells. This is understandable bearing in mind that the potential at each point in the drift chamber is a superposition of potentials due to each of the sense wires (each sense wire is kept at the constant 1650 Volts).

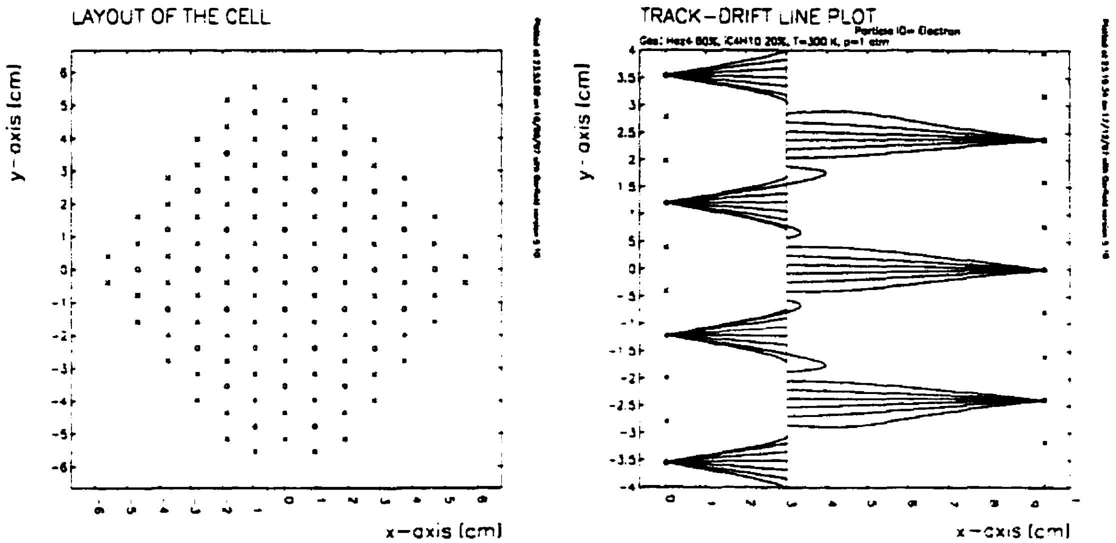

Figure 4.11: Chamber layout (left) and electron drift-lines for particle traversing cells 1-7 (right).

The configuration of surrounding wires changes as we move toward the edges of the chamber, and so does the electric potential, thus changing the drift pattern. This does not pose a serious concern to us, as the timing information is obtained by the first ionization electrons reaching the sense wire. These drift along the line of closest approach of the track to the sense wire and are, therefore, not affected by the asymmetries which are limited to the edges of the cells.

Equipotential contours for the whole chamber, and for cell 4 only, are also shown. We can see that the cell has a nice circular symmetry close to the sense wire. This symmetry is broken as we move toward the edges of the hexagonal cell. It will be shown that the potential configuration close to the edges of the cells prevents the ionization electrons created in that region from reaching the sense wire in a reasonable time.

The most important information obtained from the Garfield program is the first order approximation of the time-to-distance function. TD function can, in principle, be different for different drift chamber cells (only the cells with readouts,

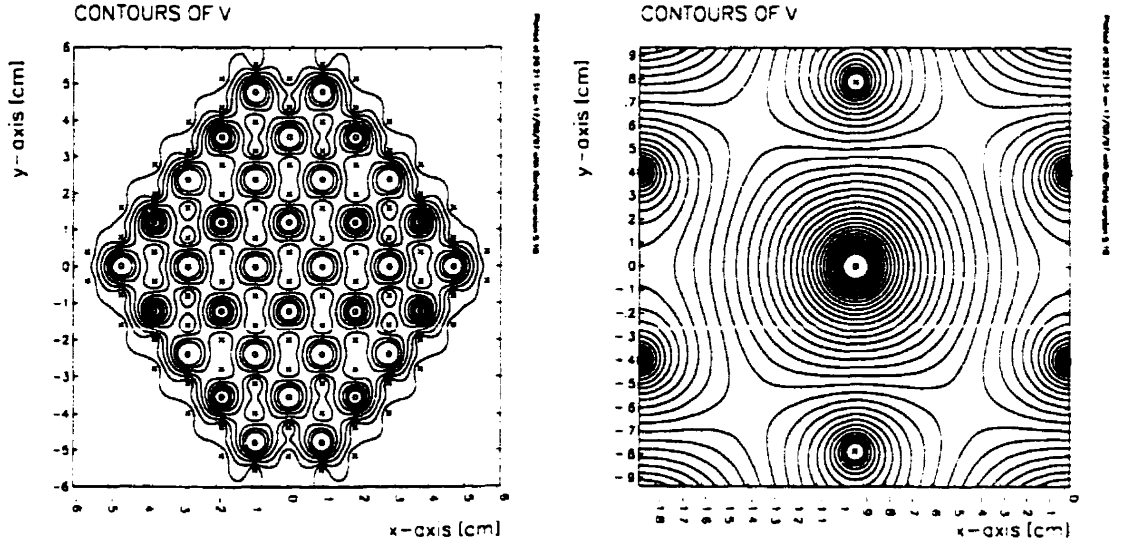

Figure 4.12: Equipotential contours for the whole chamber (left) and cell 4 only (right).

numbered 1-10 in Fig. 4.1 are relevant). Due to the symmetry of the chamber, only TD functions for cells 1-4 were examined. Particles moving along the beam direction (along the positive z axis) were created and the arrival times of the ionization electrons to the sense wires in all of the hit cells were calculated by GARFIELD. By varying the distance of closest approach of the track to the sense wires [11] and calculating the arrival time for each distance a TD function is obtained. Plots of the TD functions for cells 1-4 are shown in Fig. 4.13. Dashed lines represent the estimated uncertainties in the drift times. For the distances larger than ≈ 7.6mm (depending on the cell) GARFIELD calculation of the TD function did not converge properly. In these regions TD function was not plotted, but the values were still calculated and will be used later.

---

[11] Note that due to the specific beam direction the distances of closest approach of the track to sense wires 1, 3, 5 and 7 should be about the same. The same is true for the distances to wires 2, 4 and 6.

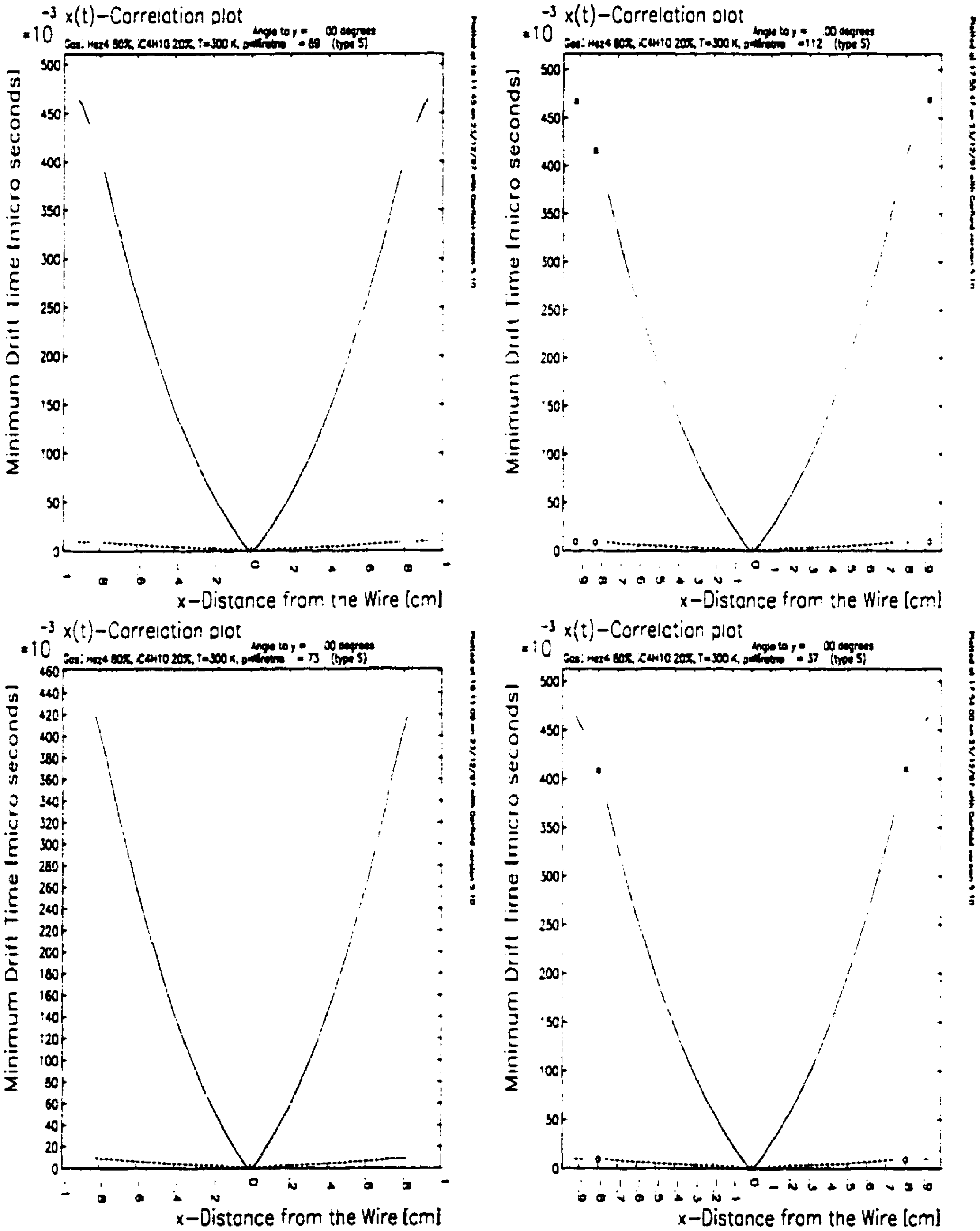

Figure 4.13: Time-to-Distance (TD) function for cell 1 (top left), cell 2 (top right), cell 3 (bottom left) and cell 4 (bottom right).

4.4.2 Time-to-Distance Function and Track Fitting

The time-to-distance function was extracted from the data [12] in the following way:

- An analytical function giving a good approximation to the expected TD function, as calculated by GARFIELD, was found.
- For each event in a given data set drift distances in every cell were calculated from drift times using a current estimate of the drift function.
- A linear fit to the points of closest approach to sense wires (assuming that the first charge arriving to the wire was propagating perpendicular to the track) was made.
- Space residuals, the difference between the distance to the wire calculated from the drift function and the distance of the track to the wire: $RES = X_{TD} - X_{FIT}$, were calculated for each cell that was hit.
- A new estimate of the drift function was obtained by minimizing the sum [13] of the squares of the residuals. This minimization was done using MINUIT [Jam94] function minimization and error analysis tool.
- A proper convergence of this procedure gave us the best approximation of the drift function for our drift chamber.

The choice of the most suitable analytical function to parametrize the time-to-distance function was not simple. The BaBar reconstruction software team

---

[12] For each event we recorded the timing information for each cell (the time the signal propagated to the sense wire) and the charge deposited in each cell (which is not relevant for track fitting).

[13] The sum was performed over all cells and all events in the data set.

suggested the use of a piecewise linear function [14]. This did not work too well due to a fairly large number of parameters (one parameter is needed for each time bin because, if continuity of the TD function is imposed, the offsets are not independent of the slopes). This made MINUIT minimization long and somewhat unreliable because for a large number of parameters (between 7 and 15 time bins were used) and a very big number of points that were fitted (7 cells in $\approx$ 10,000 events per data set) the minimization can converge at a local, as opposed to the global, minimum. Also, a big dependence of the calculated minimum on the input parameters was observed.

The next logical choice for the parametrization of the drift function was a polynomial. To satisfy the basic property of the drift function that zero drift time corresponds to zero distance, the free parameter of this polynomial must equal zero. Another issue was the optimum degree of the polynomial. Clearly, the degree should be as small as possible, resulting in the smallest number of parameters needed to describe the drift function, which is crucial for a good MINUIT minimization. Also, as discussed before, the drift functions are not exactly the same in all of the cells but, as the differences are rather small, one would still like to use a unique drift function. Finally, the choice was the smallest degree for which the parameters of the drift functions for cells 1-4 agreed to within 1 standard deviation. This, in a way, justifies the use of a single drift function for all the cells. The degree chosen was 3, and the parametrization of the time-to-distance function is:

$$X_{TD}(t) = P1 \times t + P2 \times t^2 + P3 \times t^3. \qquad (4.6)$$

Fig. 4.14 shows fits to the GARFIELD predictions of TD functions for cells 1-4.

---

[14] The time axis is divided into a number of bins. TD function in each bin is linear, but the slopes and offsets are different in different bins. The constraint is the continuity on bin boundaries.

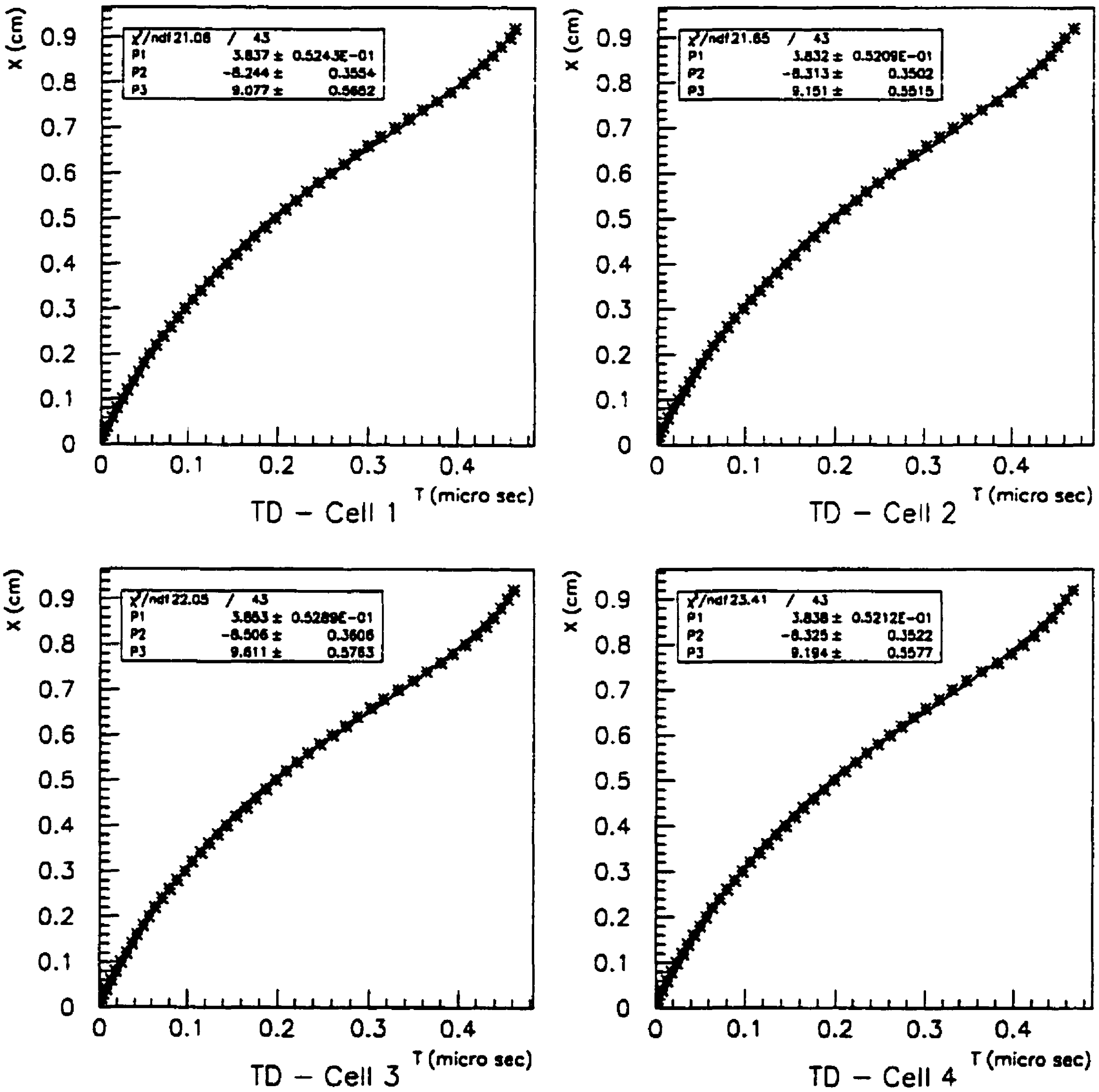

Figure 4.14: Polynomial fits to time-to-distance functions for cells 1-4.

Points (*) are the drift times calculated for the distances of closest approach of the track to the sense wire ranging from 0cm to .92cm, with a step of 0.02cm. Lines are fits to the polynomial function of Eq. 4.6. Fit parameters (P1, P2 and P3), as well as the corresponding χ^2 are shown. They are also summarized in Table 4.5. The mean values of the parameters and their uncertainties were calculated as the weighted average over the cells (due to the symmetry, TD function is the same in cells 1 & 7, 2 & 6, 3 & 5, with cell 4 being unique):

$$\bar{P} = \frac{2P_{Cell1} + 2P_{Cell2} + 2P_{Cell3} + P_{Cell4}}{7}$$
$$\sigma^2(\bar{P}) = \frac{4\sigma^2(P_{Cell1}) + 4\sigma^2(P_{Cell2}) + 4\sigma^2(P_{Cell3}) + \sigma^2(P_{Cell4})}{49} \tag{4.7}$$

It is clear that the proposed parametrization of the drift function satisfies all the requirements mentioned before. The number of free parameters is small, fits to the expected time-to-distance functions are good (all the confidence levels are above 99%, and the parameters for TD functions in different cells are within one standard deviation of each other which allows us to treat the TD function as independent of the cell number.

Cell #	P1	P2	P3	C.L.%
1	3.837 ± 0.052	-8.244 ± 0.355	9.077 ± 0.565	99.68
2	3.832 ± 0.052	-8.313 ± 0.350	9.151 ± 0.552	99.58
3	3.853 ± 0.053	-8.506 ± 0.361	9.611 ± 0.576	99.50
4	3.838 ± 0.052	-8.325 ± 0.352	9.194 ± 0.558	99.12
Mean	3.840 ± 0.027	-8.349 ± 0.183	9.266 ± 0.290	-

Table 4.5: Summary of the parameters for polynomial fits to TD functions in cells 1-4. Confidence levels are also shown.

The focusing magnets in the T10 test area allowed us to set the signed momentum (the product of the magnitude of the momentum and the electric charge of a given particle) of the incoming particles. The test beam runs that will be studied are divided into two classes: runs with the particle momentum of +3GeV/c (240,000 events before cuts, incoming particles are positively charged) and runs with the particle momentum of -3GeV/c (204,880 events before cuts, incoming particles are negatively charged). The main difference is that for the runs with a positive signed momentum the beam contains mostly pions, protons and some kaons, whereas the negative signed momentum beam does not contain antiprotons. This difference can be seen by looking at the ATC response [15] for the two sets of runs. ATC responses are shown in Fig. 4.15. Two different types of particles triggering [16] the ATC can, statistically, be distinguished by the number of Čerenkov photons produced. The number of photons produced by a particle with charge ze per unit path length and per unit energy interval of the emitted photons is [WN96]:

$$\frac{d^2N}{dEdx} = \frac{\alpha z^2}{\hbar c}\sin^2\theta_c = \frac{\alpha^2 z^2}{r_e m_e c^2}\left(1 - \frac{1}{\beta^2 n^2(E)}\right), \qquad (4.8)$$

where $\theta_c = \arccos(1/n\beta) \approx \sqrt{2(1 - 1/n\beta)}$ is the half angle of the Čerenkov cone for a particle with velocity $v = \beta c$. For practical use, Eq. 4.8 must be integrated over the region for which $\beta n(E) > 1$. From the information in Table 4.6 we see that both protons and pions at 3GeV/c will produce Čerenkov light in the ATC3, but only pions will trigger the ATC5. Electrons and kaons trigger both ATCs. Also, we see that pions traversing the ATC counters will produce more photons as they yield larger Čerenkov angle. This is true under the assumption that the energy ranges over which Eq. 4.8 has to be integrated are similar for both types of particles (or if the integration range for pions is larger). Given the actual βs, the integration range for pions is: $n(E) > 1.002$, and the integration range for

---

[15] Remember that our setup of two ATC counters (n=1.05 and n=1.03) allows us to distinguish protons from pions at 3GeV/c momentum.

[16] Passing through the detector with a momentum larger than the threshold momentum, as defined by Eq. 4.1.

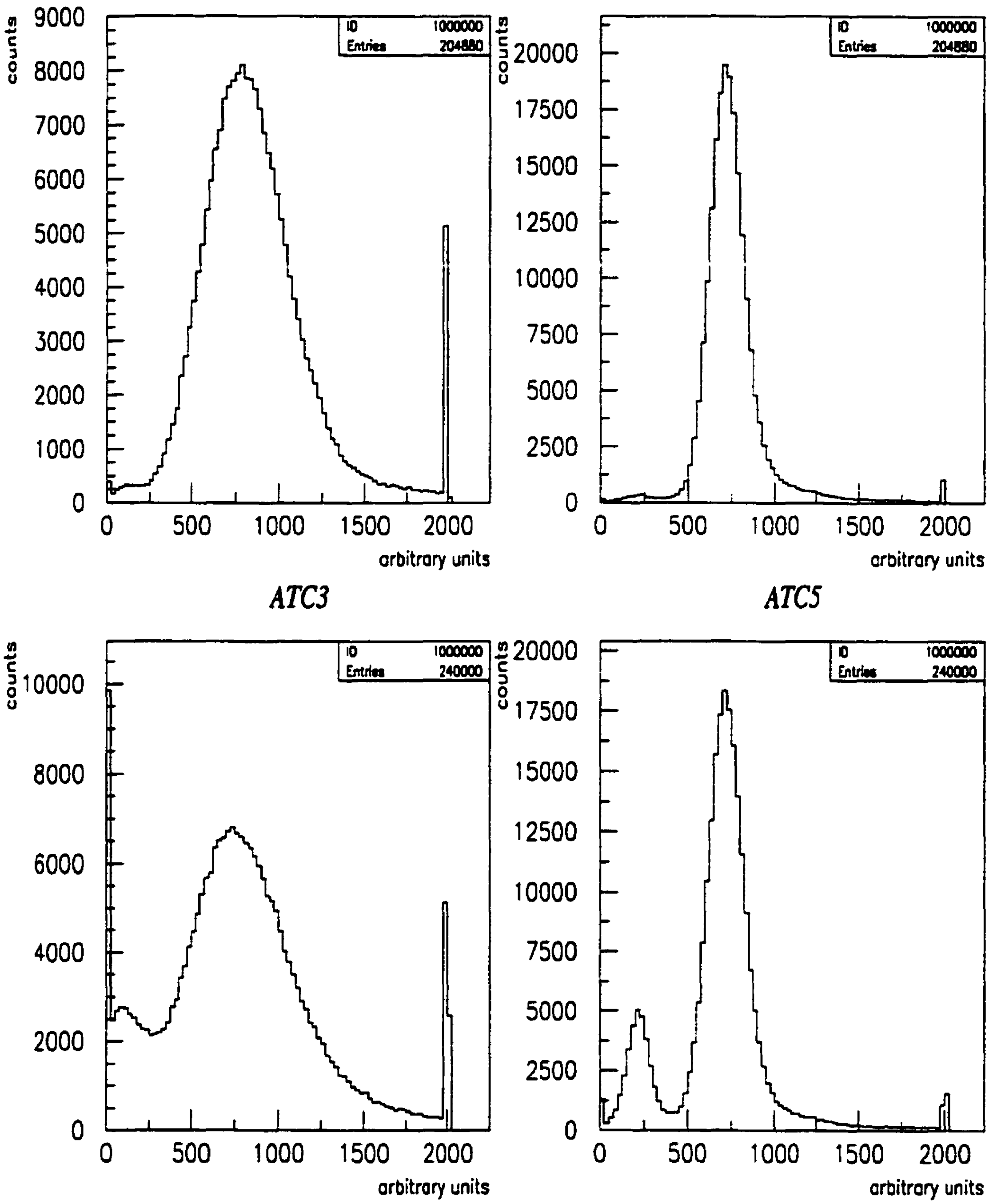

ATC3 ATC5

ATC3 ATC5

Figure 4.15: ATC readouts for the two sets of runs. The -3GeV/c runs (top) show a 'cleaner' beam particle content than the +3GeV/c runs (bottom). Responses from both ATCs are shown: n=1.03 (left) and n=1.05 (right).

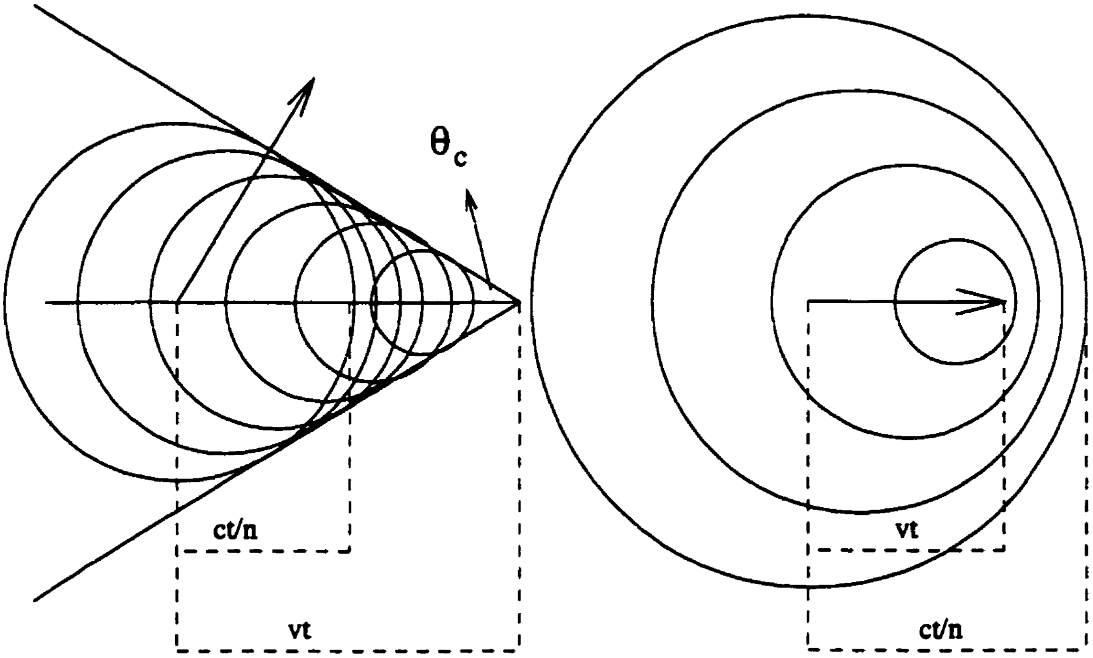

Figure 4.16: Two dimensional projection of the Čerenkov cone (left). For $\beta < 1/n$ there is no constructive interference and Čerenkov light is not emmited (right).

protons is: $n(E) > 1.048$, which verifies the conclusion that pions will produce more Čerenkov light. Looking at Fig. 4.15(bottom), we see a single peak produced by pions (as only pions are over the threshold momentum) in ATC3 and two peaks (lower-protons, higher-pions) in ATC5. The positions of peaks along the x axis are a relative measure of the number of Čerenkov photons produced (assuming that the detection probability is the same for the light produced by either type of incoming particles). The relative positions of pion and proton peaks in ATC5 show that pions produce approximately 3 times more light than protons. This is in agreement with Eq. 4.8 with a factor of two comming from the ratio of $\sin^2\theta_c$s and the rest being due to the larger integration range for pions. The top two graphs have only a single, pion peak. This is the verification of the fact that the beam with the negative signed momentum does not contain antiprotons.

Particle	β	$p_{thr,1.03}$(GeV/c)	$\sin^2\theta_{c,1.03}$	$p_{thr,1.05}$(GeV/c)	$\sin^2\theta_{c,1.05}$
pion	0.9978	0.57	0.053	0.44	0.088
proton	0.9544	3.8	-	2.9	0.042
kaon	0.9736	2.00	0.006	1.54	0.043
electron	0.9999	0.0021	0.057	0.0016	0.092

Table 4.6: Threshold momenta and the Čerenkov angles for protons and pions in both ATCs.

Time Zero (T0)

The raw times measured are not equal to the ionization electron propagation times (drift time) needed for the track reconstruction. TDC readout corresponds to the time between the arrival of the trigger signal which starts the TDC recording (common start) and the signal pulse from a given wire which stops a specific TDC channel. This is different from the drift time due to the time delay of the signal pulses (see Fig. 4.3), the propagation times of the signal pulses from the chamber preamplifier to the discriminator and the various time delays due to the electronics. For the track fitting purposes it is necessary to determine the time zero (T0) which is a difference between raw times and drift times. Time zeros can be different for different channels (corresponding to different sense wires) and will be determined for each drift chamber cell separately. Figure 4.17 shows the recorded time spectra for the sense wires in cells 1-4. The highly populated bin at ≈ 1200ns is the TDC overflow, which is recorded when the stop signal does not arrive within a time gate set for one event. This means that the cell was not hit in a given event. The shape of the spectrum depends on the cell illumination and on the drift function. As the drift velocity is not constant over the cell, uniform cell illumination does not result in a flat drift-time distribution. Since the ionization

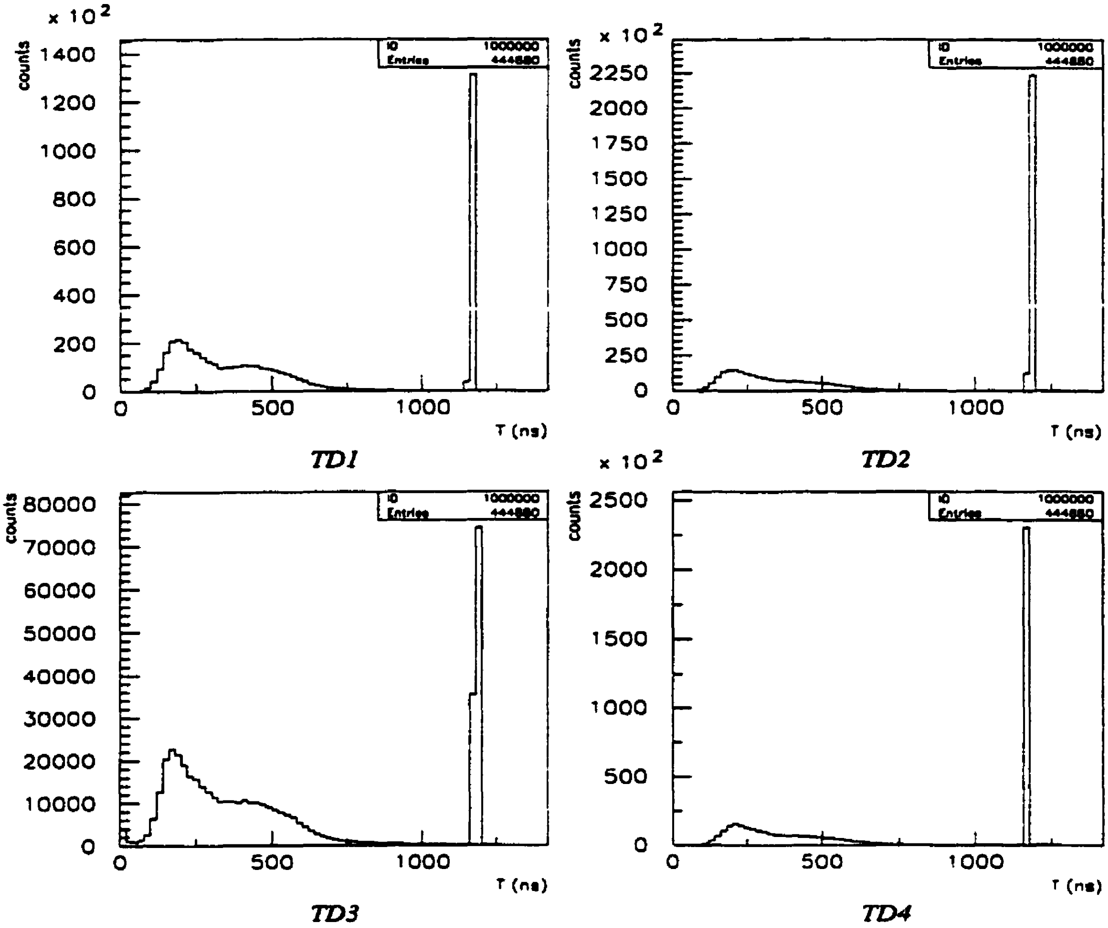

Figure 4.17: Raw time spectra (TDC readouts) for cells 1-4. Both sets of runs (-3GeV/c and +3GeV/c) were used.

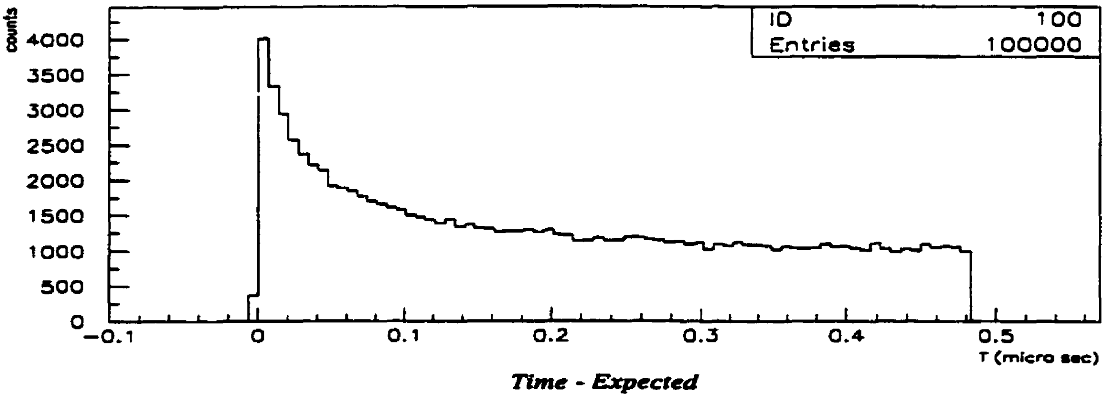

Figure 4.18: The expected time spectrum, uniform cell illumination assumed.

electrons drift faster if the ionization occurred close to the sense wire, the drift-time spectrum will be systematically shifted toward short drift-times, as seen in the Fig. 4.18. This plot was made by first numerically inverting the time-to-distance function into the appropriate distance-to-time function. 100,000 random numbers, with a flat distribution, their values lying between 0 and 0.935, were created thus simulating uniform illumination of a half of a single drift cell. These 'distances' were then converted into the corresponding 'drift times' which, when plotted, represent the expected drift-time distribution. Note that the maximum drift time is ≈ 475ns.

In principle, no signal should arrive before the time T0 has passed. This is not true in a real experiment as a signal larger than the threshold, which will stop the TDC, can be caused by electronic noise. Note that TDC1 overflows less than TDC3 (due to the chamber design and the alignment with respect to the beam, the number of hits should be about the same in cells 1 and 3) which is a consequence of a higher noise level on TDC3, most likely caused by the preamplifiers. Electronic noise is almost exclusively responsible for the drift time mismeasurement which, along with the nonuniformities in the ionization charge collection efficiency as a function of drift distance, converts the theoretical time spectrum of Fig. 4.18 in to the measured TDC response of Fig. 4.17. The sharp leading edge of the distribution becomes a smooth, exponential-like increase. It is clear that the T0 for a given cell must lie between the lowest measured time and the first peak (at about 250ns). The time zero is estimated as the point where the distribution crosses the half maximum mark (in the middle of the peak and baseline values). Individual T0s are found by fitting the leading edge to the following exponential function:

$$F(t) = P4 + P1 \times \left(1 - \frac{1}{e^{\frac{t-P2}{P3}} + 1}\right), \tag{4.9}$$

with $P2$ being the time zero. When $t = P2$ the above function reaches a height exactly between the baseline ($P4$) and the maximum ($P1$), $P3$ is the width over which the function rises.. The full data set (both sets of runs) was used

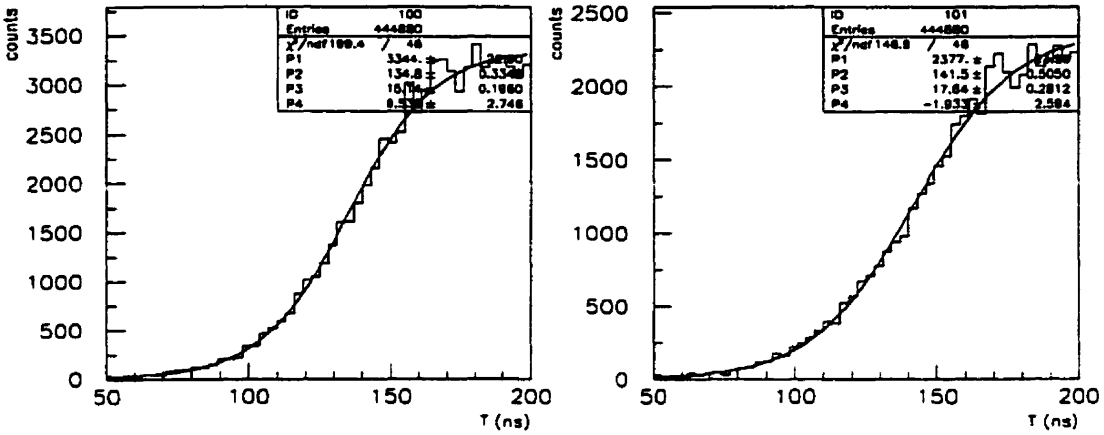

T0 - Cell 1 *T0 - Cell 2*

Figure 4.19: Exponential fits to 'time zeros' for cells 1 and 2. Both sets of runs with were used.

$T0_1$	$T0_2$	$T0_3$	$T0_4$	$T0_5$	$T0_6$	$T0_7$	$T0_8$	$T0_9$	$T0_{10}$
134.8	137.5	125.7	150.6	144.9	125.9	135.1	137.0	128.0	105.8

Table 4.7: Time zeros for all 10 cells, as obtained from the exponential fit (both sets of runs were used). The correction centering the spatial residuals was also applied.

in the T0 determination. This makes sense considering that time zeros depend only on the electronics and transmission delays and they are clearly a property of the experimental setup, independent of the type or the charge of the particle traversing the chamber. The only correction to the fitted values was done in order to center the spatial residuals in every cell around zero, as will be shown later. When determining the correction only the negative signed momentum runs were used as it is impractical to try fitting the whole data set (because of a larger number of events the minimization is not as successful) to adjust all the residuals. The results are presented in Table 4.7

4.4.3 Cuts and Event Selection

Before attempting any event reconstruction (track fitting) and further analysis of the specific ionization, events satisfying certain criteria need to be selected. This is done in order to reduce the experimental background and thus obtain a measurement with the lowest possible uncertainty.

The first requirement imposed on 'good' events is that the appropriate 7 cells (remember that there are two possible paths a particle can traverse, each passing through 7 cells) must be hit. A signal must be recorded in each of the 7 TDCs during a set interval (maximum drift time is $\approx$ 476ns, as seen before) starting at time zero. Additional requirement is that none of the remaining 3 cells were hit. These two cuts combined remove about 25% of the events.

Since the particle type determines the amount of deposited ionization at a fixed particle momentum, it is crucial to exclude all but one particle type, in our case pions. This is done by cutting on the ATC responses. A reasonable cut removes protons from the data sample. The ATC response of the p=-3GeV/c runs (see Fig. 4.15) was fitted to a Gaussian and the events within $\mu^{+3.0\sigma}_{-1.5\sigma}$ are accepted. The cuts, in terms of arbitrary units of light yield, are: $453 < ATC3 < 1488$ and $579 < ATC5 < 998$. The lower limit is severe in order to cut protons from the +3GeV/c runs as well as to ensure that the accepted events have the ATC signal well above the pedestal values. The analysis of the pedestal run is given in Appendix A.

Another requirement is that the ADC content of the 'hit' cells must be larger than a calculated threshold value. This cut will discriminate against the events in which one or more TDCs were triggered by noise. The mean ADC response resulting from the electronic noise was extracted from the pedestal run (Appendix A). Gaussian fits provide both the mean and the width of the pedestal ADC distributions. A 'good' event is required to have all 7 ADC values larger than $\mu + 5.0\sigma$ of the pedestal value.

Finally, the cut which is essential to good tracking involves times measured in all hit cells. From the cell geometry and the known particle direction it is clear that there should be a strong correlation between times measured in cells 1, 3, 5, 7 and in cells 2, 4, 6, or cells 8, 9, 10, as the track passing along the beam direction should be approximately equally distant from each cell in a given group. Similarly, there should be a strong anticorrelation between the times in different groups of cells (remember that either cells 2, 4, 6 or cells 8, 9, 10 are hit in a given event). Figure 4.20 shows time correlations and anticorrelations for a single 20,000 event run. Cutting on the time anticorrelation rather than the time correlation between different cells was proven to be more efficient. Once a scatter plot of anticorrelated times was made (as in Fig. 4.20) only events falling into a region of the plot bounded by two circles (with centers at the 45^0 line) were accepted. This cut also improves the correlation of the times measured in the cells of the same group. The improvement of the tracking resolution achieved by this cut is demonstrated in Appendix B.

Table 4.8 shows the efficiencies of the cuts used. In each of the following table rows (3 Cells Not Hit, ATC Cut, ADC Cut and TDC Cut) only one cut was applied but 7 good hits were always required. The column marked %' gives the efficiency calculated using the number of events with 7 good hits rather than all of the events recorded. The final efficiency (4.5% for negative signed momentum runs and 3.2% for positive signed momentum runs) is low. This is a consequence

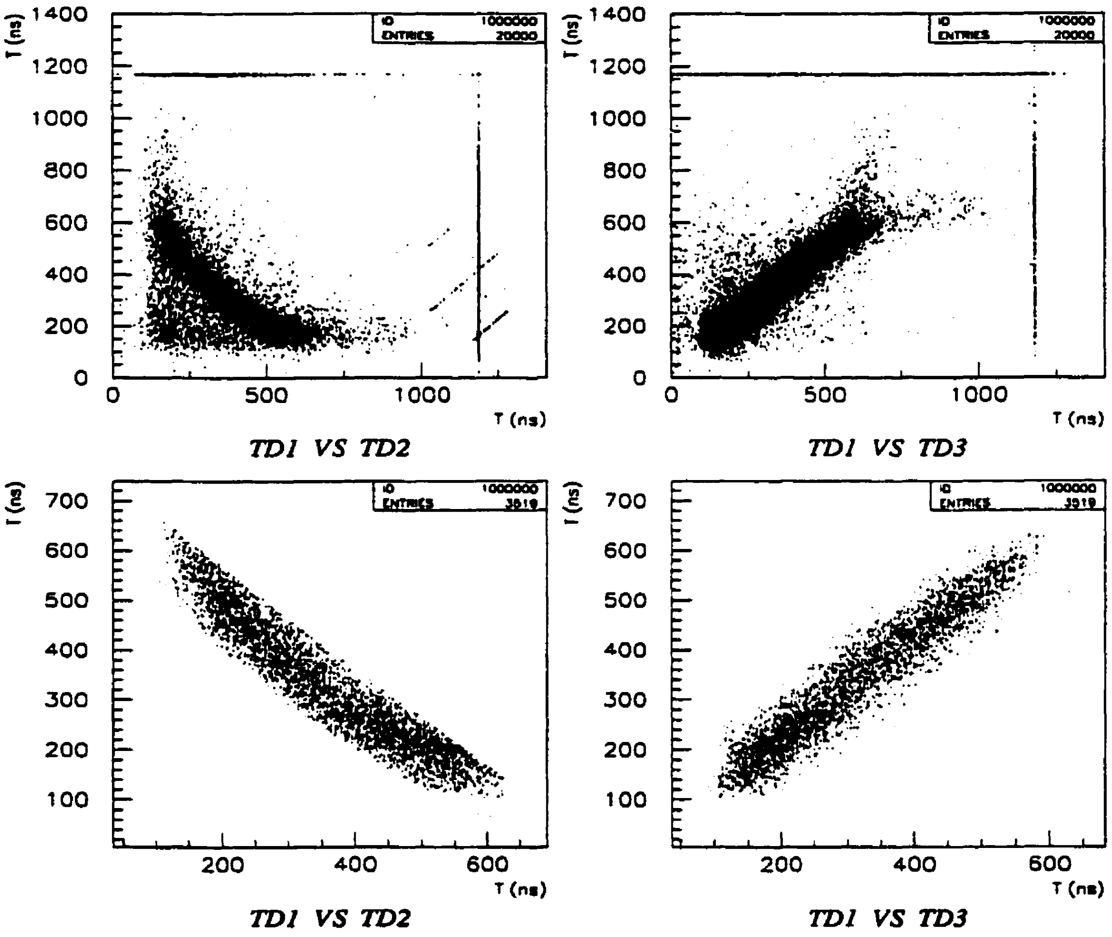

Figure 4.20: Anticorrelation of times in cells 1 and 2 (left) and correlations of times in cells 1 and 3 (right) before the time cut (top) and after the time cut (bottom).

Runs	p=-3GeV/c			p=+3GeV/c		
Events	N	%	%'	N	%	%'
Total	204,880	100	-	240,000	100	-
7 Cells Hit	60,557	29.6	100	62,305	26.0	100
3 Cells Not Hit	51,100	24.9	84.4	54,766	22.8	87.9
ATC Cut	46,026	22.5	76.0	38,569	16.1	61.9
ADC Cut	48,399	23.6	79.9	46,739	19.5	75.0
TDC Cut	14,792	7.2	24.4	15,646	6.5	25.1
All Cuts	9,279	4.5	15.3	7,724	3.2	12.4

Table 4.8: Cuts and their efficiencies for both sets of runs.

of a rather high noise level in all the readouts (TDC and ADC) but does not seriously limit our study as the amount of data available is very large.

4.4.4 Final Tracking Results

For a detailed discussion of individual track fits to both positive and negative signed momentum tracks see Appendix B.

It will be shown that the parametrizations of the TD function obtained by minimizing a χ^2 fit to either sets of runs are consistent with each other and, moreover, are in good agreement with the GARFIELD predictions. Fig. 4.21 (top) shows that the two fitted TD functions (one obtained from each of the run sets) are virtually indistinguishable which proves that the method of TD function estimation is valid and that the data is consistent. The difference between Garfield estimate and the fitted TD, Fig. 4.21 (bottom), is never larger than $30\mu m$ which is considerably smaller than the space residuals and is, therefore, satisfactory.

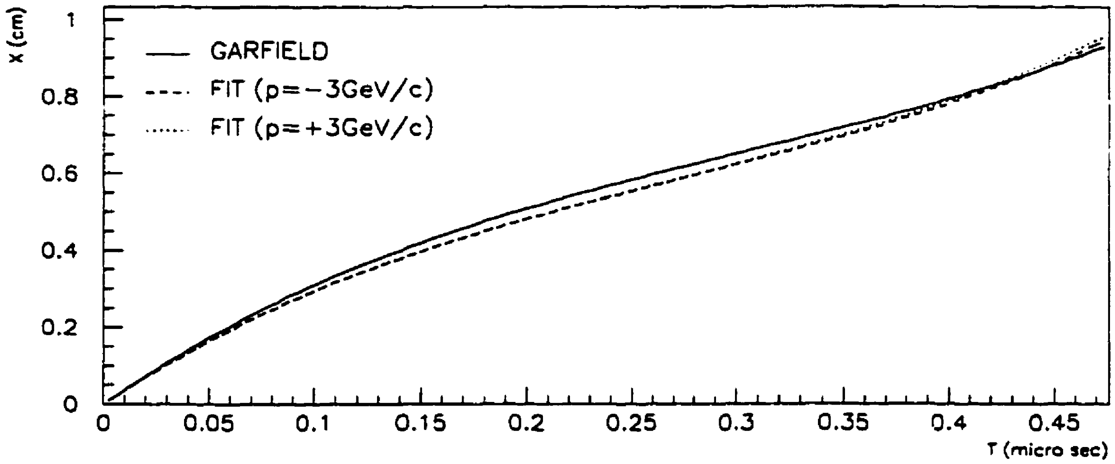

TD Functions

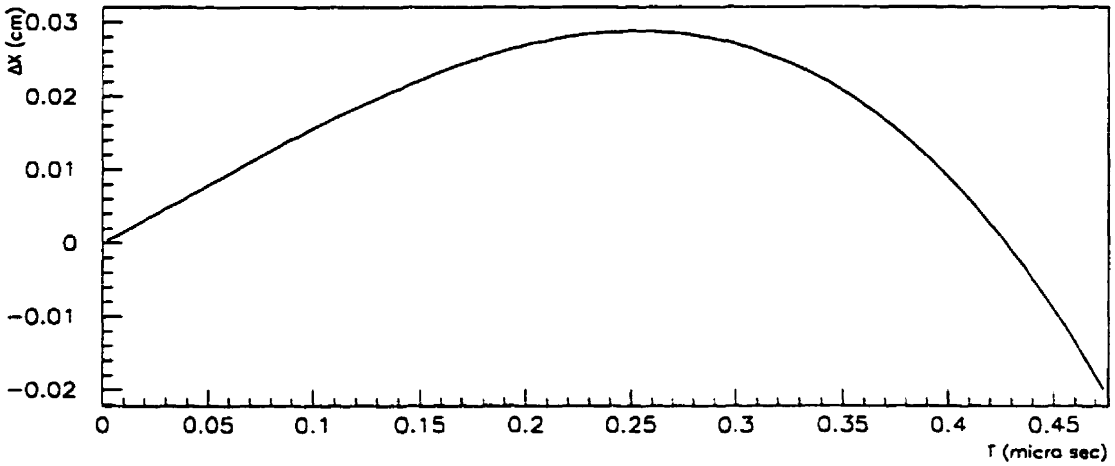

TD(GARFIELD) - TD(FIT)

Figure 4.21: Three different time-to-distance functions: a GARFIELD prediction and fits to each of the run sets (top). A difference between GARFIELD and the average of the fitted TD functions (bottom).

A summary of the TD function parameters for three different cases is given in Table 4.9. Also quoted are the average values (a weighted average, taking into consideration that cells 1, 3, 5, 7 are hit twice as much as the rest, was performed) of the absolute values of the means of the residual distributions, and the widths of the residual distributions. It can be concluded that the space residuals are well centered (as $|\mu| \ll \sigma$) meaning that the fitted drift function is unbiased. Average width of the space residual distributions is a measure of the tracking resolution achieved and, in our case, it equals $\approx 350\mu$m.

	$p = -3GeVc^{-1}$	$p = +3GeVc^{-1}$	Average	GARFIELD
P1	3.6866	3.6841	3.6854	3.840
P2	-8.4922	-8.4679	-8.480	-8.349
P3	10.386	10.453	10.420	9.266
$\|\mu_{RES}\|$ (μm)	12	25	19	-
σ_{RES} (μm)	330	372	351	-

Table 4.9: Time-to-distance function parameters, and parameters of Gaussian fits to residual distributions.

4.5 dE/dx Calculation and Results

Once good tracking resolution is achieved extracting the dE/dx information becomes simple. The amount of energy deposited in each cell is proportional to the charge accumulated in the corresponding ADC, after the pedestal was subtracted. The length a particle traversed in each cell is easily calculated for each track. Therefore, dE/dx is calculated as the ratio of the pedestal subtracted ADC readout to the cell-crossing length.

To make the truncation technique possible all the peaks of the ADC distributions must coincide. This adjustment is made by fitting the pedestal subtracted ACD spectra to Landau distributions and correcting for different peak positions. Since the units of energy depositions measured are arbitrary (no calibration was done to relate the ADC readout with the proper energy units) all the peaks will be rescaled to 100.

Run #	101	102	119	120	121
Date	Aug 22	Aug 22	Aug 23	Aug 23	Aug 23
Time	16:10	16:50	16:00	16:30	17:48
# of Events	20k	40k	20k	60k	60k
p(GeVc^{-1})	+3	+3	-3	-3	-3
Run #	122	124	143	144	146
Date	Aug 23	Aug 23	Aug 24	Aug 24	Aug 24
Time	19:00	20:33	12:20	13:00	14:35
# of Events	44.88k	20k	60k	60k	60k
p(GeVc^{-1})	-3	-3	+3	+3	+3

Table 4.10: Different runs used in dE/dx calculation.

Table 4.11 shows the calculated dE/dx resolution as a function of the percentage of hits used in the calculation. Statistical errors on the parameters of the Gaussian fits (done by PAW) are propagated to give the error in the measured resolution. The fits were performed in the $mean^{+2\times width}_{-3\times width}$ region to minimize the effect of the non-Gaussian tail at the high end, as suggested by [GDKK96].

$$\sigma\left(\frac{dE}{dx}\right) = \frac{width_{Gauss}}{mean_{Gauss}} \Rightarrow \sigma_{\sigma} = \sqrt{\frac{\sigma_w^2}{m^2} + \frac{w^2\sigma_m^2}{m^4}}, \tag{4.10}$$

with w_{Gauss} and m_{Gauss} being the width and the mean of the Gaussian fit. The

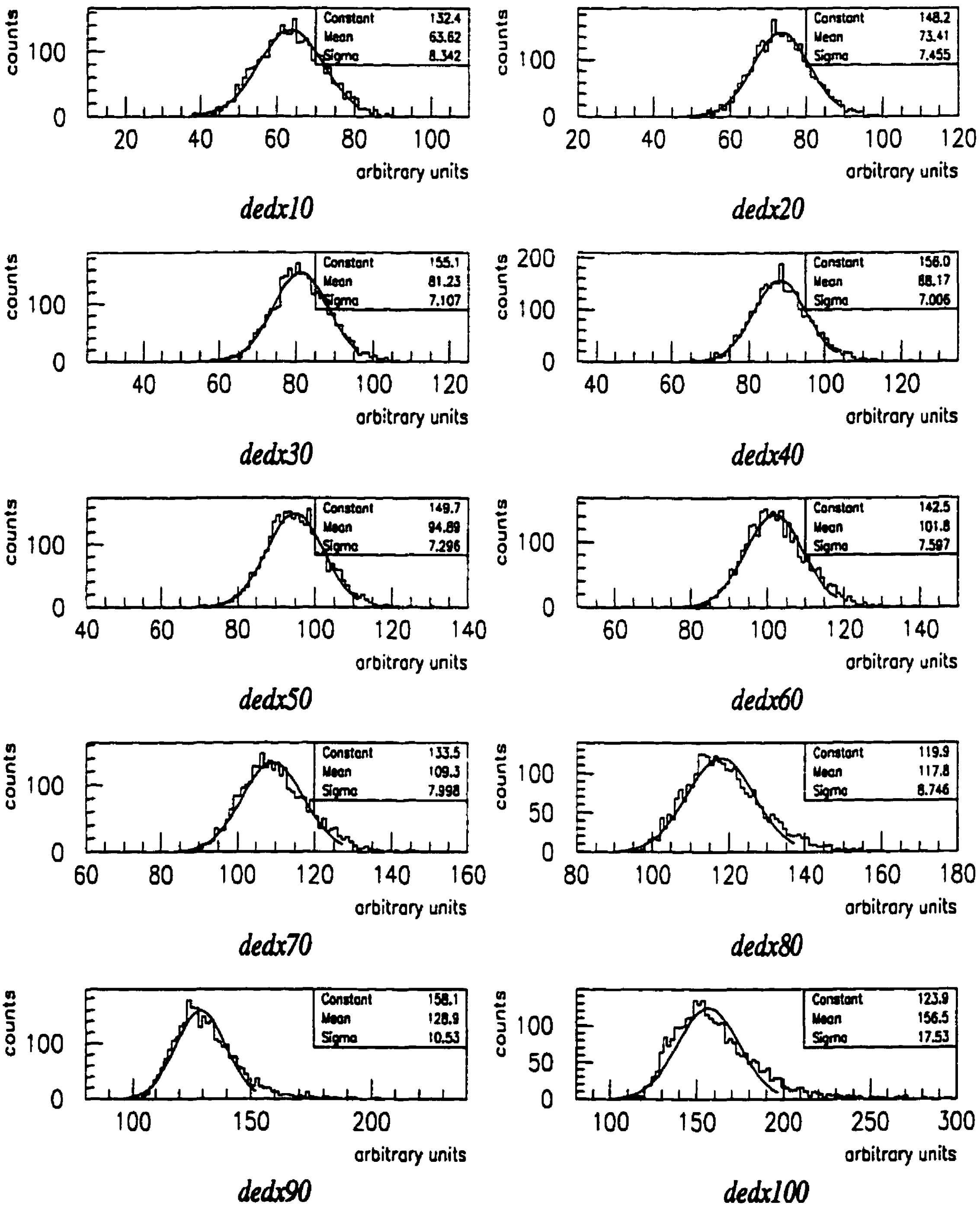

dedx10 dedx20

dedx30 dedx40

dedx50 dedx60

dedx70 dedx80

dedx90 dedx100

Figure 4.22: dE/dx resolutions obtained from both negative and positive signed momentum runs. Different fractions (10% to 100%) of hits were used in calculations.

Hits used	$\text{mean}_{\text{Gauss}}$	$\text{width}_{\text{Gauss}}$	$\sigma\left(\frac{dE}{dx}\right)$ [%]
10 %	63.63 ± 0.18	8.34 ± 0.14	13.1 ± 0.2
20 %	73.41 ± 0.16	7.46 ± 0.13	10.2 ± 0.2
30 %	81.23 ± 0.15	7.11 ± 0.12	8.7 ± 0.1
40 %	88.17 ± 0.15	7.01 ± 0.11	7.9 ± 0.1
50 %	94.89 ± 0.16	7.30 ± 0.12	7.7 ± 0.1
60 %	101.8 ± 0.2	7.60 ± 0.13	7.5 ± 0.1
70 %	109.3 ± 0.2	8.00 ± 0.13	7.3 ± 0.1
80 %	117.8 ± 0.2	8.75 ± 0.14	7.4 ± 0.1
90 %	128,9 ± 0.2	10.5 ± 0.2	8.2 ± 0.1
100 %	156.5 ± 0.5	17.5 ± 0.3	11.2 ± 0.2

Table 4.11: Gaussian fit parameters and the corresponding dE/dx resolutions for various fractions of hits used. Statistical errors are also shown.

resolution of dE/dx measurement varies with the truncation percentage and has a broad minimum at ≈ 70%, confirming a result stated by [GDKK96].

There is a systematic error associated with the truncation procedure, as the resolution depends on the percentage of hits used to calculate the means. To estimate this error the standard deviation of the resolutions (for truncation fractions of 30% to 90% [17]) was calculated yielding $\sigma_{systematic} = 0.5$ %. From Table 4.11 we can conclude that the optimum truncation percentage (giving the smallest dE/dx resolution while still having a symmetrical, Gaussian-like distribution) is 70%. The measured resolution is then:

$$\sigma\left(\frac{dE}{dx}\right) = (7.3 \pm 0.1 \pm 0.5)\ \% \qquad (4.11)$$

This result is in good agreement with $\sigma(dE/dx) = (6.8 \pm 0.3 \pm 0.5)\%$, given

---

[17] This range was centered around 60%, the truncation percentage most often used.

by [Bli97]. Our mean value of the resolution is slightly higher, due to different operating voltage; our statistical uncertainty is smaller because of the larger number of events used; the systematic uncertainty estimates are the same. Another measurement of the specific ionization resolution in the helium-isobutane (a different chamber geometry was used) was presented by [GDKK96]. Their result, $\sigma(dE/dx)$ ranging from $\approx$ 6.25% to $\approx$ 7.6%, depending on the operating voltage, is, again, consistent with our measurement. The resolution comes partly from the intrinsic width of the Landau distribution. This contribution for the Truncated Mean Method with 70% of hits used (incident particles are pions), as estimated by the GEANT simulation, is 3.7%. The experimental uncertainty contribution (resulting from both tracking and the ionization energy measurement errors) to the measured resolution is 3.6%.

The same truncation procedure was applied to the data from the test beam run at PSI in Zurich (incident particles are pions with momentum 0.405 GeV/c). The chamber was rotated by 90^0 (about the $y - axis$) with respect to the CERN setup. Again, 10 innermost cells are read but only the readout from 4 central cells was used in calculation (cells numbered 11, 9, 4 and 12 in Fig. 4.1). The advantage of this chamber positioning is simple. All of the pions passing through the central part of the cells (these are easily selected by imposing a cut on the drift time) traverse equal lengths in all four cells, thus completely eliminating tracking from the dE/dx calculation. The resolution expected should be better than previously quoted (4.11). Also, we can estimate the loss in the resolution caused by tracking uncertainties.

Gaussian fits to the truncated mean distributions for these runs are shown in Fig. 4.23 and the parameters, together with the calculated dE/dx resolutions, are listed in Table 4.12. Larger statistical errors are a consequence of a considerably smaller data set used. The optimum truncation percentage is again 70%, and

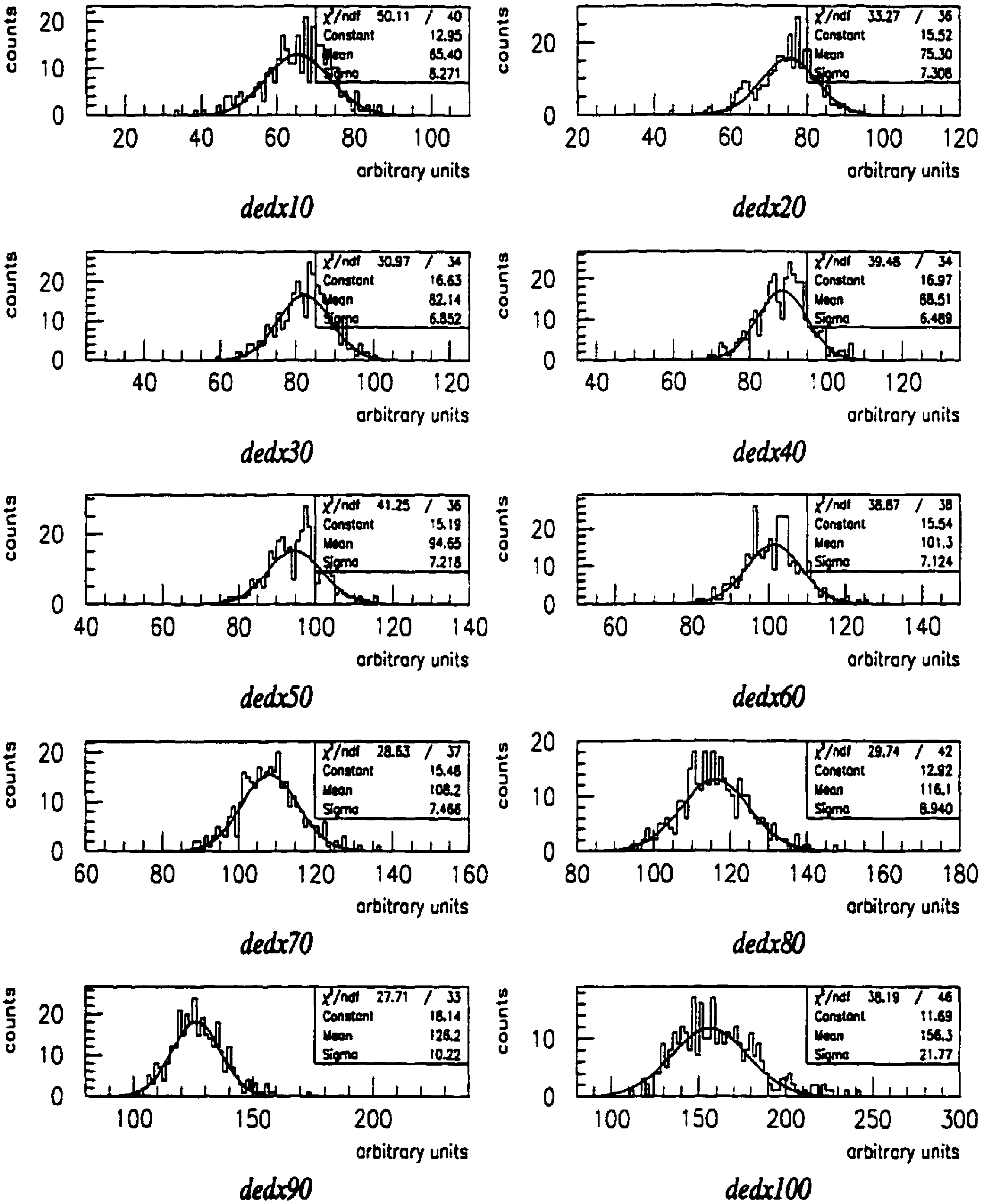

Figure 4.23: ***dE/dx*** **resolutions obtained from the PSI runs. Different fractions (10% to 100%) of hits were used in calculations.**

Hits used	mean_{Gauss}	width_{Gauss}	$\sigma\left(\frac{dE}{dx}\right)$ [%]
10 %	65.40 ± 0.60	8.27 ± 0.58	12.6 ± 0.9
20 %	75.30 ± 0.50	7.31 ± 0.48	9.7 ± 0.6
30 %	82.14 ± 0.44	6.85 ± 0.42	8.3 ± 0.5
40 %	88.51 ± 0.41	6.50 ± 0.39	7.3 ± 0.4
50 %	94.65 ± 0.45	7.22 ± 0.41	7.6 ± 0.4
60 %	101.3 ± 0.4	7.12 ± 0.39	7.0 ± 0.4
70 %	108.2 ± 0.5	7.47 ± 0.47	6.9 ± 0.4
80 %	116.1 ± 0.6	8.94 ± 0.56	7.7 ± 0.5
90 %	126.2 ± 0.6	10.2 ± 0.59	8.1 ± 0.5
100 %	156.3 ± 1.4	21.8 ± 1.4	13.9 ± 0.9

Table 4.12: Gaussian fit parameters and the corresponding dE/dx resolutions for various fractions of hits used. Statistical errors are also shown.

the systematic error is estimated as $\sigma_{systematic} = 0.5$ %. The measured dE/dx resolution for the PSI runs is then:

$$\sigma\left(\frac{dE}{dx}\right) = (6.9 \pm 0.4 \pm 0.5)\ \% \tag{4.12}$$

which is consistent with the result obtained from the CERN data. As tracking was not used in this calculation we can estimate the energy mismeasurement contribution to the resolution to be 3.2%. The contribution due to tracking is 1.6% (as the two errors, added in quadrature, must give 3.6%).

Both of the above results can be checked against the approximate formula for the dE/dx resolution [AC80]:

$$\sigma\left(\frac{dE}{dx}\right) = \frac{1}{2.35} 81 n^{-0.46} \left(\frac{\xi}{I}\right)^{-0.32}, \tag{4.13}$$

with n being the number of ionization measurements (in our case 40), ξ the same as defined in Eq. 2.27 and I the ionization potential. The factor of 1/2.35 comes from converting FWHM into σ. This empirical formula is well supported by experimental data for argon, xenon and propane. It should be good to about 20% in the range $0.5 < \xi/I < 10$. Using the relevant quantities calculated before ($I = 38.51$ eV and $\xi_{pion} = 64.71$ eV) yields the resolution of: $\sigma\left(\frac{dE}{dx}\right) = (5.3 \pm 1.1)\%$. The error is estimated based on 20% uncertainty of this empirical formula. This result is consistent with our measurements of the dE/dx resolution.

Chapter 5

Conclusion

Measurements of the dE/dx resolution in the Helium-Isobutane gas (80%He, 20%C_4H_{10}) which will be used in the BaBar drift chamber were made using a small scale prototype drift chamber. Test-beam experiments were performed at CERN (PS, proton and pion beam with a variable momentum of 1 GeV/c to 5 GeV/c) and at Zurich (PSI, pion beam with a 0.405 GeV/c momentum).

Testing of the Truncated Mean Method verified that the Landau spectrum of the specific ionization can be converted into a Gaussian-like. The quality of the Gaussian fit, however, depends on the fraction of hits used in the calculation and on the amount of statistics used.

A GEANT simulation was made in order to study the chamber response in absence of the experimental uncertainties. The dE/dx resolution calculated after applying the truncation method (70% of hits are used) to the pion specific ionization spectrum is 3.7% and it is a measure of the intrinsic width of the Landau distribution.

A GARFIELD simulation of the drift chamber was done to obtain the first order time-to-distance function and find its suitable parametrization for the subsequent fitting to the data (a third order polynomial with a zero constant term proved to be the best choice).

All of the selected events were required to have exactly 7 good hits with the arrival time larger than time zero (time zeros were fitted to the time spectra in each cell and adjusted to center the space residuals). Additional cuts were made on ADC, TDC and ATC responses to eliminate events consistent with the pedestal.

After the track fit was performed by a χ^2 minimization the average spatial resolution, as measured by the weighted averages of the space residuals in all cells, was calculated to be:

$$|\mu_{RES}| \pm \sigma_{RES} = (19 \pm 351)\mu\text{m}.$$

Obtained time-to-distance function is in good agreement with the GARFIELD prediction.

The dE/dx resolution, defined as the ratio of the width of the Gaussian distribution to the pedestal subtracted mean, was calculated for both sets of runs. Various fractions of hits used were tested and the optimum was found to be 70%. Systematic uncertainty was estimated by varying the truncation fraction. The results are:

$$\sigma\left(\frac{dE}{dx}\right) = (7.3 \pm 0.1 \pm 0.5)\ \%,$$

for the PS runs, and:

$$\sigma\left(\frac{dE}{dx}\right) = (6.9 \pm 0.4 \pm 0.5)\ \%,$$

for the PSI runs. The increase in the resolution with respect to the GEANT prediction can be explained in terms of the contribution due to the errors in the ionization energy measurement (3.2%) and the contribution due to imperfect tracking (1.6%).

Appendix A

The Pedestal Run

A pedestal run with 4000 events was taken in order to study the system dependent backgrounds. The trigger signal was periodically created and the chamber readouts were taken while the beam was turned off.

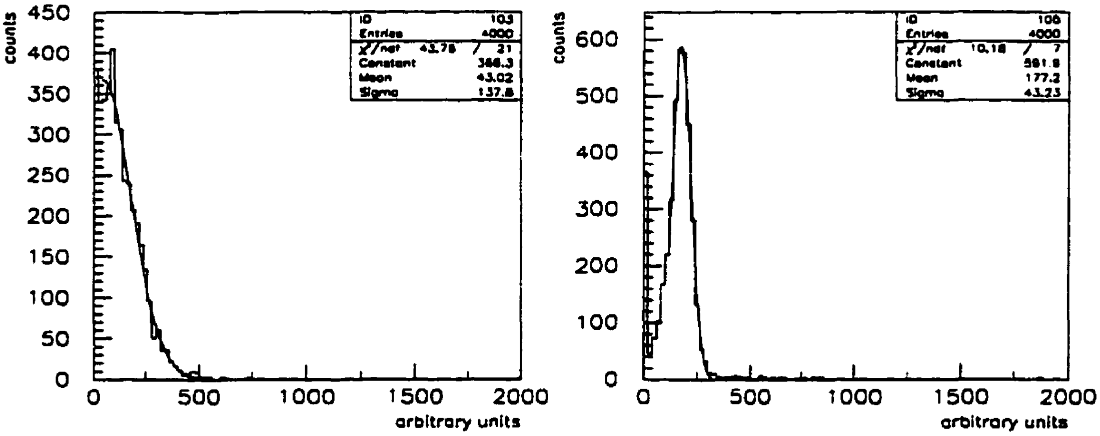

ATC3 *ATC5*

Figure A.1: ATC readouts from both counters. Gaussian fits to pedestal distribution are also shown.

The readouts from both threshold counters are shown in Fig. A.1. Gaussian fits to the distributions yield the following pedestal values (arbitrary units for the ligh yield are used): $ATC3 = 43 \pm 137$ and $ATC5 = 177 \pm 43$.

By looking at the TDC readouts (Fig. A.2) it can be realized that the noise level is reasonably small. The number of overflows in each of the TDCs is close to 4000 (which is the total number of events). Only cell 3 has a considerably higher noise level. Table A.1 lists the number of events in which a given TDC channel did not overflow, which is a measure of the noise level.

Cell #	1	2	3	4	5	6	7	8	9	10
N_{EVENTS}	35	25	311	26	21	25	25	35	25	26
%	0.88	0.63	7.78	0.65	0.53	0.63	0.63	0.88	0.63	0.65

Table A.1: Noise level in each of the TDC channels.

The pedestal values of the ADC readouts were obtained by a Gaussian fit. Even though the measured distributions are not Gaussian (as can be seen in Fig. A.3), these fits give us the information about the peak (corresponding to the mean of the fitted Gaussian) and the width of the pedestal ADC distributions. This information is summarized in Table A.2.

Cell #	1	2	3	4	5	6	7	8	9	10
μ	88.8	100.9	65.5	213.6	121.5	147.1	82.3	116.4	86.4	230.4
σ	3.4	9.0	6.2	8.9	8.7	16.9	5.4	4.1	7.1	10.2

Table A.2: Means and widths of Gaussian fits to pedestal ADC distributions. Arbitrary units are used.

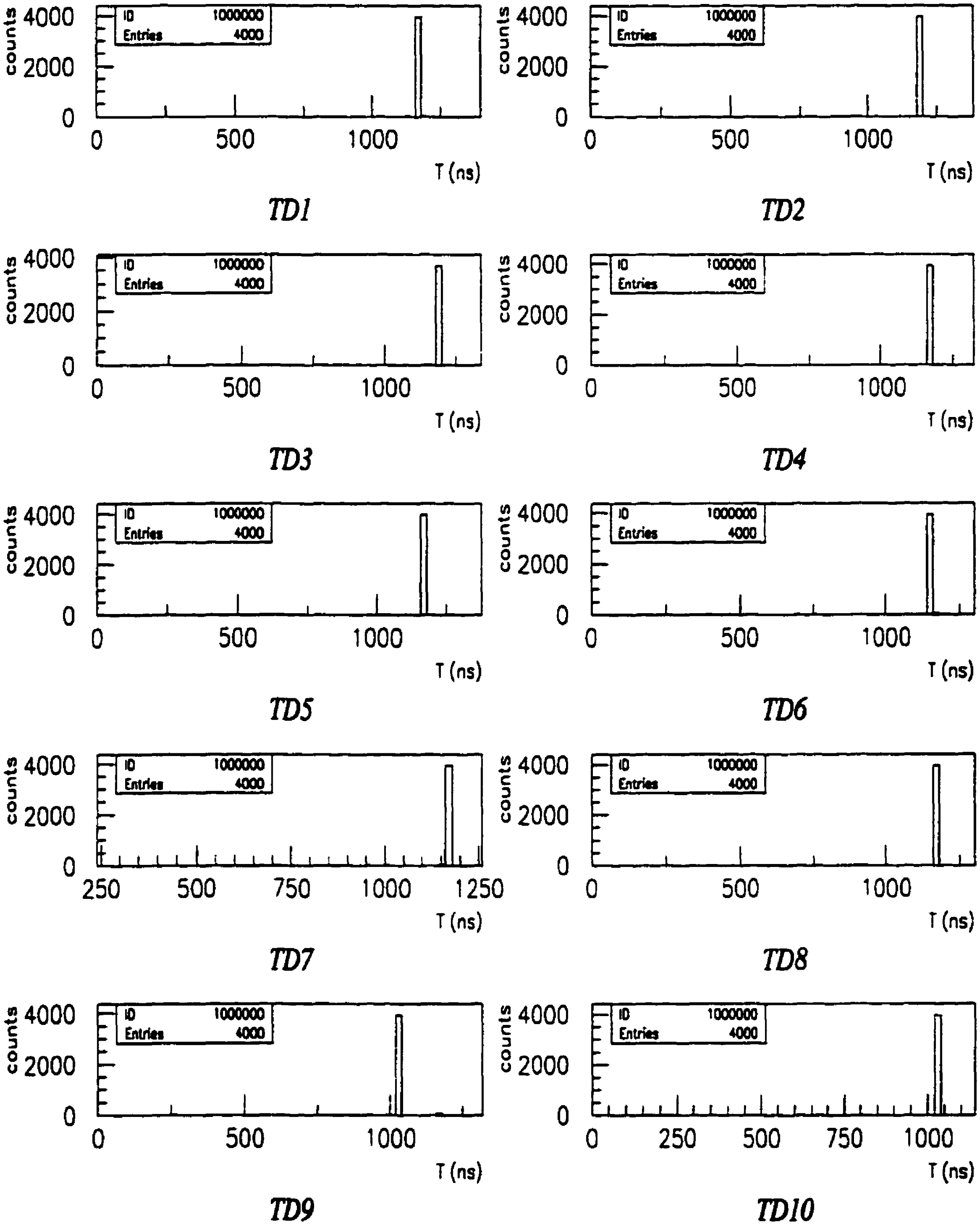

TD1 TD2

TD3 TD4

TD5 TD6

TD7 TD8

TD9 TD10

Figure A.2: TDC readouts for all 10 cells. The noise level is small as the TDCs overflow for almost all events.

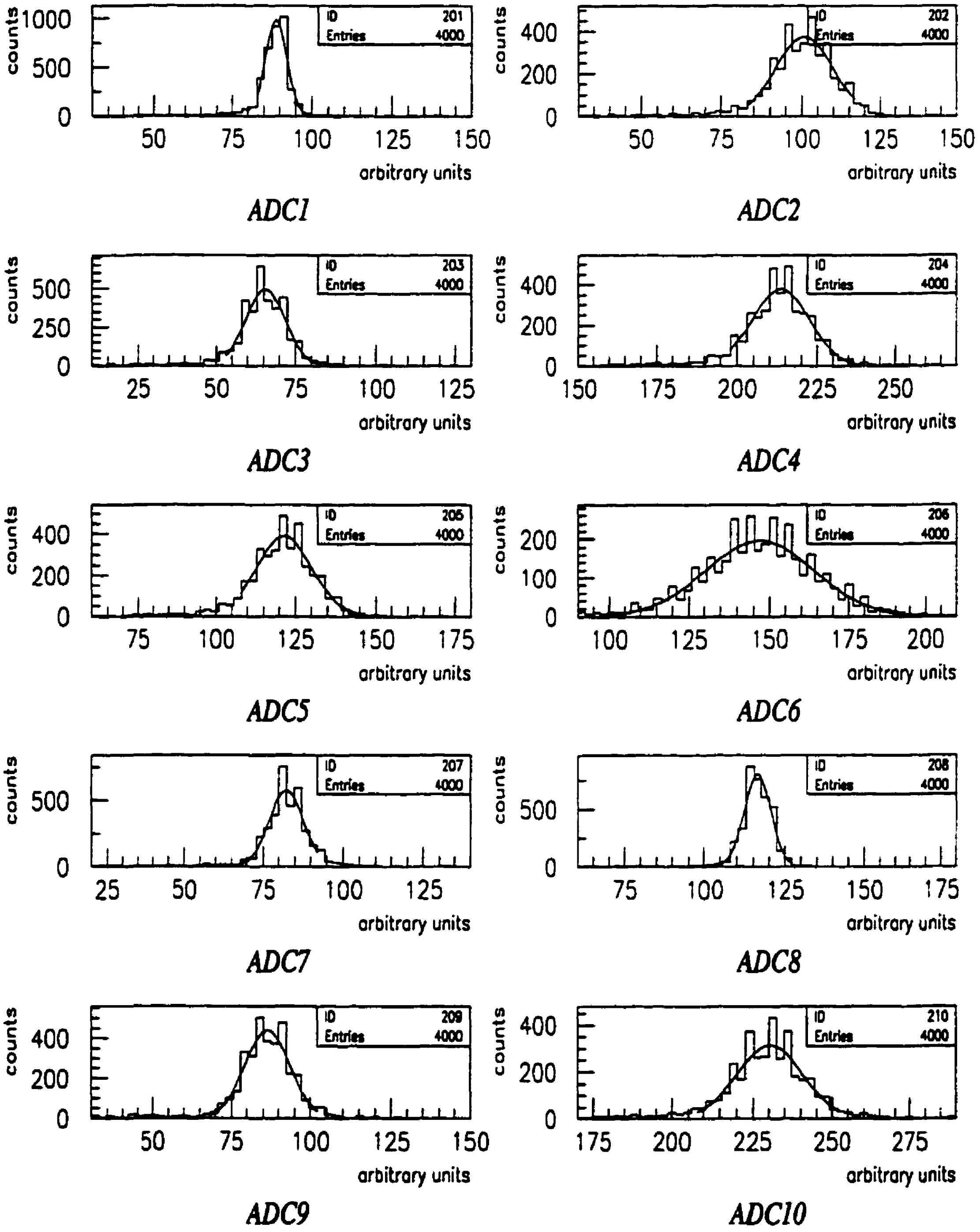

ADC1 ADC2

ADC3 ADC4

ADC5 ADC6

ADC7 ADC8

ADC9 ADC10

Figure A.3: ADC readouts for all 10 cells. Gaussian fits to pedestal distribution are also shown.

Appendix B

Track Fits Using MINUIT

The track fits (with fit parameters being the coefficients of the parametrized time-to-distance function) were done using MINUIT in data-driven mode [Jam94]. Initial values of the parameters P1, P2 and P3 are GARFIELD predictions.

B.1 Negative Signed Momentum Runs

Once the track fit converges (remember that a sum over all cells hit in all events of the squares of the spatial residuals is being minimized) the optimum parameters of the time-to-distance function are set. The quality of the fit can be verified by plotting various quantities. Fig. B.1 shows distances to the wire in cell 1 as calculated from the drift time (which is the TDC readout after T0 subtraction) using the time-to-distance function (top left, $X1$) and the distance of the track (obtained from the fit) to the wire (top right, $XFT1$). If the knowledge of the TD function and the time measurements were perfect the two distances should be the same. Due to experimental errors there is a difference between the two values, called a space residual: $R_S = X - XFT$. These will be discussed in a moment. A scatter plot of the track distance versus the calculated distance is also shown (bottom left). We can see that there is a strong correlation between the two for all but very small and very large distances. This is a consequence of a small number of events falling in these regions, which compromises the quality of the fit there. The best fit is obtained around the middle of the cell where the statistics is the highest. A plot of the track distance versus the drift-time

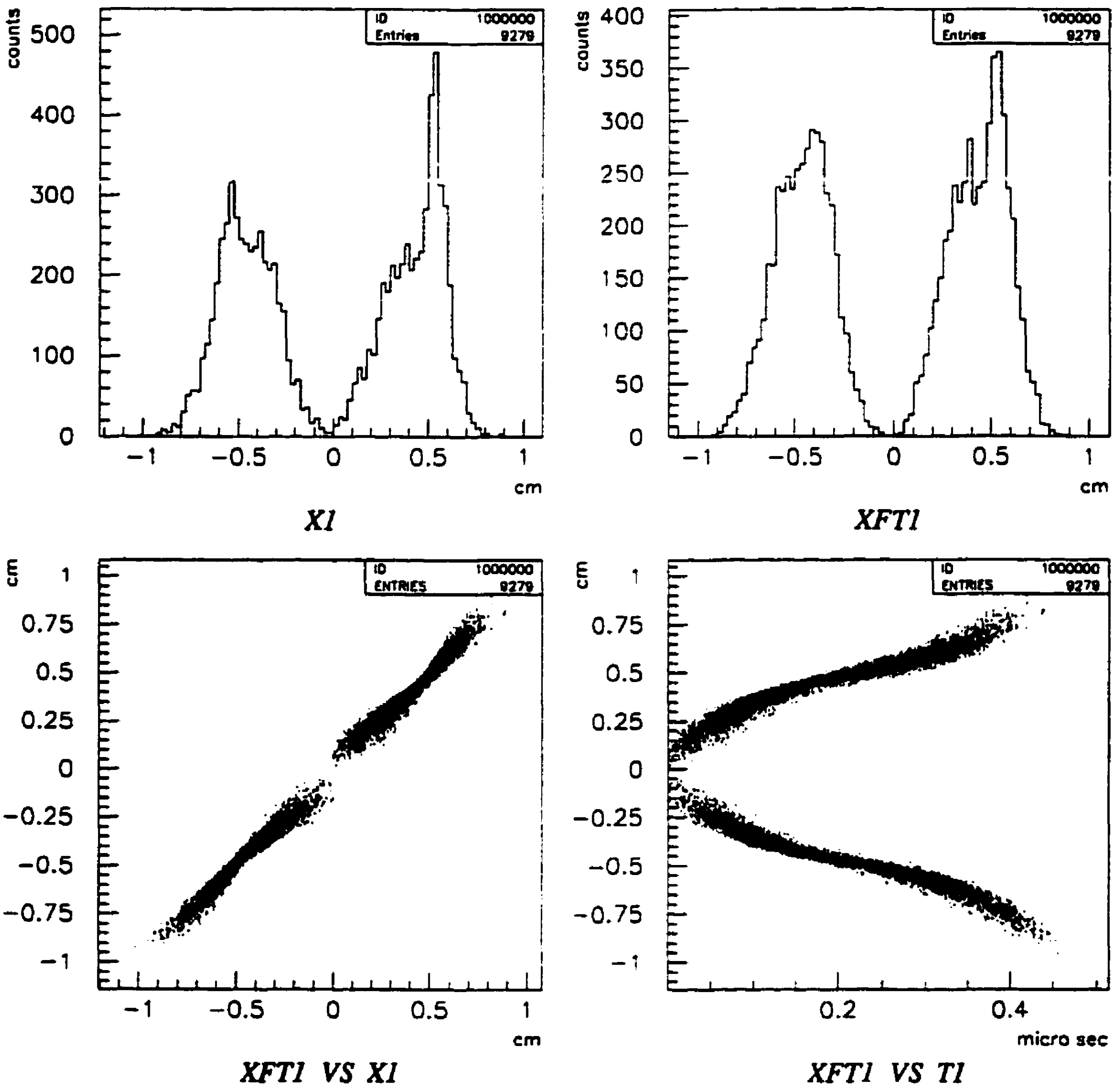

Figure B.1: Calculated and fitted distances to the wire in cell 1. Negative signed momentum runs were used.

(bottom right) closely resembles the TD function, as expected. Low statistic at very short drift distances prevents us from verifying that fitted distances also approach zero for very short drift times. Spatial residuals measure the quality of track reconstruction in a given chamber, as they correspond to the uncertainty in the particle trajectory. Fig. B.2 shows spatial residuals in all 10 cells of our prototype chamber and Table B.1 summarizes the parameters of the Gaussian fits to residual distributions. All the residual distributions are centered around zero (to within 30μm, which is large compared to the widths) which means that the track fit is not biased toward distances either larger or smaller than those calculated by the TD function. The centering of the residual distributions was done by adjusting the time-zeros, as mentioned before. Finally, the values of the fit parameters (P1=3.6866, P2=-8.4922, P3=10.386) do not differ significantly from the GARFIELD predictions.

Cell #	1	2	3	4	5	6	7	8	9	10
μ	-11.0	-10.1	6.7	-20.9	-1.0	-29.3	12.8	24.2	4.0	16.6
σ	295	346	336	358	375	316	288	330	357	326

Table B.1: Means and widths of Gaussian fits to space residuals (μm), $p = +3\text{GeVc}^{-1}$.

To show the efficiency of the drift time cut, as discussed in the Cuts and Event Selection subsection, the track fitting will be attempted on the data set (negative signed momentum) without the cut performed. To simulate the same amount of statistics only 10,000 events entered the fit. As shown in Fig. B.3, space residuals increase drastically is the time cut is not applied. In addition, they are neither symmetrical nor centered at zero. The asymmetry of the residuals is a consequence of the wrong TD function (P1=6.2207, P2=-25.137, P3=33.857) resulting from

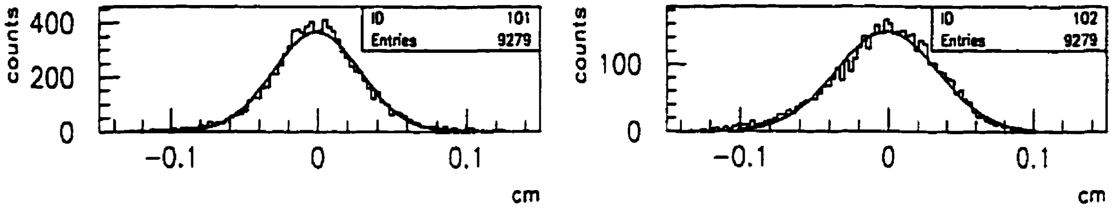

Residuals 1 *Residuals 2*

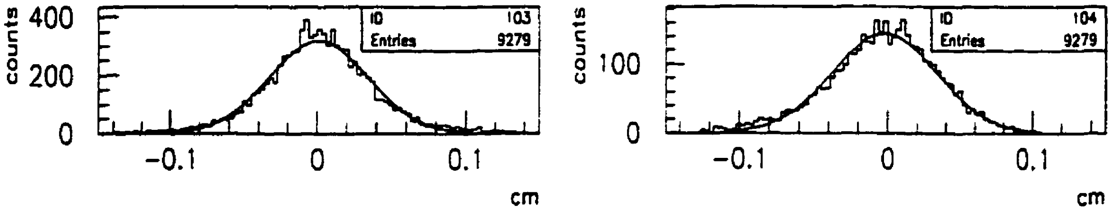

Residuals 3 *Residuals 4*

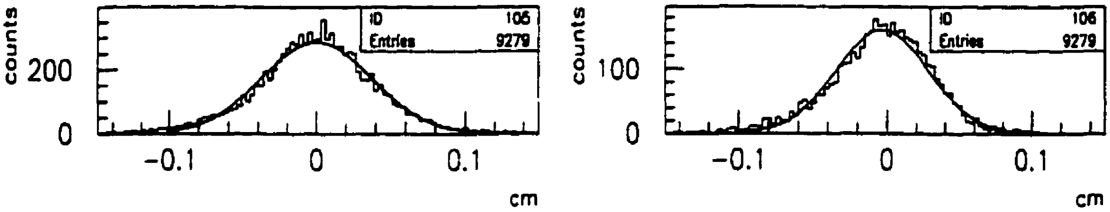

Residuals 5 *Residuals 6*

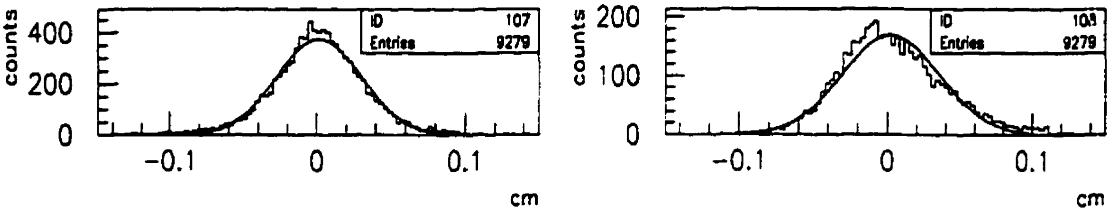

Residuals 7 *Residuals 8*

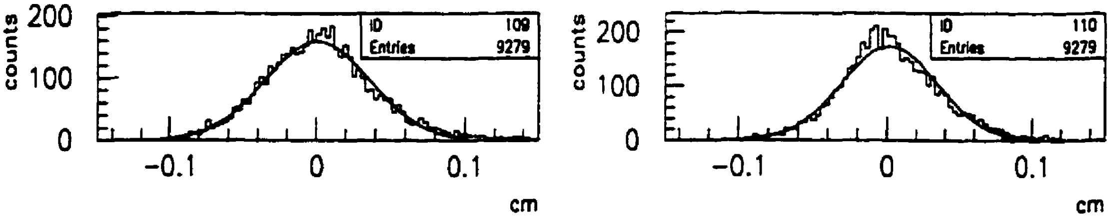

Residuals 9 *Residuals 10*

Figure B.2: Spatial residuals in all cells with a drift-time cut applied. Negative signed momentum runs were used.

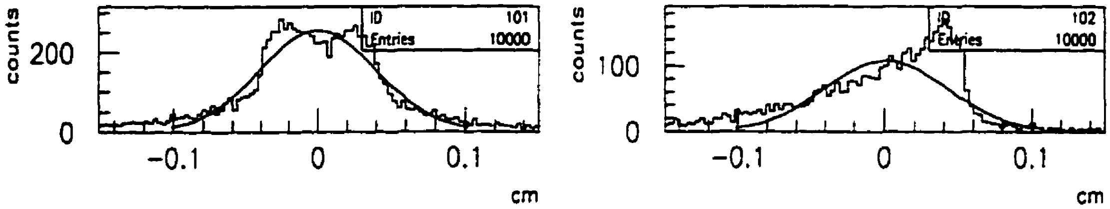

Residuals 1 *Residuals 2*

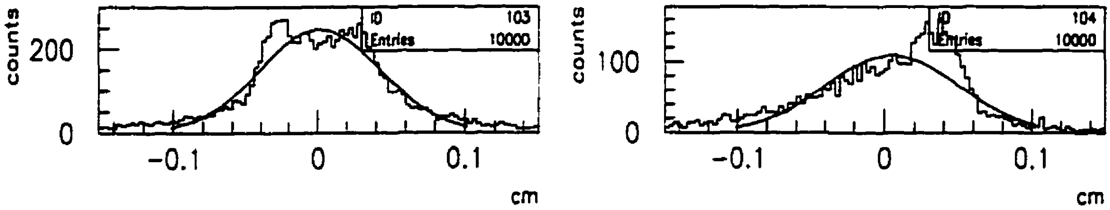

Residuals 3 *Residuals 4*

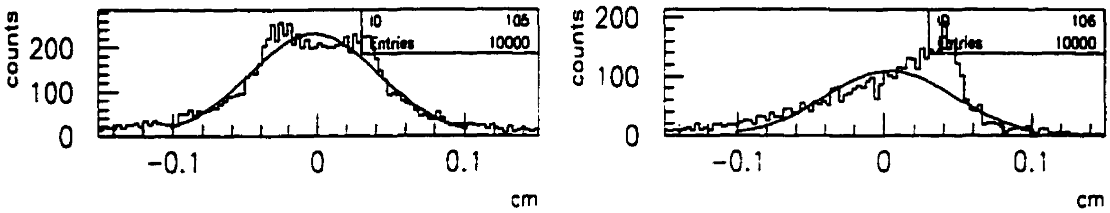

Residuals 5 *Residuals 6*

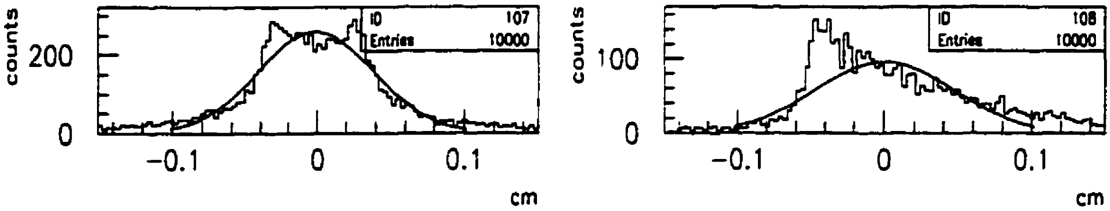

Residuals 7 *Residuals 8*

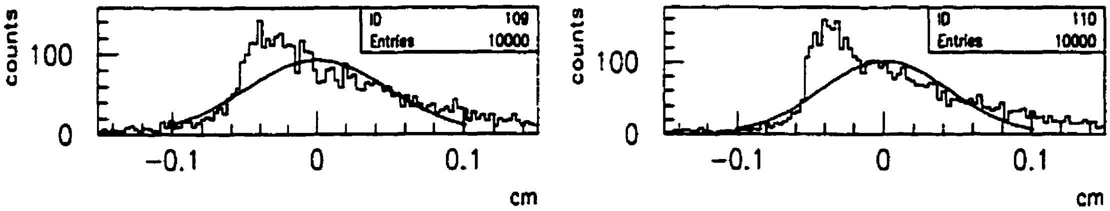

Residuals 9 *Residuals 10*

Figure B.3: Spatial residuals in all cells without a drift-time cut applied. 10,000 events from negative signed momentum runs were used.

trying to fit uncut data. Different TD functions are shown in Fig. B.4. The shifts

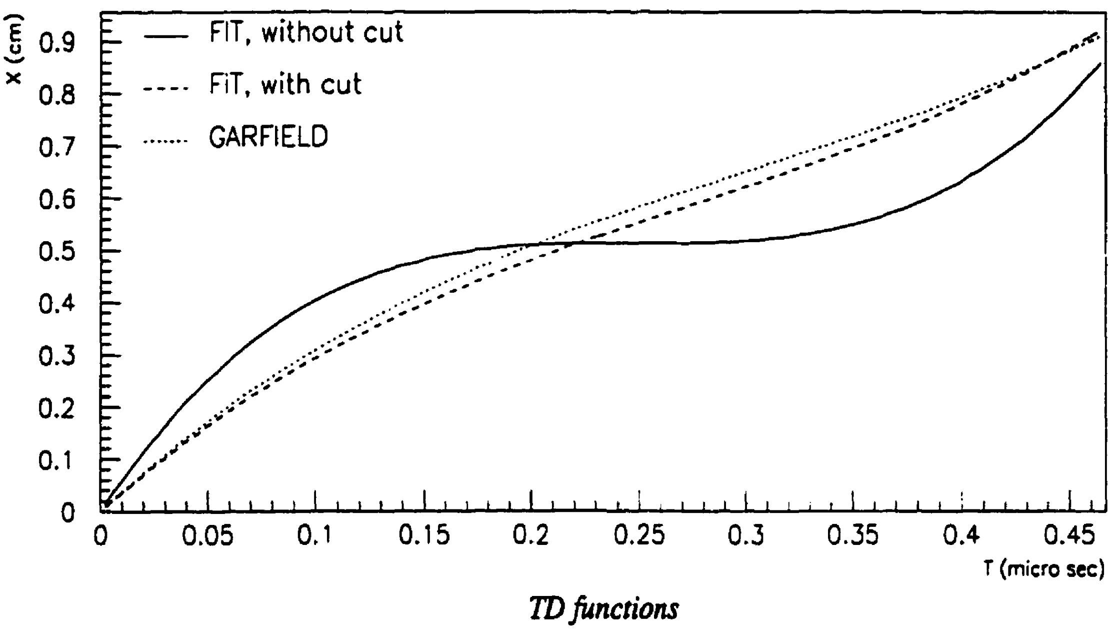

Figure B.4: Time-to-distance functions obtained from fits to dat with and without the drift time cut, and from GARFIELD prediction.

in the mean values of the residuals are produced by the overestimate of the TD function for small times whereas the elongated tails at the opposite ends of the distributions are caused by the underestimate of the TD function for large times. Remember that all positions (X and XFT) are given with respect to the chamber z axis (see Fig. 4.1) and are, therefore, positive in cells 8, 9, 10 and negative in cells 2, 4, 6. An overestimate of the TD function makes $|XFT| > |X|$ in all cells resulting in negative mean space residuals in cells 8, 9, 10 and in positive mean space residuals in cells 2, 4, 6. Note that mean space residuals in cells 1, 3, 5, 7 are either positive or negative, resulting in a double peeks seen in Fig. B.3.

B.2 Positive Signed Momentum Runs

Fig. B.5 shows the space residuals after the fit to positive signed momentum runs, with a drift time cut applied and Table B.2 summarizes the parameters of the Gaussian fits to residual distributions. We can see that both the residual distributions and the parameters of the TD function (P1=3.6841, P2=-8.4679, P3=10.453) agree with the values obtained from the first set of runs. The residuals are not as well centered around zero because the correction to time zeros was done using only the $p = -3\text{GeVc}^{-1}$ runs, as mentioned before.

Cell #	1	2	3	4	5	6	7	8	9	10
μ	-29.4	-30.0	14.1	-27.3	-4.1	-50.0	14.5	82	19.3	16.2
σ	325	389	396	398	426	358	324	366	388	361

Table B.2: Means and widths of Gaussian fits to space residuals (μm), $p = +3\text{GeVc}^{-1}$.

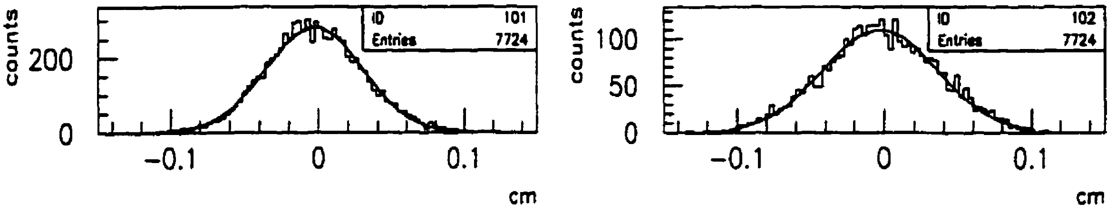

Residuals 1

Residuals 2

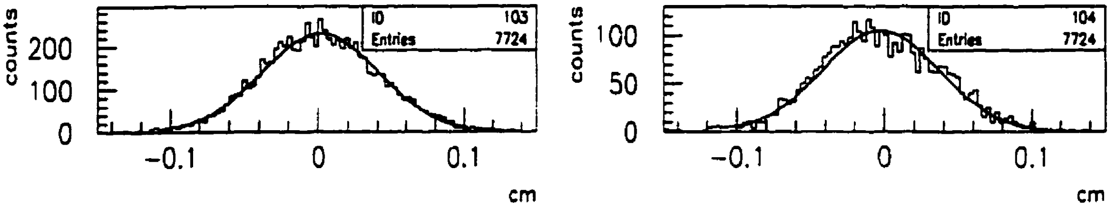

Residuals 3

Residuals 4

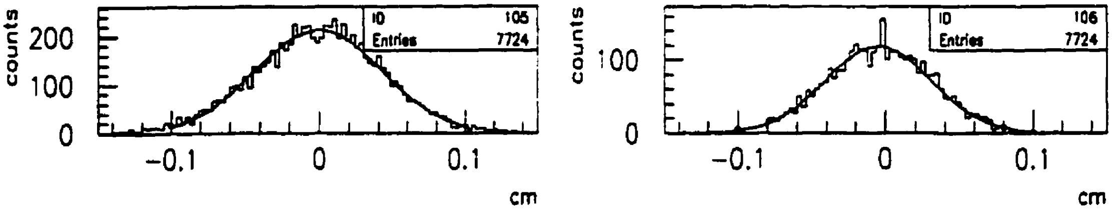

Residuals 5

Residuals 6

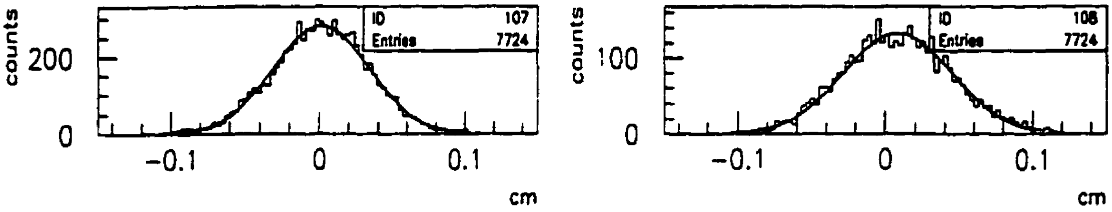

Residuals 7

Residuals 8

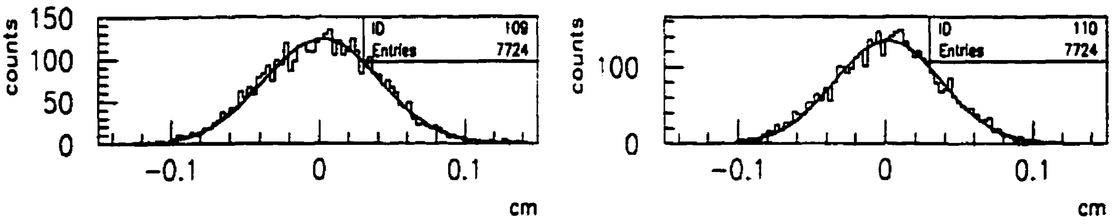

Residuals 9

Residuals 10

Figure B.5: Spatial residuals in all cells with a drift-time cut applied. Positive signed momentum runs were used.

Bibliography

[AC80] W. W. M. Allison and J. H. Cobb. Relativistic charged particle identification by energy loss. *Ann. Rev. Nucl. Part. Sci.*, 30:253, 1980.

[B⁺84] R. K. Bock et al. *Formulae and Methods in Experimental Data Evaluation, General Glossary*, 1:110, 1984.

[BBB92] A. Boyarski, D. Briggs, and P. Burchat. *NIM A*, 323:267, 1992.

[BC84] S. Baker and R. Cousins. *NIM*, 221:437, 1984.

[Bet30] H. A. Bethe. *Ann. d. Phys.*, 5:325, 1930.

[Bet32] H. A. Bethe. *Z. Phys.*, 76:293, 1932.

[Bia89] S. F. Biagi. *NIM A*, 283:716, 1989.

[Bli97] V. Blinov. Babar drift chamber de/dx resolution study based on proto-ii data. BaBar note No. 397, 1997.

[Blo33] F. Bloch. *Z. Phys.*, 81:363, 1933.

[BSS79] M. Bander, D. Silverman, and A. Soni. *Phys. Rev. Lett.*, 43:242, 1979.

[Bur97] C. P. Burgess. A primer on the standard model of elementary particle physics. Course Notes, McGill University, 1997.

[C⁺91] V. Cindro et al. *NIM A*, 309:411, 1991.

[Cab63] N. Cabibbo. *Phys. Rev. Lett*, 10:531, 1963.

[CCFT64] J. Christenson, J. Cronin, V. Fitch, and R. Turlay. *Phys. Rev. Lett.*, 13:138, 1964.

[CK84] L. L. Chau and W. Y. Keung. *Phys. Rev. Lett*, 53:1802, 1984.

[Col95] BaBar Collaboration. *BaBar Technical Design Report.* Stanford Linear Accelerator Center, Stanford, California, March 1995.

[Fer86] R. C. Fernow. *Introduction to Experimental Particle Physics.* Cambridge University Press, 1986.

[GDKK96] K. K. Gan, C. M. Daubenmier, H. Kagan, and R. Kass. Study of helium-based drift chamber gasses. *NIM A*, 374:27–33, 1996.

[GG74] H. Georgi and S. L. Glashow. *Phy. Rev. L.*, 32:438, 1974.

[GKR97] F. J. Gilman, K. Kleinknecht, and B. Renk. The cabibbo-kobayashi-maskawa mixing matrix. Revision of Physical Review **D54**, 1(1996); available at http://pdg.lbl.gov/, 1997.

[Gri87] D. Griffiths. *Introduction to Elementary Particles.* John Wiley & Sons, Inc., 1987.

[Gro96] M. Gronau. CP violation in B-decays: The standard model and beyond. *NIM A*, 384:1–7, 1996.

[Gru96] C. Grupen. *Particle Detectors.* Cambridge University Press, 1996.

[Jam94] F. James. *MINUIT Function Minimization and Error Analysis.* CERN, Geneve, Switzerland, 1994.

[Kay96] B. Kayser. CP violation in the K and B systems. Proceedings of the Summer School in High Energy Physics and Cosmology, International

Center for Theoretical Physics, Trieste, June-July 1995, November 1996.

[KM73] M. Kobayashi and T. Maskawa. *Prog. Theor. Phys*, 49:652, 1973.

[KS84] K. S. Kolbig and B. Schorr. *Comp. Phys. Comm*, 32:121, 1984.

[Leo87] W. R. Leo. *Techniques for Nuclear and Particle Physics Experiments.* Springer-Verlag, 1987.

[Lon96] D. London. CP violation and heavy hadrons. Presented at 2nd International Conference on Hyperons, Charm and Beauty Baryons, Montreal, Canada, 27-30 Aug 1996., November 1996.

[Lue57] G. Lueders. *Annals Phys.*, 2:1–15, 1957.

[MRRS88] G. Musiol, J. Ranft, R. Reif, and D. Seeliger. *Kern und Elementarteilchenphysik.* VCH Verlagsgesellschaft, Weinheim, 1988.

[NQ92] Y. Nir and H. R. Quinn. CP violation in B physics. *Annual Review of Nuclear and Particle Science*, 42:211, 1992.

[Odd87] P. Oddone. *in Proceedings of the UCLA Workshop: Linear Collider $B\bar{B}$ Factory Conceptual Design, ed. D. Stork (World Scientific)*, page 243, 1987.

[PBES92] S. M. Playfer, R. Bernet, R. Eichler, and B. Stampfli. Studies of helium gas mixtures for low mass tracking detectors. *NIM A*, 315:494–501, 1992.

[Ram82] N. F. Ramsey. *Rep. Prog. Phys.*, 45:95, 1982.

[Ros52] B. Rossi. *High Energy Particles.* Prentice-Hall, 1952.

[Sak67] A. D. Sakharov. *JETP Letters*, 5:24, 1967.

[Sof94] Application Software Group. *GEANT Detector Description and Simulation Tool.* CERN, Geneve, Switzerland, 1994.

[Sof95] Application Software Group. *PAW Physics Analysis Workstation.* CERN, Geneve, Switzerland, 1995.

[Tal79] R. Talman. *NIM*, 159:189, 1979.

[U+93] S. Uno et al. *NIM A*, 330:55, 1993.

[Vav57] P. V. Vavilov. *JETP*, 5:749, 1957.

[Vee96] R. Veenhof. *Garfield Simulation of Gaseous Detectors.* CERN, Geneve, Switzerland, http://consult.cern.ch/writeup/garfield, 1996.

[VRFC82] J. Va'vra, L. Roberts, D. Freytag, and P. Clancey. Energy loss measurement in a jet chamber. *NIM A*, 203:109, 1982.

[W+57] C. S. Wu et al. *Phys. Rev.*, 105:1413, 1957.

[WN96] E. J. Weinberg and D. L. Nordstrom, editors. *Review of Particle Properties*, volume 54 of *Physical Review D, Particles and Fields.* The American Physical Society, American Institute of Physics, 1996.

[Wol83] L. Wolfenstein. *Phys. Rev. Lett*, 51:1945, 1983.

[WPF88] F. W. Walker, J. R. Parrington, and F. Feiner. *Chart of the Nuclides.* Knolls Atomic Power Laboratory, 1988.